

Pattern Formation in 2D Continuum and Discrete Chemically Reactive Media

Hossein Azizi

Doctor of Philosophy

Department of Physics

McGill University

Montreal, Quebec

2017-10-16

A thesis submitted to McGill University in partial fulfillment of the requirements of the
degree of Doctor of Philosophy

© Hossein Azizi 2017

ACKNOWLEDGEMENTS

This work would not have been possible without help and advise of my supervisor Nikolas Provatas. I can not thank him enough for taking me graciously under his wings and taught me how not only to be a better physicist, but also a better person.

I wish to thank our collaborators in mechanical engineering department at McGill University Andrew Higgins and Samuel Goroshin for the fruitful discussions and assistance with the project. Special thanks to Sebastian Gurevich for his great collaboration and mentorship. I would also like to thank the members of our computational material science group, especially Nana Ofori-opoku, David Montiel, Michael Greenwood, Nan Wang, Gabriel Kocher, and Nathan Smith for their valuable consultations and advise. I thank my sister, Fereshteh, for always being there for me and help to get through difficult times.

This work was supported by a Canadian Space Agency Class Grant “Percolating Reactive Waves in Particulate Suspensions” under Grant No. 232916. I would like to acknowledge their financial support. The numerical studies of this work was performed using high computing resources provided by Compute Canada (www.computecanada.ca) and Calcul Quebec, specially the staff of HPC McGill (www.hpc.mcgill.ca) without their restless effort and technical support this numerical work was not plausible.

Last but no least, I like to thank my parents. I will always be grateful to you and your support and kindness.

CONTRIBUTIONS OF AUTHORS

The material contained in Chapter 2 (partially) and Chapter 3 has been published in a peer-reviewed journal article, and is available in:

- (1) H. Azizi, S. Gurevich, N. Provatas. Analysis of thermodiffusive cellular Instabilities in continuum combustion fronts. *Physical Review E*, 95(1):2219, 2017.
- (2) Our examination of combustion fronts in random discrete media is being prepared for an upcoming publication.

ABSTRACT

The spatio-temporal instabilities of a solid-gas combustion front and its resulting pattern formation are examined in the framework of thermal-mass diffusional instabilities, in the case of homogenous and heterogeneous media. In our numerical simulations, by employing a novel adaptive mesh refinement algorithm, we achieve experimentally relevant system sizes. To our knowledge, this is the first work where these methods are applied to a new class of solid-gas combustion models.

We introduce a unified mathematical model called “master model” to describe the combustion of metal fuel particles in an oxidizer gas, based on the physical parameters of the problem (i.e. order of the chemical reaction ($n = 0, 1$), the ignition temperature T_{ign} , and the Lewis number Le , defined as the ratio of thermal to mass diffusivity), and for different limits of oxidizer mass diffusivity, with continuous and random reactant fuel distributions.

Our numerical findings for a combustion front in the continuum limit show that a front develops a cellular structure for a specific ignition temperature T_{ign} , and below a critical Lewis number Le_c . The linear regime of these morphologies is investigated numerically and found to agree well with the dispersion relation predicted analytically by Brailovsky et al.. The effect of system size and Lewis number on the linear regime were also addressed. For Lewis numbers Le close to the critical value Le_c , the transition from linear to non-linear (i.e. late time) is prolonged. This regime is characterized by the appearance of shallow-cell structures, and those morphologies can be described qualitatively based on the growth modes available in the linear regime. For this reason, this regime is called

“quasi-linear” regime. By lowering the Lewis number values below $\text{Le} \sim 0.4$, the morphology of the front changes significantly and becomes complex, featuring non-symmetric deep cells and overhangs. We explored this highly non-linear regime and the influence of finite size effects on the late-time dynamics of tip splitting and merging, emphasizing parallels with isotropic dendritic microstructures in solidification phenomena. The dendritic patterns simulated in this work are similar to those observed in experiments of flame propagation over a bed of nano-aluminum powder burning with a counter-flowing oxidizer conducted by Malchi et al. We further studied the linear regime of cellular combustion fronts under heat dissipation conditions. Our numerical results show that the growth rate of high k modes, in the presence of heat dissipation, can effectively be described by the same modes as in the adiabatic condition, but with their amplification rate increased. This essentially resembles the effect of lowering the Lewis number on the linear regime of adiabatic combustion. For small k modes, however, a different behaviour is observed between our numerical and analytical results when heat dissipation is considered. It is plausible that this is an artifact of finite-size effects in our simulations, which suppresses the growth of low- k modes.

The dynamics of a combustion front propagating in random media, assuming zero-order kinetics $n = 0$ and for a small Lewis number $\text{Le} = 0.3$, were also studied numerically. The results for early-time evolution show that the most unstable k modes are in the cellular regime, in contrast to the continuum limit, do not follow the linear regime and instead grow non-linearly and develop a complex pattern. This pattern is then subjected to an endless tip splitting and merging and never reaches a steady state. The excited modes seem to follow the linear regime only momentarily after each tip-splitting, which may happen

due to amplitude reduction before and during tip-splitting events. These numerical findings suggest that the destabilizing effect of the random medium, is qualitatively analogous to lowering the Lewis number in the continuum limit. It leads to an increased stability range of modes and an increased growth rate. The late-time dynamics of cellular pattern formation in random media is also investigated. The results indicate that for both uniform and non-uniform random particle distributions, modifying the area fraction of the medium occupied by metal particles (denoted by Φ_s) alters the cell depth (i.e. max-to-min distance of cells). On the other hand, changing the number density N_s reshapes the morphology. For the highest value of number density and area fraction that we could achieve in our simulations, we observed a cellular structure, resembling the seaweed structures obtained in the continuum limit for low Lewis number. By lowering both Φ_s and N_s , the number of cellular branches decreases while the cell-spacing increases. Also we find that the robustness of the cellular patterns against perturbations increases by decreasing the number density. Our numerical analysis for the effect of the Lewis number on the late-time dynamics show that even in the long run, the effect of a random distribution of particles is analogous to low-Lewis numbers in the continuum limit. We show that by increasing the Lewis number, the morphology is changed from a seaweed-like structure to regular shallow cells. This morphology is similar to what we have seen in the continuum limit for high Lewis numbers in the “quasi-linear” regime.

ABRÉGÉ

Les instabilités spatio-temporelles d'un front de combustion gaz/solide, ainsi que motifs résultants, sont examinés dans le cadre des instabilités de la diffusion thermo-massique, dans des milieux continus et hétérogènes. Dans nos simulations numériques, en utilisant un nouvel algorithme de maillage adaptatif, nous atteignons des tailles de systèmes expérimentaux. À notre connaissance, c'est le premier travail où de telles méthodes sont appliquées à cette nouvelle classe de modèles de combustion à gaz/solide.

Nous introduisons un modèle mathématique unifié appelé "modèle principal" pour décrire la combustion des particules de combustible en métal dans le gaz oxydant, en fonction des paramètres physiques du problème (c.-à-d. l'ordre de la réaction chimique ($n = 0, 1$), la température d'allumage T_{ign} et le nombre de Lewis Le, défini comme le rapport de la diffusion thermique à la dispersion de masse), et pour différentes limites de la diffusion de masse d'oxydant, avec des distributions continues et aléatoires de carburant réactif.

Nos résultats numériques pour un front de combustion dans la limite continue montrent que celui-ci développe une front de structure cellulaire pour une température d'allumage T_{ign} , et au-dessous d'un nombre de Lewis critique Le_c . Numériquement, nous trouvons que le régime linéaire de ces morphologies est en accord avec la relation de dispersion prédictive analytiquement par Brailovsky et al.. Les effets de la taille du système, et du nombre de Lewis sont également été abordés. Pour les valeurs du nombre de Lewis proches de la valeur critique Le_c , la transition de linéaire à non-linéaire (dans le régime de longs

temps) est prolongée. Dans ce régime caractérisé par l'apparition de structures à cellules peu profondes, la morphologie du front cellulaire peut être décrite qualitativement en fonction des modes de croissance disponibles dans le régime linéaire. Pour cette raison, ce régime est appelé régime “quasi linéaire”. En abaissant les valeurs de nombre de Lewis au-dessous de $\text{Le} \sim 0.4$, la morphologie du front change significativement et devient complexe, elle est décrite par des cellules profondes non symétriques et des surplombs. Nous avons exploré ce régime hautement non-linéaire et l'influence des effets de taille finie sur la dynamique tardive des divisions et unions cellulaires, en insistant sur les parallèles avec la formation de microstructures en solidification. Les motifs dendritiques simulés dans ce travail sont semblables à ceux observés dans les expériences de propagation de flamme sur un lit de nano-poudre d'aluminium brûlant avec un oxydant à contre-courant menée par Malchi et al. Nous avons étudié le régime linéaire des fronts de combustion cellulaires dans des conditions de dissipation thermique. Nos résultats numériques montrent que le taux de croissance des modes k élevés en présence de dissipation de chaleur, peut être décrit par les mêmes modes que dans l'état adiabatique, mais avec un taux de croissance plus élevé. Cela ressemble essentiellement à abaisser le nombre de Lewis sur le régime linéaire de la combustion adiabatique. Cependant pour les modes k , de faible valeur, un comportement différent est observé lorsque la dissipation de la chaleur est enclenchée. Il est plausible qu'il s'agisse d'un effet de taille finie de nos simulations, qui ralentirait la croissance de bas modes k .

Nous avons également étudié la dynamique d'un front de combustion se propageant dans un milieu aléatoire, en supposant une cinétique de l'ordre zéro et un petit nombre de Lewis $\text{Le} = 0.3$. Les résultats pour l'évolution en stade précoce montrent que les

modes de k les plus instables sont dans le régime cellulaire. Contrairement à la limite continue, ils ne suivent pas de régime linéaire et se développent de façon non-linéaire, développant une structure complexe. Cette structure est ensuite soumise à une continuité de fractionnements et fusions des pointes et n'atteint jamais un état stationnaire. Cependant, les modes excités semblent suivre le régime linéaire momentanément après chaque fractionnement, probablement en raison de la réduction d'amplitude avant et pendant un événement de fractionnement de pointe. Ces résultats numériques suggèrent que l'effet déstabilisateur du milieu aléatoire, est qualitativement analogue à l'abaissement du nombre de Lewis dans la limite du continue, menant à l'augmentation de la plage de stabilité des modes et de leur taux de croissance. La dynamique tardive de la formation de motifs cellulaire dans les milieux aléatoires est également étudiée. Les résultats indiquent que, pour des échantillons uniformes et non uniformes de particules aléatoires, la modification de la fraction de surface du milieu occupé par les particules métalliques (notées par Φ_s) modifie la profondeur des cellule (c'est-à-dire la distance max-min des cellules). De l'autre côté, changer la densité de nombre N_s altère la morphologie. Pour les valeurs de densité de nombre et de fraction de zone les plus élevées que nous avons pu atteindre dans nos simulations, nous avons observé une structure cellulaire, ressemblant aux structures d'algues pour le nombre Lewis bas dans la limite de continue. En abaissant les deux paramètres Φ_s et N_s , le nombre de branches cellulaires diminue alors que l'espacement cellulaire augmente. Aussi, nous trouvons que la robustesse d'un motif cellulaire contre les perturbations augmente en diminuant la densité de nombres. Notre analyse numérique de l'effet du nombre de Lewis sur la dynamique de temps longs, montrent qu'une distribution aléatoire des particules est analogue à l'effet d'un nombre de Lewis faible dans la

limite du continue. Nous montrons qu'en augmentant le nombre de Lewis, la morphologie passe d'une structure semblable à celle des algues à des cellules peu profondes. Cette morphologie est semblable à ce que nous avons vu dans la limite du continue pour les nombres Lewis élevés dans le régime “quasi linéaire”.

TABLE OF CONTENTS

ACKNOWLEDGEMENTS	ii
CONTRIBUTIONS OF AUTHORS	iii
ABSTRACT	iv
ABRÉGÉ	vii
LIST OF FIGURES	xiv
1 Introduction	1
1.1 Pattern formation:	1
1.1.1 Instabilities and pattern formation in Reaction Diffusion (RD) systems	4
1.1.2 Applications of pattern formation in RD systems	8
1.1.3 Modelling of RD systems	9
1.1.4 Self-Sustained RD fronts	11
1.1.4.1 Isothermal chemical fronts	11
1.1.4.2 Non-isothermal chemical fronts	14
2 Overview of modelling combustion systems: continuum and discrete limit . . .	35
2.1 Review of reaction rate kinetics	35
2.1.1 Model derivation	38
2.1.2 Specializing the model for kinetic-limited reaction rate	40
2.1.3 Specializing the model for diffusion-limited kinetics	42
2.1.3.1 General expression of a single particle burning rate . . .	42
2.1.3.2 Combustion of a particle surrounded by a cloud of particles	43
2.1.4 Master model for continuum and discrete solid fuel distribu- tions	46
2.1.5 Special Limits of the Master Model Equations	54
2.2 Summary	58

3	Cellular instabilities of Continuum Combustion fronts	59
3.1	Analysis of Cellular Flame Front Instability- Adiabatic case	60
3.1.1	Numerical Methods	60
3.1.2	Linear regime	62
3.1.2.1	Effect of system size on linear mode selection	65
3.1.2.2	Effect of Lewis number on linear mode amplitudes	67
3.1.3	Quasi-Linear Regime as $Le \rightarrow Le_o$	68
3.1.3.1	Effect of initial condition and system size on the dynamics of the interface	68
3.1.3.2	Effect of Lewis number on the morphology	78
3.1.4	Non-Linear Front Dynamics for Small Le : Seaweed Fronts	79
3.2	Adding Thermal Dissipation to the Master Model Equations	86
3.2.1	Derivation of linear dispersion-relation with thermal dissipation	89
3.2.2	Numerical linear dispersion-relation with thermal dissipation . .	93
3.2.3	Summary	95
4	Cellular instabilities of combustion fronts in random discrete media	99
4.1	Analysis of cellular flame front instability- Adiabatic random discrete case	101
4.1.1	Numerical method to study cellular flame front instability in random media	103
4.1.1.1	Numerical representation of discrete particle	104
4.1.1.2	Sampling random dispersion of fuel particles	104
4.1.2	Cellular combustion front in random media: Early-time regime	108
4.1.3	Effect of Lewis number: Correspondence between pattern formation in discrete random and continuum-limit media	114
4.2	Cellular combustion front in random media: Late-time regime	118
4.2.1	Effect of stochastic nature of particle system on cellular fronts .	119
4.2.2	Effect of Lewis number on the late-time dynamics of a cellular front	125
4.2.3	Effect of uniformity of a random particle distribution of cellular patterns	128
4.3	Summary	133
5	Conclusion	136

A	Derivation of combustion equations in a discrete heterogenous medium using one particle combustion in hot oxidizer gas	143
A.1	One particle combustion in the presence of oxidizer	144
	A.1.1 Combustion of cloud of particles	151
A.2	Derivation of combustion equations with heterogeneous random media .	156
	A.2.1 Deriving equations for discrete combustion in the limit of $n = 0$ and Le finite	158
	A.2.1.1 Deriving equations for discrete combustion in the limit of $n = 0$ and $\text{Le} \rightarrow \infty$	160
	A.2.2 Deriving equations for discrete combustion in the limit of $n = 1$ for both Le finite and $\text{Le} \rightarrow \infty$	161
B	Derivation of effective medium version of discrete combustion equations, and the derivation of the Continuum Master Equations	163
B.1	Effective medium derivation	164
	B.1.1 Master model derivation	167
C	Linear Stability Analysis for Master Model equations with dissipation	171
C.1	Deriving steady-state solutions and dispersion relation for dissipative combustion model	172
References	181

LIST OF FIGURES

Figure	page
1–1 Schematic diagram of the thermal structure of a combustion front.	15
1–2 Classification of different combustion systems with respect to the reaction kinetics and Lewis number.	21
2–1 Numerical and analytical steady-state profiles of dimension-less temperature and concentration fields for MM($n = 1$; $\text{Le} = 0.75$; $\theta_{\text{ign}} = 0.75$).	53
2–2 Dimension-less temperature profile for a zero-order kinetics combustion front in the absence of mass diffusion.	56
3–1 Linear growth rate ω normalized with the characteristic time τ versus the wavenumber k of the perturbation normalized by $\delta_c/2\pi$	64
3–2 The normalized spectral power of the 1D interface $x = f(y, t)$ with model parameters MM($n = 1$; $\text{Le} = 0.6$; $\theta_{\text{ign}} = 0.75$).	66
3–3 Stability space for MM($n = 1$; Le ; $\theta_{\text{ign}} = 0.75$) for $\text{Le} < \text{Le}_o$ where the horizontal axis is the parameter ε defined as $(\text{Le}_o - \text{Le})/\text{Le}_o$ and the vertical axis is the wavenumber k normalized by $\delta_c/2\pi$	69
3–4 Contours of the dimension-less temperature field in a moving frame for model parameters MM($n = 1$; $\text{Le} = 0.6$; $\theta_{\text{ign}} = 0.75$) and system size $L_y = 80\delta_c$	70
3–5 The sequence of the time evolution of the front, defined by the isotherm $\theta(x, y) = \theta_{\text{ign}} = 0.75$ in Fig. 3–4.	71
3–6 Evolution of the dimension-less temperature field for model parameters MM($n = 1$; $\text{Le} = 0.6$; $\theta_{\text{ign}} = 0.75$) from (a): the initially perturbed front with wavelength $\lambda = 80\delta_c$ to (h): the final state in the computation.	72
3–7 Contour plots of dimension-less temperature field for model parameters MM($n = 1$; $\text{Le} = 0.6$; $\theta_{\text{ign}} = 0.75$) in the system $L_x = 2000$ and $L_y = 320$	75

3–8 The normalized spectral power of the interface $x = f(y, t)$ of the steady-state for the two different initial perturbation modes in Fig. 3–7: $k_8 = 0.05\pi/\delta_c$ (■) and $k_4 = 0.025\pi/\delta_c$ (*).	76
3–9 Temporal history of evolution of 1D front corresponding to isotherm $\theta(x, y) = \theta_{\text{ign}}$ for model parameters MM($n = 1; \text{Le} = 0.6; \theta_{\text{ign}} = 0.75$) with initial morphologically noisy interface and in the system size $L_x = 5000 \delta_c \times L_y = 320 \delta_c$	77
3–10 The normalized spectral power of the interface $x = f(y, t)$ for model parameters MM($n = 1; \text{Le} = 0.6; \theta_{\text{ign}} = 0.75$): a) $L_y = 80 \delta_c$ at $t = 76\tau$, b) $L_y = 320 \delta_c$ at $t = 69\tau$	78
3–11 Amplitude of cellular pattern for model parameters MM($n = 1; \text{Le}; \theta_{\text{ign}} = 0.75$) for range of Lewis numbers $0.1 \leq \text{Le} \leq 0.6$	80
3–12 Cell depth parameter h in units of δ_c versus Le.	81
3–13 (Colour online) Temporal history of evolution of 1D front corresponding to isotherm $\theta(x, y) = \theta_{\text{ign}}$ for model parameters MM($n = 1; \text{Le} = 0.05; \theta_{\text{ign}} = 0.75$) with initial sinusoidal wave mode $k = 0.05\pi/\delta_c$ and in the system size $L_x = 600 \delta_c, L_y = 80 \delta_c$	82
3–14 (Colour online) Temporal history of evolution of 1D front corresponds to isotherm $\theta(x, y) = \theta_{\text{ign}}$ for model parameters MM($n = 1; \text{Le} = 0.05; \theta_{\text{ign}} = 0.75$).	84
3–15 One dimensional analytical solutions for the dissipative model MM($n = 1; \text{Le} = 0.75; \theta_{\text{ign}} = 0.75, \Gamma = 0.01$)	88
3–16 Dispersion relation for MM($n = 1; \text{Le} = 0.6; \theta_{\text{ign}} = 0.75, \Gamma = 0.01$).	95
4–1 Amplitude of a combustion front propagating in a uniform random media with parameters $\Phi_s = 0.7, N_s = 16$ and for model parameters MM($n = 0; \text{Le} = 0.3; \theta_{\text{ign}} = 0.75$).	110
4–2 The normalized spectral power of 1D interface $x = f(y, t)$ at $t = 30\tau$ for model parameter MM($n = 0; \text{Le} = 0.3; \theta_{\text{ign}} = 0.75$) corresponding to a uniform random heterogenous medium with ($\Phi_s = 0.7, N_s = 16$).	111
4–3 Dispersion relation for model parameters MM($n = 0; \text{Le} = 0.3; \theta_{\text{ign}} = 0.75$).	113

4–4 Temporal history of evolution of 1D front $x = f(y, t)$ corresponds to isotherm $\theta(x, y) = \theta_{\text{ign}}$ for model parameters MM($n = 0$; $\text{Le} = 0.3$; $\theta_{\text{ign}} = 0.75$) and for a uniform random particle distribution	121
4–5 The spectral power of the interface $x = f(y, t)$ of combustion fronts in Fig. (4–4) taken at $t = 30\tau$ for model parameters MM($n = 0$; $\text{Le} = 0.3$; $\theta_{\text{ign}} = 0.75$) and for a uniform random heterogenous medium with a) $\Phi_s = 0.7$, $N_s = 16$; b) $\Phi_s = 0.7$, $N_s = 4$; c) $\Phi_s = 0.4$, $N_s = 4$; d) $\Phi_s = 0.4$, $N_s = 16$	122
4–6 Temporal history of evolution of 1D front corresponds to isotherm $\theta(x, y) = \theta_{\text{ign}}$ for model parameters MM($n = 0$; $\text{Le} = 0.45$; $\theta_{\text{ign}} = 0.75$) and for a uniform random particle distribution with $\Phi_s = 0.7$ and for $N_s = 16$. The direction of front propagation is shown by the dashed arrow.	126
4–7 The spectral power of the interface $x = f(y, t)$ of combustion front in a random media with identified by ($\Phi_s = 0.7$; $N_s = 16$) and for model parameters MM($n = 0$; $\text{Le} = 0.45$; $\theta_{\text{ign}} = 0.75$).	127
4–8 Contours of the dimension-less temperature field for model parameters MM($n = 0$; $\text{Le} = 0.3$; $\theta_{\text{ign}} = 0.75$) and in a non-uniform random medium with ($\Phi_s = 0.4$; $N_s = 1$).	129
4–9 Temporal history of evolution of 1D front $x = f(y, t)$ corresponds to isotherm $\theta(x, y) = \theta_{\text{ign}}$ for model parameters MM($n = 0$; $\text{Le} = 0.3$; $\theta_{\text{ign}} = 0.75$) and for a non-uniform random particle distribution.	132

CHAPTER 1

Introduction

1.1 Pattern formation:

Spontaneous pattern formation is a hallmark of systems out of equilibrium. These systems, which typically exchange energy and/or mass with their environment by some form of transport like heat conduction or mass diffusion, are referred to as open, dissipative systems. Under these constraints of mass/energy flux, a system may lose its stability against arbitrary small perturbations and develop temporal or spatial patterns. In closed, non-dissipative systems where both mass and energy are conserved, any possible initial spatial disturbances, on the contrary, will decay in the long run and a spatially homogenous thermodynamic equilibrium state develops. This, in fact, is in agreement with second law of thermodynamics that states the entropy in closed system, increases until thermodynamic equilibrium is established [11]. Pattern formation in systems out of equilibrium has been widely studied both experimentally and theoretically. Theoretical predictions in pattern formation have typically been difficult to realize in experiments. The main reason may be attributed to the fact that past experiments have been closed to both energy and mass and thus initial disturbance are smoothed out on time-scales considerably smaller than the time scale for pattern formation to develop. For example, spatial Turing patterns [177] in auto-catalytic reactions verified experimentally only when these chemical reactions conducted in open reactors. Nonetheless, zero-flux conditions in close systems do not seem to prevent pattern formation if chemical reactions take place in a narrow region between reacted

and fresh mixtures (a chemical front). In these chemical reactions, small length-scale of chemical front compared to dimensions of the systems in which they propagate, mimics the similar conditions of chemical reactions in open systems, and thus even local flux of energy/mass can drive the system interfaces out of equilibrium (see [70]).

Pattern formation due to the instabilities of moving fronts has been observed in different physical, chemical, and biological systems. Propagating fronts emerge in dynamic processes where two distinct phases are separated by an interface. They are observed in nature in a variety of applications ranging from chemical and biological systems to material sciences. In general interfaces may exhibit rich and complex spatiotemporal instabilities and, although different in their underlying physical and chemical mechanisms, can be studied in the unifying framework of less (or non) reactive growth systems and reaction-diffusion systems.

Instabilities of propagating fronts in the diffusion-driven growth systems, are tackled in the context of diffusive instabilities. The growth process, in these systems, is described by the governing scalar fields (e.g. Pressure, Temperature), whose dynamics near a moving interface are related to their Laplacian in a layer limited by a diffusion length. When the diffusion length is much smaller than the length scale of the domain, the system boundaries do not have a notable effect on the growth process and thus will be disregarded. In the other limit, however, where the diffusion length is on the order of the system size, the problem goes over to the so called “Stefan problem” [156, 72, 20]. In this case, the interface growth process is sensitive to boundary conditions, and the shape and velocity of the front can be derived from the Laplacian fields self-consistently satisfying boundary

conditions far from the interface and at the moving interface itself [34]. Examples include directional solidification of binary alloys [92], nematic-isotropic transition in liquid crystals [53], viscous fronts [34], diffusion limited aggregation [188]. In these cases, a steady-state propagating front under certain conditions can undergo spatiotemporal instabilities whose length-scales are determined by various parameters like imposed gradient of temperature in solidification and liquid crystals [92, 53], system size in viscous fingering [34] or front velocity in eutectic growth [152]. The competition between imposed and emergent length-scales during the growth process results in different front morphologies ranging from stable front to fractal patterns [34].

Not all pattern formation is due to purely diffusive effects. Some studies have shown that another distinct type of instability appears when rate of generation (consumption) of diffusing species (e.g. concentration of reactants in chemical reactions or population of species in population dynamics) is coupled to their diffusivity. The class of systems that exhibit this type of coupling are referred to as the *reaction-diffusion (RD)* systems. Auto-catalytic reactions [99], combustion fronts [192], and calcium waves [140] are among the well-known examples of these systems in chemistry and biology. Classical RD equations typically contain a diffusion equation to propagate diffusing quantities such as temperature, pressure or some reactive species. The diffusion equation contains a source (sink) term to account for the generation/depletion of heat or mass in/out of the system during a reaction. The source/sink terms in population dynamics, for instance, represents interactions among species [131], while in chemically reactive propagating waves, they describe heat release during the reaction, which then contributes to molecular diffusion of reactants

and products [99]. The sink/source term in RD equations is typically coupled to a non-conserved order or reaction parameter that follows its own equation and tracks interfaces between reacted and non-reactive media, different species, etc. Instabilities in RD systems arise from special form of kinetics (like autocatalysis) or from a spatial decoupling of key species, known as the *activator* and *inhibitor* species, by some form of transport like diffusion [71]. These instabilities are ascribed to different diffusivity of inhibitor and activator. These type of processes are common in biological and chemical systems [129, 177]. For instance, in the case of autocatalytic chemical systems, autocatalytic species that promote reaction are activator and those that act to inhibit autocatalysis are called inhibitor species. The inhibitor may be produced by the autocatalytic process or it may be simply a stoichiometrically deficient reactant of that process.

1.1.1 Instabilities and pattern formation in Reaction Diffusion (RD) systems

Research in pattern formation mainly aims to address the questions of under what conditions and how transitions from homogenous state (or steady-state solutions) to pattern occur. These transitions which are triggered by instabilities or bifurcations can be classified, in a similar way as phase transition, into continuous (supercritical) and discontinuous (subcritical) instabilities analogously to first order or second order phase transitions [35]. Theses instabilities can either result in “spatial” patterns, wherein a spatially heterogeneous pattern emerges with a defined wavelength such as Turing patterns; or “spatiotemporal” patterns, in which the pattern can vary periodically in time as well as having a defined spatial length-scale. Patterning in RD systems occurs when the uniform steady

state loses stability as a control or bifurcation parameter passes through a critical value.¹ When this critical value is reached, the characteristic wavelength of the linearly unstable pattern and its period (in the case of spatiotemporal patterns), in general, can be calculated in terms of the parameters of the model. The specific type of emergent pattern depends on the parameter space of the system under consideration. For instance, an oxidation front propagating in a combustible mixture, can develop a stationary cellular and dynamic oscillatory (wave-like) patterns, for small and large values of oxidizer mass diffusivity (D) compared to the mixture's thermal diffusivity (α), respectively. Cross and Hohenberg [35], in their review article on pattern formation, classified the patterns in RD systems into three main groups: (I) spatially periodic and stationary in time (Turing instabilities), (II) spatially periodic and oscillatory in time (wave instabilities) and (III) spatially homogeneous and oscillatory in time (Hopf bifurcation).

Morphological patterns in reaction-diffusion systems trace their origin back to the work of British mathematician Alan Mathison Turing who considered the “Chemical Basis of Morphogenesis” [177] and showed that the interplay of nonlinear reaction and diffusion transport may lead to sustained stationary concentration patterns, henceforth often called “Turing structures”. In his theoretical work, Turing demonstrated that a system of reacting and diffusing chemicals could spontaneously evolve to spatially heterogeneous patterns from an initially uniform state in response to infinitesimal perturbations. He specifically

¹ The term “critical” here is general not intended to solely imply that all such transition points in RD systems as “critical” in the sense implied in phase transformations.

considered a system of two chemicals, and explained the instabilities in term of activator-inhibitor systems. Turing showed that if the diffusion of the inhibitor was greater than that of the activator, then diffusion-driven instability could result in pattern formation. This, however, opposes the intuitive perception of diffusion as a homogenizing process[102]. Since Turing’s paper, there has been a vast body of literature on both the theoretical and practical aspects of RD systems [50, 131, 47, 25, 153]. Turing models have been applied to such diverse areas as ecology [154], semiconductor physics [102]), material sciences [90, 57], hydrodynamics [183], astrophysics [133], and even economics [113]. The first experimental evidence of the existence of Turing structures was presented by De Kepper’s group [38], nearly forty years after the original theory.

Some systems that become unstable and exhibit time-dependent oscillatory patterns do so through the mechanism of a Hopf bifurcation. This mechanism has been studied in such systems for many years. In chemical systems, for instance, the best known oscillatory reaction is the Belousov-Zhabotinsky reaction [17, 99]. This system also exhibits a number of different types of wave structures, such as propagating fronts, spiral waves, target patterns and toroidal scrolls[190, 185, 186, 187, 78, 182].

Other than patterns whose characteristics can be mainly determined by few quantities like speed, wavelength, and frequency, the emergence of complex patterns in reactive media can also be attributed to the following phenomena: i) combination and interaction of simple patterns, ii) chaos and bifurcation, and iii) interaction of patterns with external perturbations and noise.

An interesting example of type (i) is a combination of localized and periodic patterns which gives rise to new complex patterns such as a rotating spiral, consists of a well-defined rotation centre (point-like centre or “core” in 2D, and line-centre or “filament” in 3D), from which periodic waves emitted in all radial directions [11]. Rotating spiral waves observed in the experiment of the catalytic reduction of NO with CO on a platinum surface [178]. The same phenomena arises in the aggregation of slime molds colonies where spiral waves of chemoattractant are observed in the early aggregation stage [49, 93]. More reviews on these patterns can be found in [157, 77]. Another particularly interesting example of combinatory instabilities appears when Turing and Hopf bifurcation modes emerge simultaneously at the so-called Turing-Hopf bifurcation point [41]. Interaction and competition between Turing and wave-like instabilities is also investigated numerically by Bar et al. [11].

Spatiotemporal chaotic patterns in reaction-diffusion systems of type (ii) are among the most widespread examples of complex patterns. For example, the analysis of pattern formation in the quasi-two-dimensional Belousov-Zhabotinsky reaction, reveals that this system can undergo spatiotemporal chaos [194].

Pattern formation can also be influenced as a result of constructive or destructive interplay between external manipulation (noise or perturbation) and dynamics of underlying self-sustained processes.

An example of type (iii) can be found in the light-sensitive Belousov-Zhabotinsky reaction [144]. The time-periodic forcing with light changes the pattern from perfectly periodic waves to a disordered labyrinthine pattern. A large variety of other patterns have been obtained upon changes of the frequency and amplitude of the illumination.

More examples of complex patterns in RD systems are three-dimensional patterns consisting of parallel lines of periodic spots , hexagons, rhombic pattern and special complex pattern referred to as “black-eye” which are observed in experiments of “The chlorite-iodide-malonic acid-starch reaction” [38, 39, 136, 181, 135, 64]. It is noteworthy that regardless of their complexity, the simple activator-inhibitor picture as well as the concept of an excitable medium could be used to explain the patterns that emerge in these examples.

Complex patterns in exothermic RD systems such as combustion fronts have also been extensively investigated. This Thesis will investigate new properties of such systems using a new class of RD equations to describe combustion. In chapter 3 we show how simple cellular fronts, obtained certain range of model parameters and system size, can transition to a complex [apparently] chaotic cellular or dendritic seaweed patterns. The effect of external noise (random particle distribution) in combustion front pattern formation will also be studied in chapter 4.

1.1.2 Applications of pattern formation in RD systems

Pattern forming in complex system has numerous applications in science and technology. One application, for instance, is their abilities to generate and propagate a respond to a small stimuli from the environment in a fast and reliable fashion. Reaction-diffusion system, as an excitable media, has two stable rest and excited states. Perturbations larger than the threshold may cause a large response, while small perturbations and noise decay immediately. Super-threshold perturbations lead via diffusion to propagation of fast reaction-diffusion waves that transmit information in a reliable fashion. Propagation of

action potential in response to a small change in potential of the neural membrane, is a good example of this ability in neural networks of the brain. Reaction-diffusion systems are also capable of developing stationary periodic patterns such as Turing structures in autocatalysis or cellular patterns in chemically reactive waves where the former may play an important role in morphogenesis and the evolution of structures in living organism, and the latter has some applications in material and chemical sciences. Other types of dynamic instabilities of chemically reactive fronts, such as wave, and oscillatory instabilities are also proposed as efficient methods to synthesize novel materials with functionally graded mechanical, electrical and/or heat transport properties. Examples of these methods can be found in the literatures of Combustion Synthesis (CS) or Self-propagating High-temperature Synthesis (SHS) [123, 74].

1.1.3 Modelling of RD systems

Historically, the earliest model for a two-dimensional excitable medium is a cellular automaton model for the propagation of electrical activity in heart muscle [184] proposed by Wiener and Rosenblueth in 1946. First two pioneering works on RD systems were conducted in 1952 in chemical systems by Turing [177] and physiological systems by British physiologists A. L. Hodgkin and A. F. Huxley. The latter were the first examples of models of an excitable medium derived from underlying physico-chemical processes. They derived a set of ordinary differential equations from measurements of ionic currents at the membrane of the squid giant axon [69], neglecting spatial variations. Their nobel-prize-winning effort is still considered the “most successful model in physiology” [84]. Since the Hodgkin-Huxley equations, many of the subsequently developed models for

membrane potentials are coupled nonlinear ordinary differential equations. These have largely resisted analytical treatment and have been mostly studied numerically [84]. A highly simplified version has been derived by R. FitzHugh and J. Nagumo in the early 60s. It is known as the FitzHugh-Nagumo model [52] and reads :

$$\begin{aligned}\frac{du}{dt} &= f(u, v) = -\frac{u^3}{3} + u - v, \\ \frac{dv}{dt} &= \epsilon g(u, v) = \epsilon(u - \gamma v + \beta)f(u, v).\end{aligned}\tag{1.1}$$

where ϵ , γ and β are parameters of the model. Originally, the activator u is derived from the voltage V of the Hodgkin-Huxley equations, while the inhibitor v represents a type of slow gating variable n [84]. To allow for spatial variation in the variables u and v , it is possible to add transport by diffusion, thus obtaining a coupled set of nonlinear partial differential equations of the form

$$\begin{aligned}\frac{\partial u}{\partial t} &= D_u \nabla^2 u + f(u, v), \\ \frac{\partial v}{\partial t} &= D_v \nabla^2 v + \epsilon g(u, v).\end{aligned}\tag{1.2}$$

A nice feature of the FitzHugh-Nagumo model is that it contains both the Turing patterns and the excitable medium as special cases depending on the choice of the parameters. Despite its ability to describe the essential features of reaction-diffusion systems, many real systems like action potential propagation [124], calcium waves [84] or catalytic CO oxidation [12] do not follow the simple linear relation for the inhibitor production v in the FHN equations, but rather more complicated nonlinear dependencies. Since Turing's paper, several RD models have been considered with non-linear kinetic terms. These models are more realistic since their solutions evolve to bounded values, and are derived

essentially in three different ways: (i) phenomenologically, (ii) to model a hypothetical reaction and (iii) empirically.

Propagating reaction-diffusion fronts were first considered by Luther [101, 9], followed by theoretical treatments by Fisher [51], and Kolmogrov et al. [89] about 30 years later. Fisher and Kolmogrov et al. formally studied the propagating front with quadratic kinetics, which is the typical kinetics of chemical propagating waves in biological science. Propagating fronts with cubic kinetics is also first studied by Semenov [179] in 1939. Review of these models can be found in [58, 150, 174].

1.1.4 Self-Sustained RD fronts

One important class of RD systems is self-sustained chemical reaction fronts which can be classified into Isothermal and non-isothermal fronts. Advances in reaction-diffusion theory along with connections between isothermal fronts and non-isothermal chemical front propagation are well described in this review [151]. In what follows, we briefly illustrate each case together with their instabilities and pattern formation.

1.1.4.1 Isothermal chemical fronts

Isothermal fronts appear in chemical systems, where the locally initiated reaction, propagates through a fresh reactant, via diffusion process, and leaves products behind. The “isothermal fronts” emerge in this process are much like flame fronts, but with no heat. These chemical fronts are common in autocatalytic chemical reactions, when autocatalytic reaction couples with diffusion to produce self-sustaining fronts that propagate

with constant velocity and waveform. Examples of autocatalytic reactions which can support propagating front are reviewed in [99].

Isothermal reaction-diffusion fronts may exhibit complex patterns. For instance, propagating autocatalytic chemical fronts, under conditions when diffusivity of the reactant differs from that of the autocatalyst, become unstable and develop patterns[70]. Scott et al. [151] show that complex behaviour, including spatiotemporal chaos, may arise from the coupling of diffusion and simple autocatalysis in a two-dimensional medium. In another study, Horvath et al. [70] examine the conditions for onset of these instabilities. In their studies, Horvath et al. illustrate the general features of reaction-diffusion fronts, specifically for autocatalytic chemical fronts, by assuming three nonlinear forms for reaction kinetics such as quadratic, cubic, and combination of both (mix-order kinetics). Their results indicate that in general, the narrow reaction zone assumption, similar to the assumptions on which the Kuramoto-Sivashinsky theory for combustion front is based, holds only approximately for mixed-order autocatalysis fronts. The assumption of narrow reaction zone is better presented by higher-order autocatalysis, which mimics the Arrhenius temperature dependence more closely and produces narrower reaction fronts similar to those in flame propagation.

In these isothermal systems, local diffusion of an autocatalyst into the fresh reactant ahead of the front results in bulged segments in the direction of propagation. In these convex regions, the dispersion of autocatalytic agents is enhanced compared to a planar front. This, effectively, weakens the driving force for reaction ahead of the front, thereby reducing the wave speed relative to the planar wave speed. The situation is reversed for retarded segments of a front, where the total density of autocatalytic agent is increased

due to enhanced diffusion, leading to increase in local wave speed. These local increases and decreases tend to eliminate the effect of local curvature and thereby stabilize a planar wavefront [70]. Diffusion of reactant, on the hand, tends to oppose the aforementioned effects of autocatalysis. The local speed of advanced (retarded) segments are increases (decreases) due to enhanced (reduced) diffusional supply of reactant into a front, which in effect promote the instability and thus has a destabilizing effects [70]. According to their analytical results on a chemical front with mixed-order kinetics, Horvath et al. [70] showed that the destabilization of a planar front occurs when the diffusivity of the reactant exceeds that of the autocatalyst by a critical ratio, whose exact value depends on the relative contributions of the cubic and quadratic terms in reaction kinetics [70]. Furthermore, their results suggest that destabilization effects are present only if the kinetics include the cubic term and quadratic autocatalysis alone is not sufficient for the evolution of nonplanar fronts. The requirement of a retarded diffusion of the autocatalytic species relative to that of the reactant is similar to the condition for the establishment of Turing patterns in finite geometries [132, 131] which are also realized in experimental studies [29, 136, 94, 48]. Although the non-planar wave front has many characteristics of a propagating Turing pattern, there are important differences. For example, in the Turing case, nonplanar fronts arise from simple autocatalysis rather than specific non-linear reaction kinetics. Other than the stationary Turing-like patterns, a steady nonplanar isothermal fronts may lose stability, leading to temporal oscillatory behaviour. This is because of the special form of kinetics that supports oscillatory behaviour in homogeneous reaction mixtures[70].

1.1.4.2 Non-isothermal chemical fronts

Non-isothermal flame fronts are another class of propagating RD fronts where propagation of chemical front accompanied by heat release from an exothermic chemical reaction, such as oxidation. The reaction heat thus diffuses away towards the fresh mixture, raising its temperature which is followed by the subsequent chemical reaction. In analogy with isothermal fronts, in non-isothermal fronts and in the absence of convective effects, thermal feedback through exothermic heat release and temperature-dependent reaction rate, couples with thermal diffusivity (conduction).

One of the best known examples of self-sustained non-isothermal chemical front is the combustion front. Forest fires, gas flames, and gas-less combustion systems are among the well-known examples of the combustion process. In following section modelling, applications, and instabilities of combustion flames will be discussed in more detailed fashion.

Self-sustained combustion fronts

Combustion is a process of fast oxidation involving fuel and an oxidant. It is an exothermic chemical reaction with substantial heat release, which through the competition between heat dissipation and mass transport can form a self sustaining propagating front. Propagation of a combustion wave is one of the possible modes for a combustion reaction. The stationary-flame frame around the flame, is depicted in Fig. (1–1). As it is shown in the figure, the reactant with relatively low initial temperature, T_0 , flows toward the stationary flame with speed u_0 and products are withdrawn from the stationary flat combustion zone with speed, usually, different than u_0 (Fig. 1–1). The reactive mixture is separated from the high-temperature reaction products, T_b , by a narrow combustion zone

and a relatively larger preheat zone. In real systems, however, the directions of the initial mixture flow and the normal to the combustion front do not coincide, and thus the combustion front is not generally flat [121].

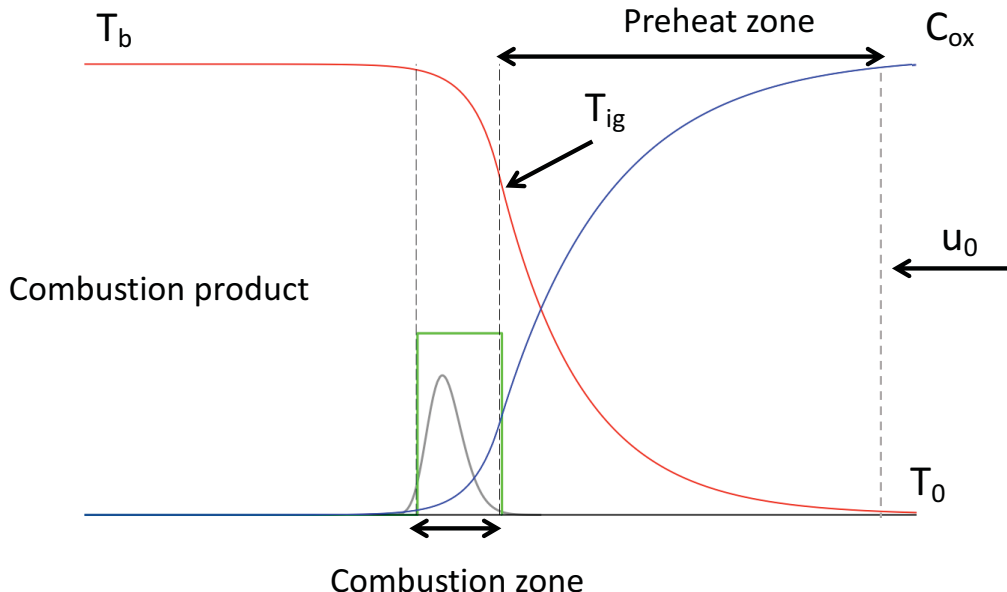


Figure 1–1: Schematic diagram of the thermal structure of a combustion front. In the figure steady-state temperature profile is specified by (red solid line), and concentration of oxidizer is shown by (blue solid line). Two common reaction rates; Arrhenius kinetics (gray solid line), and stepwise kinetics (green solid line), are depicted in the reaction zone. In this diagram the combustion flame is assumed to be stationary.

Another possible scheme for the process of combustion front propagation occurs when the combustion zone propagates into the initially stationary reactive media with a fixed relative velocity u . This velocity is called “normal combustion velocity”.

Combustion systems, based on the phases of reactants and products, can be classified into gaseous (where both reactants and products are in gaseous phase), solid-gas (where solid fuel particle distributions react in the presence of a gaseous oxidizer in which they are dispersed) and gas-less solid fuel combustions. The latter includes a process whereby

a solid mixture is converted directly into more stable solid solution, without a gaseous reactant and even without any gaseous product. Solid "combustion" of this form has applications in materials science, including in the synthesis of metal alloys, ceramics and superconductors [74]

Reactive combustion fronts have broad applications in technology. e.g. gaseous mixtures of hydrocarbons with air are utilized in various spark-ignition engines, jet propulsion engines, etc.[97, 165]; explosives, gun powders and solid rocket propellants [7, 18]; fine sprays and dusts in engines and furnaces [143, 86, 88]; systems for synthesizing refractory compounds in the combustion zone [118, 21, 116]; for producing some metals, alloys and added metals [145, 149, 46], for production of acetylene and of various grades of soot by incomplete oxidation of hydrocarbons [8].

A combustion phenomenon of particular interest is that of solid-gas combustion. This phenomenon is fundamental to "combustion synthesis" (CS) [74] and "Self-propagating High-temperature Synthesis" (SHS) [123]. These processes are fast and energetically economical compared to similar traditional techniques and yield high purity products. Some of the main advantages of SHS, and its history, are reviewed in [123].

Theory of combustion phenomena

Despite the great deal of mechanisms and parameters rendering combustion wave propagation as a complicated phenomena which results in the existence of numerous theories, it has been shown that the theory of combustion front propagation can be divided into two main parts: "physico-chemical" and "fluid-dynamic" [121]. The combustion front is the realization of exothermic chemical reaction occurring with heat and mass transport, which

leads to heat generation and temperature rise. The theory of physico-chemical is developed to study the underlying coupled chemical and heat/mass transport processes in order to determine the thermal structure, velocity and thermal instabilities of combustion waves, both for homogeneous and heterogeneous reactant distributions. The reciprocal effects of flow field and combustion wave and their couplings, are fully treated in the fluid-dynamic theory [91, 97, 109, 168, 76, 121].

Studying the effects of fluid-flow on combustion wave requires consideration of different length-scale phenomena. When the characteristic length-scale of combustion wave (usually on the order of few millimetres), is significantly smaller than fluid-dynamic dimensions, it is possible to decouple these two problems and study flame front velocity and structure independently from its underlying flow-field. In this situation the fluid-dynamic velocity gradient (across the flame width) is small [121]. However, there are several cases where it is impossible to separate the fluid-dynamic and physico-chemical aspects of the phenomena. A “Flame-stretch”, and dependence of front velocity on the flame front curvature, are well known examples of such a strong coupling. More details of these instances can be found in[121].

Physico-chemical theory of combustion front

The mathematics of solid-gas and gas-less solid combustion processes can generally be described in the framework of reaction-diffusion equations that integrate heat and mass diffusion with the detailed chemical and thermodynamic characteristics of the reaction process and reactant materials. In recent years, numerous models have been introduced to

describe such combustion processes. While apparently disparate, the various models generally describe such combustion phenomena based on (1) the heterogeneity of the solid medium through which the combustion wave is propagating, (2) the rate and the order of chemical reaction (oxidation in this case), (3) heat transport, and (4) diffusion of oxidizer. The relative importance of (3) and (4) is typically of fundamental importance and is characterized through the Lewis number.

Effect of heterogeneity of combustible medium

Based on the distribution of combustible media, the combustion process can be divided into two classes, namely, homogenous and heterogeneous combustion.

In the case of homogeneous combustion, the combustible mixture (chemical reactants) is uniformly distributed in space and remains uniform throughout the process. In this regime of combustion the rate of chemical reaction and heat generation is represented by a spatially-homogenized function which is not essentially affected by transport and mixing of components. Homogeneous combustion comprises exothermic chemical reactions of condensed and/or gasified species.

Among all homogenous combustion systems, much of the effort to understand the underlying mechanisms of combustion, and in particular the role of thermo-diffusive instabilities, has focused on systems of “premixed flames”² where reactants are in gaseous phase. This study will include an examination of premixed flames wherein solid fuel reactant particles undergo oxidation with gaseous oxidizer.

² In premixed flame, reactants and oxidizer are mixed prior to combustion.

Combustion systems in the heterogeneous limit are macroscopically non-uniform either due to an initial distribution of reactants or microscopic structure of a combustible media in which the combustion front propagates. The rate of combustion in heterogenous media, in contrast to the homogenous case, is strongly limited by transport of reactants. Heterogenous combustion system include various condensed and disperse systems with different properties and modes of burning (various fuel droplets in a gaseous oxidizer, porous fuels into which the oxidizer is fed by infiltration, etc.).

The effect of heterogeneity of reactant medium has been investigated in numerous experimental and theoretical studies. Typically, the analysis of pattern-forming models is carried out assuming an effectively homogenous initial conditions and model parameters. In the case of reaction-diffusion models, this yields, in principle, a complete, albeit effective characterization of the instability space (cf. [128, 130]). In reality, however, pattern-forming mechanisms often operate in spatially heterogeneous environments. In such cases it becomes critical to understand the effects of the imposed spatial heterogeneity on the ability of the mechanism to generate pattern, and on the form of the resulting pattern. Karen et al. [137] investigate the effect of heterogeneity of the medium on pattern formation in more general reaction-diffusion systems. They found that the heterogeneity of the medium can increase both the complexity and range of possible patterns and enhance the robustness of patterns. These effects on Turing instabilities also have been studied in numerous works [177, 102, 41]. An interplay of dynamics of propagating combustion front and the heterogeneity of combustible medium has been addressed previously. Lu et al. studied the pattern formation in reverse filtration combustion in porous media under both adiabatic and non-adiabatic assumptions [100]. Their results show the development

of unstable, fingered patterns of the burned fuel, similar to those observed in the related problem of reverse combustion in a Hele-Shaw cell. More reviews on combustion process in heterogeneous media can be found in [1, 120, 3]. We will study the effect of spatial heterogeneity on dynamic pattern formation in chapter 4.

Rate and the order of chemical reaction

A fundamental consideration when considering combustion is the kinetics that drive the reaction within the combustion front. In principle, a wide variety of kinetic forms may be used in both heterogenous and homogenous models. Two main kinetics have been suggested for these systems in the literature. The first, and most common, is “Arrhenius kinetics” and the second is “Stepwise ignition kinetics”. These kinetics will be discussed and compared in chapter 2. In this work, we settle on and assume that the more physically relevant reaction rate follows stepwise ignition kinetics for solid-gas combustion of metal particles [166, 14, 22].

Effect of transport mechanisms and Lewis number

The Lewis number (the ratio of thermal to mass diffusivity), is a key parameter to characterize the competition of thermal versus mass transfer on combustion fronts that exhibit thermo-diffusive instabilities. Such instabilities have been investigated in experimental and numerical studies [43, 122, 193] and often lead to cellular or fingering patterns at low Lewis number and oscillatory front motion at large Lewis numbers. Cellular interfaces often begin through the linear instability of a few wave modes of the interface at early times. Non-linear interactions between these modes give rise to complex patterns at late

times. Such patterns can involve both overhands and cusps. For example, Denet et al [43] predicted local extinction in cusped patterns for lean hydrogen flames in the limit of low Lewis number, leading to the front morphologies observed in the experiments [122]. Some examples of combustion systems with reaction kinetics and observed thermo-diffusive instabilities within a range of Lewis numbers are presented in Fig. 1–2.

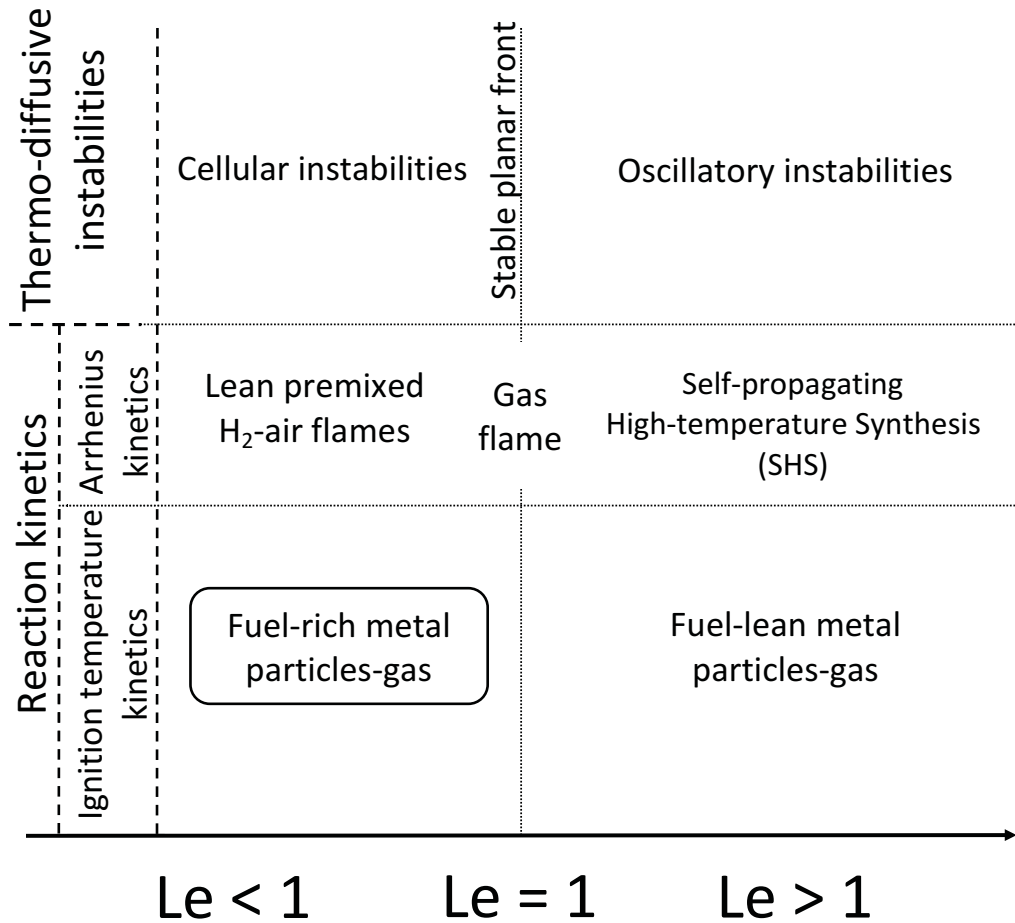


Figure 1–2: Classification of different combustion systems with respect to the reaction kinetics and Lewis number. Thermo-diffusive instabilities generally form “Cells” at low Lewis numbers ($Le < 1$), and “Oscillations” for high Lewis number ($Le > 1$), as has been observed in previous studies [148, 45, 117, 81]. This thesis studies the regime of rich metal particles in gas.

Instabilities of combustion front

Combustion is a popular paradigm for studying complex spatiotemporal dynamics and pattern formation in reaction-diffusion processes [107, 192, 123, 164, 59, 24, 147, 75, 160, 23, 54, 127]. Experiments with premixed flames show that combustion fronts can exhibit cellular [122, 63] or oscillatory patterns such as traveling waves, pulsations, and spinning fronts [164, 59]. These patterns, in the absence of buoyancy, originate in hydrodynamic effects and thermal/mass diffusional instabilities [192, 159, 163]. The former mechanism, as shown by Darrieus and Landau, is based on assumption that the mixture density changes due to gas expansion resulting in density jump across the flame front [37, 91], whereas the latter mechanism accounts for the competition between heat and mass transport phenomena [13, 159]. Flames fronts that develop under these instability mechanisms appear to be wrinkled and develop spatial and temporal patterns. In the case of thermo-diffusive instabilities, when segments of a wrinkled combustion front bulge into an unburnt (fresh) mixture, lateral heat conduction diffuses excess heat away, thereby stabilizing the front. Mass diffusion flux of a limiting reactant towards the bunched area, on the other hand, can promote the propagation of the wrinkle and further destabilize it. This thermo-diffusive instability mechanism is thus dominant in combustion systems where Lewis number Le , the ratio of thermal diffusivity to a mass diffusivity of limiting reactant, is sufficiently small and hydrodynamic effects are negligible [160, 159]. Recent theoretical studies have shown that a similar instability may occur in an isothermal reaction-diffusion front, when the diffusivity of the autocatalyst is sufficiently lower than that of the stoichiometrically deficient reactant. For instance, lateral instabilities in isothermal reaction-diffusion fronts and

thermo-diffusive instabilities in premixed flames share many common features [70, 112]. These instabilities also resemble “Turing structure” in activator-inhibitor systems when the diffusivity of an activator is larger than that of an inhibitor.

Several studies have been conducted to examine combustion front instability due to hydrodynamic effects. The first model in the linear regime of combustion front dynamics was proposed by Darrieus and Landau [37, 91] who considered a flame as a density jump propagating at a constant speed in an incompressible, non-viscous, non-conducting fluid. This assumption is valid for the wavelength of disturbances larger than thermal thickness. A flame thickness is given by $l_{\text{th}} = D_{\text{th}}/V$ where D_{th} and V are thermal diffusivity and normal velocity of flame front, respectively. This model, however failed to predict the correct dynamics and instabilities of flames observed in experiments, specifically for short-wave disturbance. Markstein [111] attempted to resolve this issue by introducing a phenomenological length-scale into the equation, connecting the curvature of the front to its speed. Due to the uncertainty in the phenomenological constant, this model also did not comply with experimental observation. A few years later, in 1966 Istratov and Librovich [76] suggested that the flame has two characteristic lengths, the small one appears because of thermo-diffusive effects while the larger is signature of hydrodynamic effects. These assumptions are implemented the equation of growth rate of instabilities developed by Frankel and Sivashinsky (1982) [55] and Pelce and Clavin (1982) [141], given by

$$\sigma = \Omega_0 V k - \Omega_1 D_{\text{th}} k^2 \quad (1.3)$$

where σ is the instability rate, k is the perturbation wave number, $\Omega_0 = \frac{1}{2}\gamma$, and $\Omega_1 = [\frac{1}{2}\beta(\text{Le}^{-1} - 1) - 1]$, while γ , β , and Le are the thermal expansion coefficient, Zeldovich

and Lewis numbers, respectively. Hydrodynamic effects, due to gas expansion, have been shown to narrow down the range of unstable linear modes of thermo-diffusive instabilities [163]. The viscosity turns out to have a secondary effect on the flame stability and should appear in higher-order expansion of Eq. (1.3). It may, however, be significant when either $\Omega_1 < 0$, meaning that when hydrodynamic flame instability combines with thermo-diffusive instability, or when Ω_1 is both positive and small[163].

Some studies have focused on the thermo-diffusive instabilities and ignore hydrodynamic effects. The main mechanism of cellular structures in premixed flames is shown to be a result of high diffusivity of deficient component in reaction (low Lewis number limit) [96]. Sivashinsky [160, 159] showed that cellular formation can occur purely due to diffusional-thermal instability, and need not be connected with the hydrodynamics of the perturbed flow. Sivashinsky developed a thermo-diffusive model by using constant-density assumptions which implies the density of the gaseous mixture is constant everywhere and ignored the thermal expansion of gas. This model also assumes that If the combustible mixture is motionless at the initial instant, the gas will remain motionless and uniform throughout the process thus underlying flow field can be ignored as well. He developed a thermo-diffusive model, which for a range of small Lewis number ($Le < Le_c$) (Le_c being the critical Lewis number) can explain both linear and nonlinear regime of cellular flames. The model is also capable of predicting the chaotic motion of cells in long-term dynamics which are observed in experimental studies [112, 110].

The combined effects of hydrodynamic and thermo-diffusive mechanisms have been also investigated[44, 4, 158, 32, 114]. Denet et al. in their study of thermo-diffusive instabilities of premixed flames used the thermo-diffusive model ([13]) with the assumption

of negligible gas expansion. They justified this assumption by noting that in most applications, gas density is generally much lower in the burnt gases than in the fresh mixture and thus important hydrodynamical effects, are not included in the thermal-diffusive model. Their calculation found the correction for real gas expansion of flames is very large and its influence on the growth rates is very important. In a similar study, Altantzis et al. [4] showed that the triggering mechanism of instability for large wavenumber (short wavelength) of perturbations on sub-unity Lewis number flames is thermo-diffusive. Their results did show, however, that during the long-time propagation of the flame, the wavenumber of secondary modes (after tip-splitting) lie outside the range of the linearly unstable modes. This could be thus an indication of the coupling effects of the two mechanisms of instability considered in this study. Upon increasing the lateral system size, the nonlinear evolution of the flame was characterized by chaotic cell splitting and merging. Their numerical results, along with [44], could justify that hydrodynamic effects only introduce secondary effects. In this work, we will take this approach and thus ignore hydrodynamic effects to focus our study to thermo-diffusive instabilities.

In addition to the largely theoretical and experimental studies on premixed flames discussed above, there is also evidence of cellular and fingering pattern formation in the absence of convection in non-premixed combustion systems, such as thin solid fuel combustion[193], smoldering [196], and flame propagation over a bed of metal nanoparticles [104].

Despite the different underlying physical mechanisms in the various aforementioned RD systems, they all share several qualitative instability mechanisms in the limit where we

assume only thermo-diffusive instabilities at work. Therefore, our study of pattern formation in combustion examined in his thesis will serve as a paradigm for pattern formation physics in the sub-unity Lewis number regime of numerous different systems. Nevertheless, it should be pointed out that in order to understand more quantitatively the behaviour of more realistic experimental condition, particularly for gaseous combustion, hydrodynamic effects have to be taken into account.

Approaches for self-consistently ignoring hydrodynamic effects

Several approaches have been suggested to self-consistently ignore hydrodynamic effects in RD systems when considering thermo-diffusive instabilities. One is to carry out the analysis within the context of a constant-density model, namely assuming that the density is independent of temperature so that the flow field not affected by the flame may be prescribed a-priori. For instance Bruck et al.[28], in studying diffusion flames in concentric ducts, effectively introduced constant-density approximation which can be systematically obtained as an asymptotic limit when the heat release parameter is small. However, in general, premixed fames, e.g., hydrogen-air and methane-air fames with stoichiometric conditions, exhibit considerably large heat release. Thus hydrodynamic effects caused by thermal expansion plays an important role in the instability of premixed fames [82]. Nevertheless, ignoring hydrodynamics is useful in elucidating some of the complexities associated with thermo-diffusive aspects of the combustion process. The flame shapes and heights predicted by Burke et al. [28], for example, are in remarkably good agreement with experimental results. The stability of a planar premixed flame is another example where the constant-density approximation has been used to filter out hydrodynamic disturbances

and provide explicit results about the role of diffusion on the onset of instabilities in the form of cells and/or oscillations [160]. The author of this paper [160] used the constant density model and treated the flame as an exothermic reaction front supported by molecular transport of the reacting species and heat, which propagate in a motionless medium, if the gas is motionless initially. These results were instrumental later on in constructing a more comprehensive stability theory that includes the previously missing hydrodynamic effects [56, 141, 114, 82].

Another approach for neglecting hydrodynamics in combustion front modelling is suggested by Spalding [169]. He proposed to simplify the governing equations for the flame by introducing a density-weighted coordinate. In this coordinate system, the continuity equation is automatically satisfied, and advection effects induced by thermal expansion of the gas are absent. Once found, the solution in x -space can be transformed into physical coordinates, as described by Margolis[106].

A third approach for neglecting hydrodynamics is the so-called diffusive approximation, in which the gas expansion is assumed to be small, so that the thermal diffusive variables, i.e., temperature T and mass fraction of the limiting reactant C , evolve in an imposed flow field. This approximation is equivalent to the one usually made for scales larger than the flame thickness when one solves for a discontinuity propagating front with a given normal velocity and subject to a turbulent flow field without retroaction. This usually is done by using an eikonal equation describing flame propagation[85] , i.e., by transforming the front propagation problem into a field equation in order to avoid the difficult problem of reconnections occurring on the front[42].

In this work will be using constant density approximation [160]. This assumption can be justified based on the considerably small density of burned gas in the product zone compared to that in fresh mixture. In what follows we review recent studies conducted on thermo-diffusive instabilities of combustion fronts for a range of Lewis numbers.

Thermo-diffusive instabilities: from cells to oscillations

Numerical simulations and experiments on thermo-diffusive instabilities in combustion for small Lewis number have reported a wide range of interface instabilities, ranging from cellular fronts [164, 108, 43] to turbulent fluctuations far in the non-linear regime [24, 147, 75, 112]. In the latter context, Sivashinsky investigated self-turbulizing cells using a non-linear differential equation to model the surface of a flame front in a premixed gaseous fuel [160]. There is also evidence of cellular and fingering instabilities in non-premixed combustion systems [193, 196, 2, 104]. Flame propagation over thin solid fuels first introduced by Ris[40], has gained significant attention recently. Zhang et al. [193] studied the effect of Lewis number experimentally on flame spreading over thin film solid fuel by including Lewis number effect into Ris's model [40]. They observed the cellular structure for range of Lewis numbers < 1 for systems of $\text{S}_2 - \text{SF}_6$ and $\text{O}_2 - \text{CO}_2$. The cells observed exhibit constant splitting and merging, resembling those pattern observed in premixed flame where the thermo-diffusive instabilities for low Lewis numbers results in cellular flame fronts [31]. The resemblance attributed to the finite Damköhler number (the ratio of a characteristic chemical reaction rate to a characteristic convective or diffusive transport rate) effects lead to leakage of reactants through the flame front [98] and

thus regions will exist where fuel and oxidant are mixed but not reacted. These premixed regions could then exhibit cellular structures in a manner similar to premixed flames [31].

Another interesting thermo-diffusive pattern formed in solid fuel oxidation was reported by Zik et al. They observed a fingering instability of solid fuel when it is forced to burn against a horizontal oxidizing wind in their experiment on paper [196]. The onset of fingering instability appears in the absence of natural convection (when the Rayleigh number for convection is below criticality) [195, 196]. These patterns, which have been explained in the context of thermo-diffusive instabilities, appeared in a well defined regime of the Rayleigh and Péclet numbers below the threshold of vertical convection when molecular diffusion in the horizontal plane is a prevailing factor. In their experiments, vertical (i.e. natural) convection, is introduced in order to mimic microgravity. They distinguished two length-scales in their experiments, finger width, which is determined by the ability of the front to release heat, and inter-finger spacing controlled by the availability of oxygen. This happens due to the limited amount of oxygen present in the space between the paper (solid fuel) and the top of the cell. Conti et al [33], in their numerical investigation of instabilities of front instabilities in slow combustion, observed fingering instabilities resembling dendritic structure . The authors draw connections between this phenomena and those observed in binary alloy dendritic growth [92]. Recently, Malchi et al. [104] conducted experimental studies on flame propagation over a bed of nano-aluminum particles, burning with a counter-flowing oxidizer. They observed fingering instabilities where the diffusing of oxygen is the dominant mechanism of destabilization.

At high Lewis numbers, oscillatory and spin modes due to thermo-diffusive instabilities have also been reported [138, 139]. Other studies observed a transition from a

uniform solution to chaotic pulsations via periodic doubling[23, 54]. In the limit of high Lewis number, if thermal expansion of gases is not negligible, hydrodynamic effects due to underlying flow fields are may be considerable as well [32, 141, 160]. Auto-oscillatory instabilities, including spinning and pulsation are reported in gas-less solid fuel combustion [103, 119]. A more complete review of the different types of instabilities reported in these reactive systems can be found in previous studies [127].

Methods used in this thesis to study dynamic pattern formation of the combustion front in linear regime

A key tool used in this thesis to obtain important information about patterning in diffusion-limited RD systems is the linear response of the interface. Most systems exhibiting cellular patterns have a characteristic linear regime which is characterized by the growth rates of different modes of perturbation [126]. This is analogous to the way the onset of cellular or dendritic instabilities are characterized in directional solidification phenomena. There, the scale and morphology of crystalline patterns is calculated using various system properties like number of fields governing a front, the gradient energy of the fields at the interface and front's velocity. The emerging length-scales of such patterns are characterized using linear stability analysis. Some of the classic analytical techniques used in solidification analysis are summarized in [92].

In this work, we explore the characteristics of cellular instabilities in combustion fronts for the case of both continuum and discrete random distribution of reactants (metal particles). We will perform this analysis on a specific class of RD modes adapted for this work, but the the approach is general for any system of free boundary problems. The

first step is to find the steady-state (uniform) solution of a front supported by the set of energy and mass balance equations comprising the RD model and the appropriate boundary conditions. The steady state is then perturbed by a small amplitude sinusoidal perturbation in time and space of the form of $A_o \exp(-\omega t + i k x)$ where A_o , k , and ω are amplitude, wave number, and growth rate of the perturbation. Substituting the perturbed solution into the RD equations and keeping only term of linear order, we can solve for a relation for ω as a function of k and all model parameters (in our case, ignition temperature θ_{ign} and Lewis number Le). This relation is called a linear dispersion relation. Different type of instability in linear regime of dynamics based on the value of ω is expected. For combustion front instabilities in the form of cells, real ω ; for oscillatory solutions, pure imaginary ω ; and for wave propagation, complex ω is expected. In this study we applied numerical methods to find the linear growth rate of perturbation modes. Our numerical dispersion relation is then verified with the analytical prediction of [22]. The numerical algorithm to find dispersion relation can be found in (https://bitbucket.org/hosseainphy/phd_files).

Numerical Methods for simulating general combustion dynamics

Exploring morphological patterning in combustion fronts, from the linear and especially in the long time non-linear regime, requires large simulation domains in order to minimize the role of finite size effect and boundary conditions. This is an extremely challenging task with traditional uniform-mesh numerical techniques, and several methods have been proposed for tackling it [19, 44]. Here, we use a new dynamic adaptive mesh refinement

(AMR) algorithm based on a C++ finite difference scheme that is parallelized with both OpenMP (shared memory) and MPI (distributed memory) parallelization. Our AMR algorithm is similar in methodology to the original AMR code developed by Provatas et al. [146, 10] to study solidification microstructures. The use of AMR dramatically decreases CPU times and memory usage over uniform or fixed grid techniques as it scales both these metrics with the length (2D) or area (3D) of a free-boundary problem. The AMR approach employed in this thesis will allow us to model systems larger than any previously studied numerically, not only with our model but with any other to our knowledge. Its details will not be presented here as it would significantly increase the page count of this thesis.

Summary

This thesis will study of thermo-diffusive stability of gas-solid combustion fronts, and the resulting pattern formation of these systems for experimentally relevant system sizes and parameters. To our knowledge this is the first work to use a novel adaptive mesh refinement algorithm applied to the new class of solid-gas combustion models adapted into one formalism for this work. It will examine the transition from cellular to dendritic morphologies of flame fronts in both continuous and random reactant distributions, characterizing these as functions of ignition temperature kinetics and Lewis number.

The remainder of this thesis is organized as follows. In Chapter 2, we introduce a pair of reaction-diffusion equations that reduce to various previous models for solid-gas combustion. We focus on the properties of this general system of equations in a special limit recently proposed by Brailovsky et al. [22] due to its quantitative description of oxidation of solid particulate fuels, which is of particular interest in materials science. Specifically, the model assumes ignition temperature kinetics to describe the combustion

of solid metal fuel by employing a step-wise activation above an ignition temperature, T_{ign} . While activation is purely thermal, it also couples to the oxidizer concentration, making the reaction mass-transport-limited [166, 61, 180].

In Chapter 3, we examine the dynamics of combustion fronts in the parameter space spanned by the order of reaction (n), the Lewis number (Le), and rate of reaction. Specifically, we focus on the role of oxidizer and thermal transport in the development of fronts with cellular and dendritic morphologies in solid-gas combustion. Here we examine the limit of continuum fuel sources. The linear growth rate and wave-length selection of cellular flame fronts are examined numerically, validating the recent analytical predictions of Brailovsky et al. [22]. In the non-linear regime, we characterize the growth of combustion morphologies that vary from cells to *seaweed* dendrites analogous to those observed in directional solidification [5, 6]. This is seen to happen for low Le, a regime separating cellular/dendritic patterns from oscillatory modes prevalent at high Le. Length-scale selection of these complex front morphologies fingers is analyzed qualitatively in the context of the linearly unstable k modes available to the system at early times. In the second part of this chapter we present a non-adiabatic form of reaction-diffusion equations by using linear (Newtonian) heat transfer law. We then further investigate the effect of heat dissipation on linear regime of combustions using the same numerical and analytical methods mentioned in the first part for adiabatic flames.

In Chapter 4 we study cellular spacing and dynamics of combustion front in systems with fuel particles that follow a uniform random spatial distribution. We first examine the effect of stochasticity on early-time dynamics of the propagating front by applying numerical linear stability analysis methods analogous to those developed in chapter 3. These

results will be compared with corresponding results for continuum combustion fronts studied in Chapter 3. We show that it is possible to map the effect of random media onto the regime corresponding to low Lewis number values in the continuum limit. In the second section of Chapter 4, the effect of randomness on the non-linear regime of the combustion front dynamics will be examined and compared, qualitatively, with the limit of decreasing Lewis numbers in the continuum situation. The last part of this chapter probes the late-time dynamics of front in non-uniform random distributions and discusses the similarities and differences between cellular patterns in the random medium with non-uniform and uniform random particle distributions.

CHAPTER 2

Overview of modelling combustion systems: continuum and discrete limit

In this chapter, we derive a model suitable for metal fuel combustion systems. For this purpose, we generalize the recent model of Brailovsky et al. [22] to include distinct process kinetics and reactant heterogeneity. This leads to a generalized mathematical model that is practical for combustion fronts in heterogeneous media, which includes flames in a suspension or in a packing of metal particles. The generalized model is derived analytically for combustion of a distribution of particles and validated with other established models in the limit of infinite Lewis number for zero-order and first-order chemical kinetics, in both continuum (homogenous) and discrete (heterogenous) media. The derived model then will be used to study cellular instabilities of propagating fronts in homogenous media (chapter 3), and in heterogeneous media (chapter 4).

2.1 Review of reaction rate kinetics

Physico-chemical-chemical theory, which in principle, considers chemical kinetics and heat/mass transfer simultaneously, was formulated by Lewis and von Elbe [95], Zeldovich and Frank-Kamenetsky [189], Semenov [155], and Hirschfelder et al. [68].

The earliest theories specified for combustion front, suggested so-called ignition temperature kinetics, assuming that there is a fixed ignition temperature below which no reaction occurs [105, 134, 79, 36]. For example Daniell [36] assumed that the reaction rate,

below a definite temperature T_i , is identically zero. According to his assumption, in samples with low enough temperature $T_0 < T_i$, the reaction rate is zero $W(T_0) = 0$, and $W(T)$ is constant inside the reaction zone for $T_i < T < T_b$, where T_b is the adiabatic temperature. The adiabatic temperature T_b , is the temperature that results from complete combustion of fuel in the absence of heat loss.

In the formulation of the classical theory of combustion Zeldovich and Frank-Kamenetsky [189] proposed another kinetic model which has been commonly used in combustion literature. This chemical kinetics relates the rate of reaction at the front to temperature by using Arrhenius function $W(T) \sim \exp(-E/RT)$, where E , and R are activation energy of a reaction and universal constant of gases, respectively. The typical form of ignition-temperature kinetics (solid green line) and Arrhenius kinetics (solid gray line) are shown in Fig. 1–1.

Arrhenius kinetics are mainly suited for premixed gaseous flames [189]. Such reaction kinetics are also suggested for flames in a suspension of particles, in which the reaction rate modified for a combustible mixture with a single-step, first order heterogeneous surface reaction whose rate is controlled by Arrhenius kinetics. The use of an Arrhenius reaction rate assumes that combustion of particles occurs under thermal equilibrium between particle and the surrounding oxidizer gas. Arrhenius-based models predict that the reaction rate is different from zero at any non-zero temperature. Consequently, a fresh mixture in the far end of a long reactor will eventually react even when quite far from the combustion front [191]. They are referred to as “kinetic-limited” models and are a good approximation for combustion of small particles ($r_p \sim 1\mu m$).

Even though the classical theory of combustion kinetics [189] might be compatible with physico-chemical mechanism and assumptions in gaseous mixtures, it has been shown recently in experiments of oxidation reactions of metal powder [166, 22] that large fuel particles greater than a few micrometers do not react (oxidize) effectively below some prescribed temperature (T_{ign}), even after a long exposure time [105, 134, 79, 36]. In this regime of combustion, the reaction taking place on the surface of the particle has a very fast rate due to the higher temperature at the particle surface compared to its surrounding gas; this aspect of the surface reaction is controlled by temperature-activated Arrhenius kinetics. However, during this surface reaction, the rate of mass transfer of oxidizer from the bulk of the oxidizer towards particle's surface is smaller than the reaction rate at the surface, and thus controls the overall rate of particle combustion. The regime in which the surface reaction depends on the migration rate of oxidizer concentration towards the particle surface is called “diffusion-limited” regime and is a good approximation for intermediate to large fuel particles ($r_p > 7\mu\text{m}$) [166]. This limit essentially modifies the surface reaction to be governed by ignition temperature kinetics. It is noteworthy that when the particle’s radius shrinks as a result of oxidation, the rate of oxidizer mass transfer becomes comparable or larger than reaction rate and the reaction goes over to the kinetic-limited regime.

In what follows we study models using both Arrhenius kinetics and ignition kinetics for flames in a suspension of heterogenous and continuum particle distributions.

2.1.1 Model derivation

Typical one dimensional steady-state profiles of combustion front temperature T , oxidizer concentration C_{ox} , and reaction rate as a function of local temperature and concentration W , for a single-step irreversible reaction, are shown in Fig. 1–1. The front is traveling toward the positive direction of spatial coordinate $+x$ which is fixed with respect to the front. We consider the reaction rate driving the combustion reaction as either a step-wise function or an Arrhenius function for the general derivation. A reaction front propagates for the following reasons. Far from the interface, with the initial temperature T_o , the reactant is in a non-equilibrium thermodynamic state, but the chemical reactions occurring are extremely slow (the characteristic reaction time when T_o is around room temperature is very large). Within the combustion front, however, the temperature increases significantly and the chemical conversion is very rapid, typically taking just milliseconds to complete. Heat generated in this intense chemical conversion zone is conducted partially upstream to cooler layers, heating them and increasing their reaction rate. As a result, the propagation of an exothermic reaction front (or “wave”) occurs.

The conduction of temperature through the system is governed by the energy equation, written in lab coordinates as

$$\rho c_p \frac{\partial T}{\partial t} = \nabla \cdot (\kappa \nabla T) + Q W, \quad (2.1)$$

where ρ , c_p , κ , are density, specific heat and thermal conductivity of a mixture, T is local temperature field, Q is heat released per unit mass of reactant, and

$$W = f(T) C \quad (2.2)$$

is rate of chemical reaction, where here C is the local solid reactant concentration. Dependency of reaction rate on temperature enters through $f(T)$ term. The evolution of solid reactant concentration C , is given by mass conservation, leading to the following equation,

$$\frac{\partial C}{\partial t} = -W. \quad (2.3)$$

In writing Eq. (2.3) we assumed that the solid phase is immobile and thus its diffusion can be neglected. Equations. (2.1-2.3) describe the oxidation reaction of metal particles, where solid metal fuel reacts with gaseous oxidant. Going forward, it will be more useful to express the combustion problem in terms of the temperature diffusion and *oxidizer concentration* diffusion. This is given by ¹

$$\begin{cases} \rho c_p \frac{\partial T(\vec{x})}{\partial t} = \kappa \nabla^2 T(\vec{x}) + Q W \\ \frac{\partial C_{\text{ox}}(\vec{x})}{\partial t} = D_{\text{ox}} \nabla^2 C_{\text{ox}}(\vec{x}) - \frac{W}{\gamma}, \end{cases} \quad (2.4)$$

where C_{ox} , D_{ox} , κ , γ , are local oxidizer concentration, mass diffusivity of oxidant, heat conductivity of the medium (mixture of gas and solid phase), and stoichiometric ratio of chemical reaction (oxidation or solid reactant), respectively.

In deriving our final combustion equations, several assumptions have been made. The reaction is assumed to be a simple one-step exothermic reaction. Molecular weight, and specific heat capacity c_p , are constant, and we will hereafter assume that thermal conductivity κ and the diffusivity of oxidizer D_{ox} are temperature-independent. Furthermore,

¹ This transformation from $C \rightarrow C_{\text{ox}}$ is given in the appendix A.

hydrodynamic effects due to thermal gas expansion assumed to be negligible [159]. The rate of reaction W in Eq. (2.2) can be written in the following form,

$$W = \gamma f(T) C_{\text{ox}}^n, \quad (2.5)$$

where n is referred to as the *order* of the reaction ($n = 0, 1$). The reaction rate W contains the specific type of rate function (Arrhenius or stepwise) and heterogeneity of the reacting medium (continuum or discrete set of fuel particles).

2.1.2 Specializing the model for kinetic-limited reaction rate

In this section we specialize the above model for later analysis in the case of first-order reaction (denoted by $n = 1$), with non-zero oxidizer diffusivity (Le finite) and Arrhenius rate form. This specialization will also provide scaling variables to use with the model equations in general. Specialization of the equations for the limit of Lewis number ($\text{Le} \rightarrow \infty$), and zero-order reaction ($n = 0$), can be obtained in an analogous way. The source term in Eqs. (2.4) is given as an Arrhenius source term $W = C_{\text{ox}} k_o \exp(-E_a/RT)$, where k_o is the pre-exponential factor, E_a is the activation energy of reaction and, R is the universal gas constant. This function represents the strong temperature functionality of reaction rate in exothermic reaction in flames.

The steady-state version of Eqs. (2.4) in a frame of reference moving with normal velocity u relative to the lab frame, thus, can be written in the following form:

$$\begin{cases} -\alpha \frac{d^2T}{dx^2} + u \frac{dT}{dx} = \frac{Q}{\rho c_p} W \\ -D_{\text{ox}} \frac{d^2C_{\text{ox}}}{dx^2} + u \frac{dC_{\text{ox}}}{dx} = -\frac{W}{\gamma}, \end{cases} \quad (2.6)$$

where $\alpha = \kappa/\rho c_p$ is the thermal diffusivity of the medium. These equations can be written in dimension-less form using the following rescalings

$$\theta = \frac{\rho c_p T}{QC_{\text{ox}}^0}, \quad \phi_{\text{ox}} = \frac{C_{\text{ox}}}{C_{\text{ox}}^0}, \quad \bar{x} = \frac{x}{\alpha/u}, \quad \bar{t} = \frac{t}{\alpha/u^2}, \quad (2.7)$$

where C_{ox}^0 is defined as the oxidizer concentration in the bulk (far from the particle), and u is a characteristic speed of the steady state front. Substituting this change of variables and the definition of W into Eq. (2.6) gives

$$\begin{cases} \frac{d^2\theta}{d\bar{x}^2} - \frac{d\theta}{d\bar{x}} + \frac{\phi}{t_R} \exp\left(\frac{-\theta_a}{\theta}\right) = 0 \\ \frac{d^2\phi_{\text{ox}}}{d\bar{x}^2} - \frac{d\phi_{\text{ox}}}{d\bar{x}} - \frac{\phi_{\text{ox}}}{t_R \gamma} \exp\left(\frac{-\theta_a}{\theta}\right) = 0, \end{cases} \quad (2.8)$$

where $t_R = u^2/\alpha k_o$ is the dimension-less combustion time. These equations can be solved in the preheat and combustion zones, and their solutions matched using the following interface boundary conditions,

$$\begin{aligned} [\theta] &= 0 & [\phi_{\text{ox}}] &= 0 \\ \left[\frac{d\theta}{d\bar{x}} \right] &= 0 & \left[\frac{d\phi_{\text{ox}}}{d\bar{x}} \right] &= 0, \end{aligned} \quad (2.9)$$

where $[\cdot]$ denotes a jump across the interface, and far-field values,

$$\begin{aligned}\theta(+\infty) &= \theta_b & \theta(-\infty) &= \theta_0 \\ \phi_{\text{ox}}(+\infty) &= 1 & \phi_{\text{ox}}(-\infty) &= 0,\end{aligned}\tag{2.10}$$

it is straightforward for one to find the steady-state solutions and normal velocity of the combustion front.

2.1.3 Specializing the model for diffusion-limited kinetics

Here we will specialize the model for diffusion-limited combustion rate. We begin first by developing the form of the reaction rate term W specifically for combustion of suspension of metal particles, which is the main topic of this work. We then later use it in the model equations Eq. (2.4) derived above.

2.1.3.1 General expression of a single particle burning rate

The reaction rate of one particle in a hot oxidizer gas (oxidation) is controlled by both the rate of surface reaction (Arrhenius kinetics) and the rate of oxidizer mass transfer towards the surface of a particle. We define the degree of conversion of a particle by

$$\eta = \frac{m_p(t=0) - m_p(t)}{m_p(t=0)}\tag{2.11}$$

where m_p is the mass of the particle. The conversion rate of the particle, assuming the ignition criteria is already satisfied in temperature, becomes

$$\frac{d\eta}{dt} = \frac{L \gamma K_{\text{eff}} C_{\text{ox}}^o}{\rho_L r_o} \left(\frac{r_p(t)}{r_o} \right)^{L-2}\tag{2.12}$$

where r_o is the initial fuel particle radius, $K_{\text{eff}} = K(T_s)\beta/[\beta + K(T_s)]$, where $K(T_s)$ is the Arrhenius reaction rate on the surface of the particle with temperature T_s , and is given by $k_o \exp(-E_a/RT_s)$ [m/s], and β is the mass transfer coefficient [m/s]. Here C_{ox}^o is an oxidizer concentration in bulk [kg/m³]. L , γ , r_p , ρ_L , are dimension of the space, the chemical stoichiometric coefficient for fuel oxidation reaction, radius, and density of the solid fuel, respectively. The derivation of Eq. (2.12) is presented in Appendix A. Equation (2.12) can be interpreted as the conversion rate from the reaction of one particle with hot oxidizer gas, and thermal activation part, represented by $H(T(\vec{x}, t) - T_{\text{ign}})$, is not written in this equation.

Combustion of one particle is an idealistic assumption and as is shown in other studies [167, 60], the “cloud” effect can alter the particle’s conversion rate and its combustion time. In the following section we will calculate the conversion rate of a particle surrounded by a cloud of particles for different limits of mass diffusion (or equivalently Lewis number) and reaction orders $n = 0, 1$.

2.1.3.2 Combustion of a particle surrounded by a cloud of particles

Before proceeding, it is appropriate at this juncture, to define formally what the reaction order n implies in terms of oxidation reaction of metal particles. The chemical process of metal fuel oxidation depends on the available concentration of both fuel (metal particles) and oxidizer. If the initial fuel concentration, $B[\text{Kg}/\text{m}^3]$ is equal to the stoichiometric value, B_{st} , then the amount of oxidizer required to completely oxidize the

fuel according to the chemical reaction of oxidation is $C_{\text{ox}}^{\text{o}} = B/\gamma$, where γ is the chemical stoichiometric ratio. The order of reaction is determined based on an initial available concentration of oxidizer. Two main reaction orders that we discuss here are zero and first-order kinetics. In zero order kinetics ($n = 0$), it is assumed that the amount of oxidizer is either equal or above its stoichiometric value, whereas for first order ($n = 1$) the oxidizer concentration is below it. When the amount of available oxidizer concentration is above (below) its stoichiometric value, the combustible mixture is called a fuel-lean (fuel-rich) mixture.

We next adapt the single particle combustion rate formula in Eq. (2.12) for a two-dimensional system and for the case when it is surrounded by a cloud of particles. We consider two reaction orders mentioned above in two limits of Lewis number, finite and infinite. The results are summarized below, and the detailed derivations of the formulae below can be found in appendix A.

- **The limit $n = 0$; $\text{Le} \rightarrow \infty$**

In this case, because oxidizer is in excess and does not diffuse, particles do not depend on local oxidizer's concentration, and can effectively burn independently. Therefore, the reaction rate of these particles, on average, is constant and is approximated by

$$\frac{d\eta}{dt} = \frac{1}{t_R^*} H(t_R^* - (t - t_{\text{ign}})) \quad (2.13)$$

where t_R^* is the combustion time, and t_{ign} is the time at which any point on the surface of particle first reaches the ignites temperature. The combustion time t_R^* is given in the appendix A in A.1, and related to the pre-factor in Eq. (2.12). The Heaviside function $H(x)$

in Eq. (2.13), reflects the constant combustion rate during oxidation process of a particle in the cloud.

- **The limit $n = 0$; Le finite**

In this situation, although the amount of oxidizer in the whole is in excess, it might be rate-limiting locally. The local oxidizer, thus should appear in the reaction rate. The conversion rate of particle, with dimension-less local oxidizer $\phi_{ox}(\vec{x}, t)$, is thus given by

$$\frac{d\eta}{dt} = \frac{1}{t_R^*} H(\phi_{ox}(\vec{x}, t)). \quad (2.14)$$

The Heaviside function in Eq. (2.14) indicates that the particle is active as long as there is enough local oxidizer, assuming the ignition criteria is already satisfied in temperature. Equation (2.14) becomes exactly equal to Eq. (2.13) for $n = 0$ and $Le \rightarrow \infty$.

- **The limit $n = 1$; Le $\rightarrow \infty$**

In first-order kinetics, in general, the rate of particle combustion is slaved to local available oxidizer, even in the absence of mass diffusion. The conversion rate of particle in this regime with dimension-less local oxidizer $\phi_{ox}(\vec{x}, t)$ reads,

$$\frac{d\eta}{dt} = \frac{\phi_{ox}(\vec{x}, t)}{t_R^*}, \quad (2.15)$$

which means the conversion rate of the single particle in cloud of particles with first-order reaction and zero mass diffusivity, is a function of available local oxidizer $\phi_{ox}(\vec{x}, t)$ at the surface.

- **The limit** $n = 1$; Le finite

In this case, insufficient oxidizer in the bulk as well as mass diffusion, lead to the strong dependence of particle reaction rate to the local available oxidizer. The conversion rate of a particle here is similar to previous case of ($n = 1$; $\text{Le} \rightarrow \infty$), and reduces to,

$$\frac{d\eta}{dt} = \frac{\phi_{\text{ox}}(\vec{x}, t)}{t_{\text{R}}^*}. \quad (2.16)$$

It is noted that although the conversion rates of a particle in both limits of mass diffusivity in the case $n = 1$ have the same form, available oxidizer in the vicinity of particle in the presence of mass diffusion in Eq. (2.16) is smaller than the corresponding value in zero mass diffusion condition in Eq. (2.15) (see appendix A).

2.1.4 Master model for continuum and discrete solid fuel distributions

In this section we return to specializing the equations of temperature and oxidizer concentration in Eqs. (2.4) for the case of *localized* particles (reaction centres) by using conversion rates for a particle that we reviewed above (and derived in appendix A). We then perform coarse-graining to these equations to find corresponding equations for a continuous medium (called the continuum regime). The results are summarized here. We show details of the derivation for first-order case ($n = 1$) in appendix B. Derivation for zero-order case ($n = 0$) is analogous, and results for this case will thus only be stated where appropriate.

As a reminder, we model combustion by a simple one-step exothermic reaction assuming constant molecular weight, specific heat capacity c_p and a temperature-independent

thermal conductivity κ and oxidizer mass diffusivity D_{ox} . Following Sivashinsky, we neglect hydrodynamic effects and assume the density of the mixture ρ is constant in time and uniform in space [163]. Moreover, the reaction rate follows stepwise ignition temperature kinetics, a physically accurate approximation for solid-gas combustion of metal particles [166, 14, 22]. We assume that oxidizer transport is diffusive and ignore the transport of solid fuel as it is much slower than that of the oxidizer.

An effective medium version of Eqs. (2.4) is obtained by coarse graining over distances that are large compared to the sizes of the heterogeneity, yielding

$$\left\{ \begin{array}{l} \frac{\partial \langle T(\vec{x}) \rangle}{\partial t} = \alpha^e \langle \nabla^2 T(\vec{x}) \rangle + \frac{Q}{\rho c_p} W^e \\ \frac{\partial \langle C_{\text{ox}}(\vec{x}) \rangle}{\partial t} = D_{\text{ox}} \langle \nabla^2 C_{\text{ox}}(\vec{x}) \rangle - \frac{1}{\gamma} W^e, \end{array} \right. \quad (2.17)$$

where α^e and W^e are effective thermal diffusivity, effective reaction rate. The effective thermal diffusivity of a random medium, where metal fuel particles, assumed as 2D impenetrable disks with thermal conductivity κ_s , occupy fraction area Φ_s of the gaseous phase with thermal conductivity κ_g , can be written as follow [30]

$$\frac{\alpha^e}{\alpha_g} = f(\Phi_s) = 1 + 2\Phi_s + 2\Phi_s^2, \quad (2.18)$$

where $\alpha^e = \kappa^e / \rho c_p$ and $\alpha_g = \kappa^g / \rho c_p$, denotes the effective thermal diffusivity of the medium (mixture of solid and gaseous phases) and thermal diffusivity of the gaseous phase, respectively. In deriving Eq. (2.18) the conductivity of solid inclusions is assumed to be much larger than that of the gaseous phase $\kappa_s \gg \kappa_g$. In deriving this set of equations, we assume that oxidizer mass diffusivity D_{ox} does not change significantly in the presence

of particles and, thus can be used for the effective medium. The Lewis number, defined as the ratio of the thermal diffusivity to the molecular diffusivity, in the effective medium by using Eq. (2.18) can be obtained as,

$$Le^e = \frac{\alpha^e}{D_{ox}} = f(\Phi_s) \frac{\alpha_g}{D_{ox}}. \quad (2.19)$$

By setting Φ_s to unity, the effective Lewis number in its continuum limit gives $Le^e(\Phi_s = 1)$, which is hereafter denoted by Le .

In a multi-particle system the reaction rate term W is given by (see appendix A),

$$W = \gamma C_{ox}^o \sum_i \frac{d\eta_i}{dt} H(T - T_{ign}) g(|\vec{x} - \vec{x}_i|, r_p), \quad (2.20)$$

where $d\eta_i/dt$, with both zero and first-order reaction kinetics and for different limits of mass diffusivity, is given by Eqs. (2.13-2.16), and its limit for the case of first-order kinetics is specified by Eq. (2.16). Here, i indexes the particle positions in the system. The Heaviside step function “freezes out” oxidation below the ignition temperature (T_{ign}) for consistency with observed oxidation kinetics as discussed previously for metal combustion. The function $g(|\vec{x} - \vec{x}_i|, r_p)$ is a normalized function with the properties of $g(|\vec{x} - \vec{x}_i| > r_p, r_p) = 0$ and $\int g(\vec{x} - \vec{x}_i, r_p) d\vec{x}$ over particle’s volume is unity, where \vec{x}_i and r_p represent centre and radius of the particle i , respectively. This function is introduced to specify the spatial extent of a particle (i.e. r_p). In the limit where inter-particle spacing is much larger than the particle size $l_p \gg r_p$, particles can be represented by point-like sources localized at random lattice positions and function $g(|\vec{x} - \vec{x}_i|, r_p)$ is replaced by the

delta function $\delta(\vec{x} - \vec{x}_i)$. In the continuum limit studied below, the influence of heterogeneities denoted by $g(|\vec{x} - \vec{x}_i|, r_p)$, are averaged out over a coarse-grained volume in the homogenization process.

Applying the homogenization processes to Eq. (2.20) gives the effective reaction rate in Eqs. (2.17) as

$$W^e = \Phi_s B_{st} \frac{d\eta}{dt} H(T - T_{ign}), \quad (2.21)$$

where $B_{st} = B/\Phi_s$ is called the stoichiometric value of solid fuel concentration, and Φ_s is the local area fraction (volume fraction in 3D) of solid metal particles within a coarse-grained cell. In the continuum limit we set Φ_s to 1 and thus $B = B_{st}$. The effective source term W^e , indicates that the combustion rate of particles within a coarse-grained volume (or local heat generation) is adjusted based on the initial concentration of solid. In Eq. (2.21), $d\eta/dt$ refers to the appropriate effective single-particle reaction rate described in the previous sub-section. The Heaviside function appears explicitly to reflect the ignition temperature assumption.

The coarse graining approach we used here is consistent experimentally. For instance Malchi et al. [104] in their work on the effect of Aluminium particle size on combustion front instabilities, show that the flame exhibits some characteristics of continuum regime flames which probably is due to small size of particles, ranging from 50 nm to 120 nm in their experiments [104].

The effective parameters for thermal diffusivity and reaction rate in the continuum-limit are derived by setting area fraction Φ_s in Eqs. (2.18 , 2.21) to unity. By substituting Eq. (2.16) (for the case $n = 1; Le$) into the continuum limit of Eq. (2.21) and performing

straightforward algebra, one can re-cast the heat and mass balance equations in Eq. (2.17) for the continuum-limit combustion in the following dimensionless form (see appendix B),

$$\begin{cases} \frac{\partial \theta}{\partial t} = \nabla^2 \theta + W \\ \frac{\partial \phi_{\text{ox}}}{\partial t} = \frac{1}{\text{Le}} \nabla^2 \phi_{\text{ox}} - W, \end{cases} \quad (2.22)$$

where $\theta(\vec{x}, t) = (T(\vec{x}, t) - T_o)/(T_{\text{ad}} - T_o)$ is the reduced temperature field while T_o and T_{ad} represent the far-field and adiabatic temperature values, respectively. The reduced ignition temperature is $\theta_{\text{ign}} = (T_{\text{ign}} - T_o)/(T_{\text{ad}} - T_o)$, where T_{ign} is the prescribed ignition temperature which determines the reaction of the fuel. Here, we define $\phi_{\text{ox}}(\vec{x}, t)$, a dimension-less local oxidizer concentration. The Lewis number Le is defined as the ratio of the thermal diffusivity to the molecular diffusivity of oxidizer α/D_{ox} . The source term W in Eqs. (2.22) can be generalized for both orders of kinetics ($n = 0, 1$) by,

$$W = \begin{cases} A \phi_{\text{ox}} H(\theta - \theta_{\text{ign}}) & \text{for } n = 1 \\ A H(\theta - \theta_{\text{ign}}) H(\phi_{\text{ox}}) & \text{for } n = 0, \end{cases} \quad (2.23)$$

where A is the strength of the source term W and is given by $\alpha/(u^2 t_R^*)$, where u is the characteristic steady state velocity of a planar front (see appendix B). In appendix B only the steps for $n = 1$ were discussed. However, the steps for $n = 0$ are analogous.

We can express the continuum combustion model in Eq. (2.22) in a unified way by re-writing the source term in Eq (2.23) as

$$W_n = A \phi_{\text{ox}}^{(n)} [H(\theta(x, t) - \theta_{\text{ign}}) H^{(1-n)}(\phi_{\text{ox}}(x, t))], \quad n = 0, 1 \quad (2.24)$$

Equations (2.22) together with (2.24) are hereafter referred to as the *continuum master model*, the parameters of which are denoted by the notation $\text{MM}(n; \text{Le}; \theta_{\text{ign}})$, which represent the reaction kinetics order n , the Lewis number Le , and the ignition temperature θ_{ign} , respectively. In our simulations of this model, length and time coordinates of the model are scaled by the characteristic length ($\delta_c = \alpha/u$) and characteristic time ($\tau = \alpha/u^2$) where u is the characteristic velocity of planar flame front (see appendix B).

In the limit of discrete fuel particles, ignition only occurs at a location within a fuel particle location. The *master model equations* can be specialized to the case of discrete point-like reactants by using Eq. (2.20) to write W_n as

$$W_n = \sum_i A \phi_{\text{ox}}^{(n)} \left[H(\theta(\vec{x}, t) - \theta_{\text{ign}}) H^{(1-n)}(\phi_{\text{ox}}(\vec{x}, t)) g(|\vec{x} - \vec{x}_i|, r_p) \right], \quad n = 0, 1 \quad (2.25)$$

where here A is defined as $l_p^2/(t_R^* \alpha)$, l_p being an average inter-particle spacing, and the function $g(|\vec{x} - \vec{x}_i|, r_p)$, as is stated before, specifies the spatial extent of a particle i with radius r_p . The sum is over all particles, each of which satisfies the ignition condition. The derivation of Eqs. (2.22) and (2.25) for combustion of metal particles in discrete limit, is presented in appendix A.

In study of combustion fronts, the heterogeneity of the medium and its effects, depending on the ratio of the scale of heterogeneity to the characteristic length of the flame front, can be either considered or precluded. The source term W in Eq. (2.22) depends on whether we consider a discrete set of fuel particles (discrete limit) or a continuum of fuel (continuum limit). In the discrete limit, ignition only occurs at a location of a fuel particle, while in the continuum limit, although still localized, ignition can potentially occur anywhere.

The model defined by Eq. (2.22) with Eq. (2.24) are the model proposed by Brailovsky et al. (i.e. $\theta \geq \theta_{\text{ign}}$ and $\phi_{\text{ox}} > 0$) and its stability was examined analytically. New pattern formation physics emergent from these equations will be studied in this thesis in chapter 3 in the limit of a continuum fuel source. In order to compare our results under adiabatic conditions to the ones with heat dissipation, chapter 3 will also introduce into the continuum master model equation a new linear heat dissipation term. The model defined by Eq. (2.22) and Eq. (2.25) is unique to this thesis and be used to study pattern formation in random discrete media in chapter 4. To study thermo-diffusive effects in continuum regime in chapter 3, we assume the thermal length of the front (δ_c) is much larger than inter-particle spacing l_p and ignore the discreteness of a medium. The reverse is true in randomly distributed heterogeneous media studied in chapter 4.

To obtain an estimate of typical parameters for this model, we use experimental data from the combustion of rich-fuel Aluminium duct clouds, which give the thermal diffusivity as $\alpha \sim 2 \times 10^{-5} [\text{m}^2/\text{s}]$, and particle reaction time as $t_r = \mathcal{O}(10^{-3}) [\text{s}]$ [73, 16]. Equation (B.19) in appendix B, with the assumption of ignition temperature $\theta_{\text{ign}} = 0.75$ and $\text{Le} = 0.75$, yields $u \sim 4 \times 10^{-2} [\text{m}/\text{s}]$ for the characteristic velocity, making the characteristic length (flame width) $\delta_c = \alpha/u = \mathcal{O}(10^{-4}) [\text{m}]$, and $\tau = \delta_c^2/\alpha = \mathcal{O}(10^{-2}) [\text{s}]$ for the model's dimension-less time scale. Figure 2–1 shows typical numerical steady-state profiles of temperature and concentration obtained from the master model with zero and first order kinetics, i.e., $n = 0$ and $n = 1$, and using the above parameters.

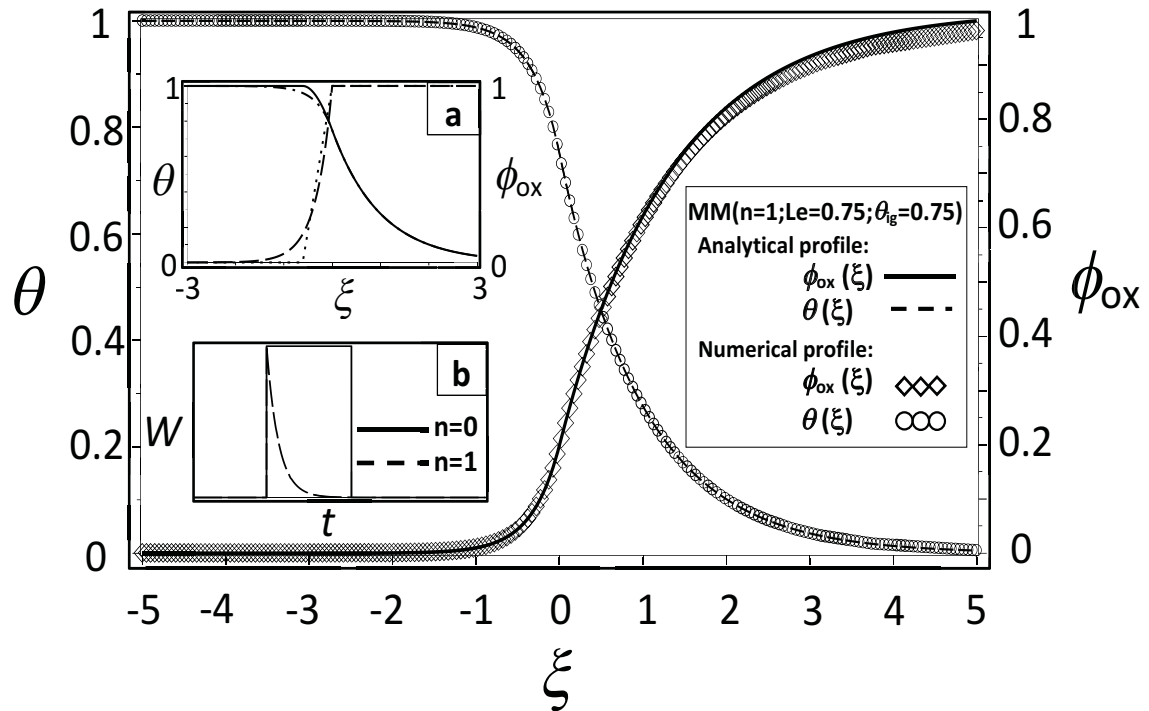


Figure 2–1: Numerical and analytical steady-state profiles of dimension-less temperature and concentration fields for $MM(n = 1; Le = 0.75; \theta_{ign} = 0.75)$. Analytical profiles are hidden under corresponding numerical results. Inset (a) shows solution profiles for $MM(n = 0; Le = \infty; \theta_{ign} = 0.75)$: — analytical temperature profile; analytical concentration profile; and for $MM(n = 0; Le = 0.75; \theta_{ign} = 0.75)$: -·-·- analytical temperature field; - - - analytical concentration profile. Inset (b) shows the schematic source term in time and in the limit of $Le \rightarrow \infty$ for $n = 0$ and $n = 1$ kinetics.

2.1.5 Special Limits of the Master Model Equations

This sub-section analyzes the master model, Equations (2.22) and (2.24), in the limit of $\text{Le} \rightarrow \infty$ for zero and first order kinetics ($n = 0, 1$). Both of these cases were previously examined by [161, 115]. We also discuss briefly a simplification of the master model equations for the case of discrete reactant sources, when the source term is described by Eq. (2.25).

- **Continuum limit, ($n = 0; \text{Le} \rightarrow \infty$)**

In the limit $\text{Le} \rightarrow \infty$ with zero order kinetics the oxidizer equation of the master model can be written as:

$$\frac{\partial \phi_{\text{ox}}}{\partial t} = -A H(\theta(\vec{x}, t) - \theta_{\text{ign}}) H(\phi_{\text{ox}}(\vec{x}, t)). \quad (2.26)$$

Integrating both sides of Eq. (2.26) with respect to the dimension-less time, from 0 to τ_r yields

$$A = \frac{\phi_o}{\left[\int_0^{\tau_r} H(\theta(\vec{x}, t') - \theta_{\text{ign}}) H(\phi_{\text{ox}}(\vec{x}, t')) dt' \right]}, \quad (2.27)$$

where $\phi_o = \phi_{\text{ox}}(\vec{x}, t = 0)$ is the initial value of the oxidizer concentration and $\tau_r = t_r^*/\tau$ is the dimension-less particle reaction time. During the particle reaction time, that is, during the time that combustion is ongoing, $\theta \geq \theta_{\text{ign}}$ and $\phi_{\text{ox}} > 0$. Equation (2.27) thus becomes $A = \phi_o/\tau_r$, and the source term on the right hand side of Eq. (2.26), can be written as

$$W(\vec{x}, t) = \frac{\phi_o H(\theta(\vec{x}, t) - \theta_{\text{ign}}) H(\phi_{\text{ox}}(\vec{x}, t))}{\tau_r}. \quad (2.28)$$

Alternatively, by introducing the ignition time $t_{\text{ign}}(\vec{x})$, the time at which the local temperature at position \vec{x} rises above the ignition temperature, one can make the Heaviside functions in Eq. (2.28) depend explicitly on time [14]. In that case, the source term takes the form

$$W(\vec{x}, t) = \frac{\phi_o H(t - t_{\text{ign}}(\vec{x})) H(\tau_r - (t - t_{\text{ign}}(\vec{x})))}{\tau_r}, \quad (2.29)$$

and the master model reduces to a single heat diffusion equation

$$\frac{\partial \theta}{\partial t} = \nabla^2 \theta + \frac{\phi_o H(t - t_{\text{ign}}(\vec{x})) H(\tau_r - (t - t_{\text{ign}}(\vec{x})))}{\tau_r}. \quad (2.30)$$

Equation (2.30) describes continuum gas-less combustion with ignition temperature kinetics, and is hereafter referred to as the *continuum box model*. The term “box” derives from it being a continuity equation, i.e, describing transport (of heat) in-and-out of a finite region (a “box”) located at position \vec{x} .

The continuum box model corresponds to the limit of the continuum master model with zero-order kinetics in the absence of mass diffusion. Figure 2–2 shows the numerical one-dimensional temperature profile along the principle direction of front propagation (x) obtained using the continuum master model $\text{MM}(n = 0; \text{Le} \rightarrow \infty; \theta_{\text{ign}} = 0.75)$ and using the continuum box model with $\theta_{\text{ign}} = 0.75$ and $\tau_r = \phi_o/18$ (see Appendix B). The inset in Fig. 2–2 shows the velocity evolution of the combustion front in both cases. A difference in the initial front velocities leads to slightly different transients and steady-state front speeds. This can be avoided by directly using the steady-state solution as the initial condition.

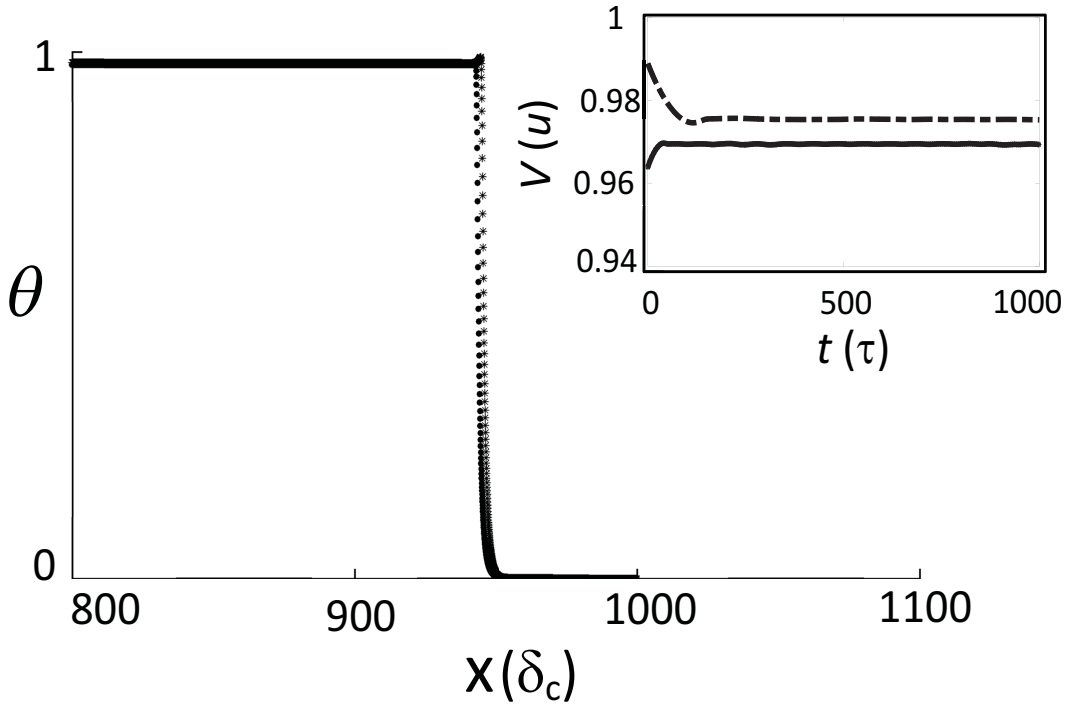


Figure 2–2: Dimension-less temperature profile for a zero-order kinetics combustion front in the absence of mass diffusion, simulated with: () master model at $t = 967.68\tau$, (*) “continuum box model” at $t = 962.56\tau$. The temperature profiles are shifted in time to compare the profiles. Only parts of the profiles around the interfaces are plotted. Inset: average velocity V of the planar front as a function of the simulation time : — master model , - - - continuum box model.

- **Continuum limit, ($n = 1$; $\text{Le} \rightarrow \infty$)**

When considering first order kinetics ($n = 1$) and no mass diffusion ($\text{Le} \rightarrow \infty$), the evolution of the oxidizer concentration in equation (2.22) takes the form

$$\phi_{\text{ox}}(\vec{x}, t) = \phi_o \exp\left[-\int_0^t A H(\theta(\vec{x}, t') - \theta_{\text{ign}}) dt'\right], \quad (2.31)$$

where $\phi_o = \phi_{\text{ox}}(\vec{x}, t = 0)$. The integrand is constant for $0 \leq \tau \leq \tau_r$, hence $A = 1/\tau_r$ defines the time until the oxidizer reaches e^{-1} of its initial value. Now the master model, Eq. (2.22)

and (2.24), can be reduced to a single heat diffusion equation with a source given by

$$W = \frac{\phi_o H(\theta(\vec{x}, t) - \theta_{\text{ign}})}{\tau_r} \left[\exp \left(- \int_0^t \frac{H(\theta(\vec{x}, t') - \theta_{\text{ign}})}{\tau_r} dt' \right) \right]. \quad (2.32)$$

The qualitative difference between the source in this case (continuum, $\text{Le} \rightarrow \infty$, $n = 1$, Eq. (2.32)), and in the previous case (continuum, $\text{Le} \rightarrow \infty$, $n = 0$, Eq. (2.29)) is illustrated in inset b of Fig. 2–1. Both have a finite duration, but while $n = 0$ case is constant and the $n = 1$ case decays exponentially.

- **Discrete limit of the continuum box model in Eq. (2.30)**

Considering discrete particle sources described by Eq. (2.25) in the limit of zero-order kinetics ($n = 0$) and $\text{Le} \rightarrow \infty$, transforms the continuum box model of Eq. (2.30) into the *discrete box model*

$$\frac{\partial \theta}{\partial t} = \nabla^2 \theta + \sum_i A \left[H\left(\frac{1}{A} - (t - t_{\text{ign}})\right) H(\theta - \theta_{\text{ign}}) g(|\vec{x} - \vec{x}_i| - r_p) \right]. \quad (2.33)$$

Here, the inter-particle distance l_p is of the order of the flame front width of a steady-state planar combustion front, and sets the length-scale δ_c in our dimension-less equations, while the dimension-less reaction time becomes $1/A = \alpha t_R^*/l_p^2$. In the limit where particle size r_p is much smaller than the inter-particle spacing l_p , particles can be represented as point-like sources in space, and $g(|\vec{x} - \vec{x}_i| - r_p)$ in Eq. (2.33) can be replaced by $\delta(\vec{x} - \vec{x}_i)$. This model is derived in appendix A, and its detailed analysis has been done by Tang et al. [172].

2.2 Summary

Summarizing, we introduced a unified mathematical combustion model coined the “master model”, for solid metal fuel combustion in the presence of an oxidizer for zero and first-order kinetics, with continuous and random discrete reactant fuel source distributions. The gas-less limit ($\text{Le} \rightarrow \infty$), for both kinetic orders ($n = 0, 1$), was examined analytically to connect the master model to previously established models [161, 115].

CHAPTER 3

Cellular instabilities of Continuum Combustion fronts

In this chapter we explore numerically the morphological patterns of thermo-diffusive instabilities in combustion fronts with a continuum fuel source, within a range of Lewis numbers and ignition temperatures, characterizing the cellular flame front regime. For this purpose, we use continuum master model (Eqs. (2.22) and (2.24)). Cellular and dendritic instabilities are found at low Lewis numbers. A numerical linear stability analysis of the front is conducted, confirming recent analytical results of Brailovsky et al. [22]. Characterizing the long-time front dynamics, three distinct types of dynamics are found in the vicinity of unit Lewis number, ranging from steady-state cellular patterns to continued tip-splitting and cell-merging instabilities. These patterns are well described within the framework of thermo-diffusive instabilities and are consistent with previous numerical studies in other types of reaction-diffusion models. A regime of shallow cells is classified as “quasi-linear” and characterized by low amplitude cells that may be strongly affected by the mode selection mechanism and growth prescribed by the linear theory. Below this range of Lewis number, highly non-linear effects become prominent and large amplitude, complex cellular and *seaweed* dendritic morphologies emerge. Using an adaptive mesh refinement (AMR) numerical, these patterns are characterized at experimentally relevant system sizes for the first time to our knowledge.

3.1 Analysis of Cellular Flame Front Instability- Adiabatic case

Below a critical value of the Lewis number $Le_c \sim \mathcal{O}(1)$, when mass diffusion becomes large enough relative to heat diffusion that the combustion front develops cellular flames. These structures, which have troughs pointing in the direction of the consumed material and convex peaks that grow towards the fresh mixture, span the combustion front in periodic or periodic-like formations [107]. In this section we address the linear stability of cellular fronts numerically and compare our results to the recent analytical predictions of Brailovsky et al. [22]. The intermediate to long-time dynamics and the length-scale selection of cellular flame fronts in the vicinity of Le_c are then examined numerically.

Combustion front instabilities in this chapter are studied using a dynamic adaptive mesh refinement (AMR) technique that allows very large computational domains, thus allowing us to reduce finite size effects that can affect or even preclude the emergence of these patterns. In following section we briefly go over main features of our numerical algorithm. A more detailed discussion about numerical simulation algorithm along with computational codes for post-process can be found in

(https://bitbucket.org/hosseinphy/phd_files).

3.1.1 Numerical Methods

We performed our numerical simulations using a C++ finite difference adaptive mesh refinement (AMR) code that incorporates OpenMP parallelization. The adaptive mesh is based on an algorithm originally introduced by Provatas et al. [146, 10], which is specially suited for modelling free-boundary problems. It greatly decreases CPU times and memory usage in such problems when compared to uniform or fixed grid techniques as it scales

both metrics with the size of the interface rather than with the dimension of the system. The local refinement of the computational mesh is determined by an error estimator that places a threshold on each of the gradients of temperature and concentration. The lowest refinement level, i.e, the smallest grid size, was set to $dx = 0.04$ (in units of the model's characteristic length-scale δ_c). The time step was determined according to the numerical stability criteria for the two dimensional diffusion equation, evaluated using the larger gradient coefficient. Parallelization was performed within 16 core nodes. The simulation domain consisted of a two dimensional rectangle (L_x, L_y) where the spatial coordinates x and y were parallel and normal to the principal direction of flame propagation, respectively. The AMR combined with parallelization allowed us to attain large domain sizes, minimizing finite size effects.

We implemented far-field boundary conditions in the principal direction of flame propagation:

$$\begin{aligned}\theta(+\infty, y) &= 0, & \theta(-\infty, y) &= 1, \\ \phi_{\text{ox}}(+\infty, y) &= 1, & \phi_{\text{ox}}(-\infty, y) &= 0,\end{aligned}\tag{3.1}$$

and zero flux boundary conditions in the lateral direction in order to model adiabatic conditions:

$$\begin{aligned}\frac{\partial \theta}{\partial y}(x, y = 0) &= 0, & \frac{\partial \theta}{\partial y}(x, y = L_y) &= 0, \\ \frac{\partial \phi_{\text{ox}}}{\partial y}(x, y = 0) &= 0, & \frac{\partial \phi_{\text{ox}}}{\partial y}(x, y = L_y) &= 0.\end{aligned}\tag{3.2}$$

3.1.2 Linear regime

A linear dispersion relation of a moving front pairs the linear growth rate ω of a periodic perturbation of a planar interface with the wavenumber k of the perturbation. Brailovsky et al. [22] derived analytically the following dispersion relation for the first order ($n = 1$) kinetics of the master model,

$$\begin{aligned}\Delta(\omega, k, \text{Le}, \theta_{\text{ign}}) &\equiv (q - l)[\theta_{\text{ign}} - 2(1 - \theta_{\text{ign}})p] \\ &[(1 - \text{Le})(\omega - l) - A \text{Le}] + A \text{Le}(p - l) = 0,\end{aligned}\quad (3.3)$$

while for zero order ($n = 0$) kinetics they obtained

$$\begin{aligned}\Delta(\omega, k, \text{Le}, \theta_{\text{ign}}) &\equiv 1 + (1 + 2p)[\exp(-R) - 1] \\ &- \exp[R(\text{Le} - 1 + q - p)] = 0, \\ \theta_{\text{ign}} &= \frac{1 - \exp(-R)}{R},\end{aligned}\quad (3.4)$$

where p, q, l are defined by

$$p = \frac{1}{2}(\sqrt{1 + 4\omega + 4k^2} - 1), \quad (3.5)$$

$$q = -\frac{1}{2}(\sqrt{\text{Le}^2 + 4\text{Le}\omega + 4k^2} + \text{Le}), \quad (3.6)$$

$$l = \frac{1}{2}(\sqrt{\text{Le}^2 + 4\text{Le}(A + \omega) + 4k^2} - \text{Le}). \quad (3.7)$$

In Eq. (3.4), R is the width of the reaction zone. Setting $k = 0$ in the dispersion relation for $n = 1$ kinetics (Eq. 3.3) and $n = 0$ kinetics (Eq. 3.4) and solving for $\omega = 0$, leads to the following critical values of the Lewis number at which $k = 0$ becomes neutrally stable

[22],

$$\text{Le}_c(\theta_{\text{ign}}, k = 0, n = 1) = \frac{\sqrt{16\theta_{\text{ign}} - 15\theta_{\text{ign}}^2 + 2\theta_{\text{ign}}^3 + \theta_{\text{ign}}^4 + \theta_{\text{ign}}^2 - 3\theta_{\text{ign}}}}{(4 - 6\theta_{\text{ign}} + 2\theta_{\text{ign}})^2}, \quad (3.8)$$

for $n = 1$, and for $n = 0$

$$\text{Le}_c(\theta_{\text{ign}}, k = 0, n = 0) = \frac{R}{2 \exp(R) - R - 2}. \quad (3.9)$$

This value of the Lewis number specifies the boundary between the stable (planar) and cellular regimes as a function of ignition temperature. We hereafter identify this value with, and refer to it as, the critical Lewis number $\text{Le}_o = \text{Le}_c(\theta_{\text{ign}}, k = 0, n)$.

To obtain a linear dispersion relation numerically, we perturb a steady-state planar front solution with a small amplitude sinusoidal wave and compute the growth rate of the perturbation at its initial stages, while the evolution of the perturbation's amplitude is purely exponential. More explicitly, given a steady-state planar front solution for the dimension-less temperature field $\theta^{\text{ss}}(x, t)$ and the oxidizer concentration $\phi_{\text{ox}}^{\text{ss}}(x, t)$, we use as initial condition $\theta^{\text{ss}}(x - A(y), t)$ and $\phi_{\text{ox}}^{\text{ss}}(x - A(y), t)$ with $A(y) = A_o \cos(ky)$ where A_o is the amplitude of the perturbation, k is its normal wavenumber and $\lambda = 2\pi/k$ its wavelength. The growth rate is defined by $\omega = (1/A)dA/dt$, and the regime is considered linear as long as the growth rate increases linearly in time.

Linear dispersion calculations were performed for different transverse wave numbers for both zero order kinetics $\text{MM}(n = 0; \text{Le} = 0.3; \theta_{\text{ign}} = 0.75)$ and first order kinetics $\text{MM}(n = 1; \text{Le} = 0.6; \theta_{\text{ign}} = 0.75)$. The lateral dimension of the system was set to half of the perturbation's wavelength, and was varied according to the wavelength analyzed. The

resulting dispersion computations are shown in Fig. 3–1 (main). The respective analytical solutions of Brailovsky et al., shown in the same figure, are in excellent agreement. In

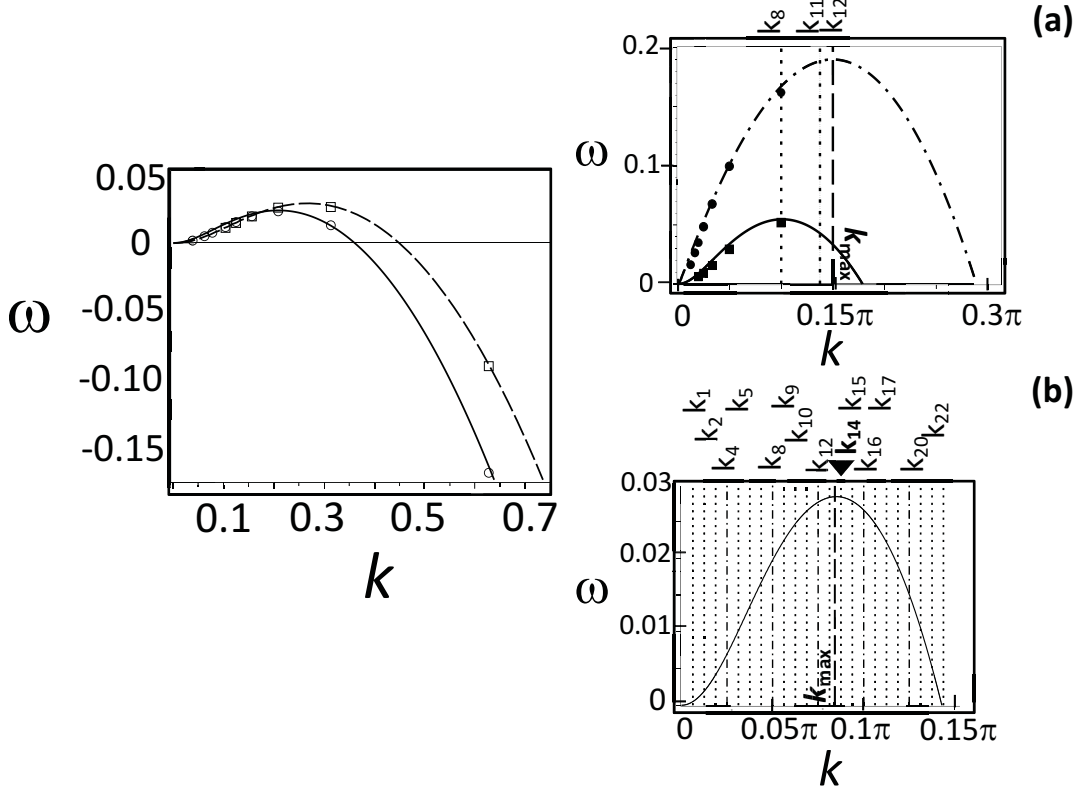


Figure 3–1: Linear growth rate ω normalized with the characteristic time τ versus the wavenumber k of the perturbation normalized by $\delta_c/2\pi$. Left: Dispersion relation for $MM(n = 1; Le = 0.6; \theta_{ign} = 0.75)$: — — analytical, \square numerical; $MM(n = 0; Le = 0.3; \theta_{ign} = 0.75)$: — analytical, \circ numerical. Right: (a) Dispersion relation for $MM(n = 1; Le = 0.5; \theta_{ign} = 0.75)$: — analytical, \blacksquare numerical; $MM(n = 1; Le = 0.05; \theta_{ign} = 0.75)$: — — analytical, \bullet numerical. Some permissible k modes for $(n = 1; Le = 0.05; \theta_{ign} = 0.75)$ in a system with $L_y = 160 \delta_c$: ... (b) Dispersion relation for $(n = 1; Le = 0.6; \theta_{ign} = 0.75)$. Permissible k modes in a system with $L_y = 80 \delta_c$: -.-. and $L_y = 320 \delta_c$: k_{\max} is specified in both (a) and (b) by dashed line.

Fig. 3–1 (main), the dispersion relation for first order kinetics ($n = 1$) has a larger range of unstable k modes than that for zero order ($n = 0$) kinetics, as well as a larger maximum growth rate. This is because with zero order kinetics ($n = 0$), the rate of heat release

throughout the reaction zone is constant, making the front more stable against perturbations than in the corresponding first order kinetics ($n = 1$) case. The same effect, i.e., increasing the range of unstable k modes and the maximum growth rate, can be achieved by decreasing the Lewis number while holding all other parameters fixed, as illustrated in Fig. 3–1(a). Therefore, one can make the first order kinetics ($n = 1$) case comparable to the zero order kinetics ($n = 0$) case by increasing the mass transport rate or by decreasing the heat diffusion.

3.1.2.1 Effect of system size on linear mode selection

To examine the effect of system size on growth modes, we consider the evolution of an initially noisy front by perturbing a planar steady-state solution with local point-to-point random morphological fluctuations whose amplitude varies between 0 and A_o . It is noted that given the non-flux boundary conditions in the transverse y -direction of the system, only modes that are in multiples of the width of the system, $L_y, 2L_y, 4L_y, \dots$ are attainable. Some of the accessible modes available for two systems of width $L_y = 80\delta_c$ and $L_y = 320\delta_c$ ($n = 1$; $\text{Le} = 0.6$; $\theta_{\text{ign}} = 0.75$) are displayed on the dispersion relation in Fig. 3–1(b). The actual selected modes at early times for these two systems sizes are shown in Fig. 3–2. This figure highlights the correlation between the number of potential unstable k modes and the transverse domain size. Two modes, $k_8 = 0.05\pi/\delta_c$ and $k_{16} = 0.1\pi/\delta_c$, are excited in the smaller system $L_y = 80\delta_c$. The highest of these two peaks (k_{16}) is close to the most unstable mode k_{\max} shown in the dispersion relation in Fig. 3–1(b), while the other is double the wavelength. Both are, as expected, multiples of the width of the system. With the wider system, the number of modes excited is larger and the highest peak

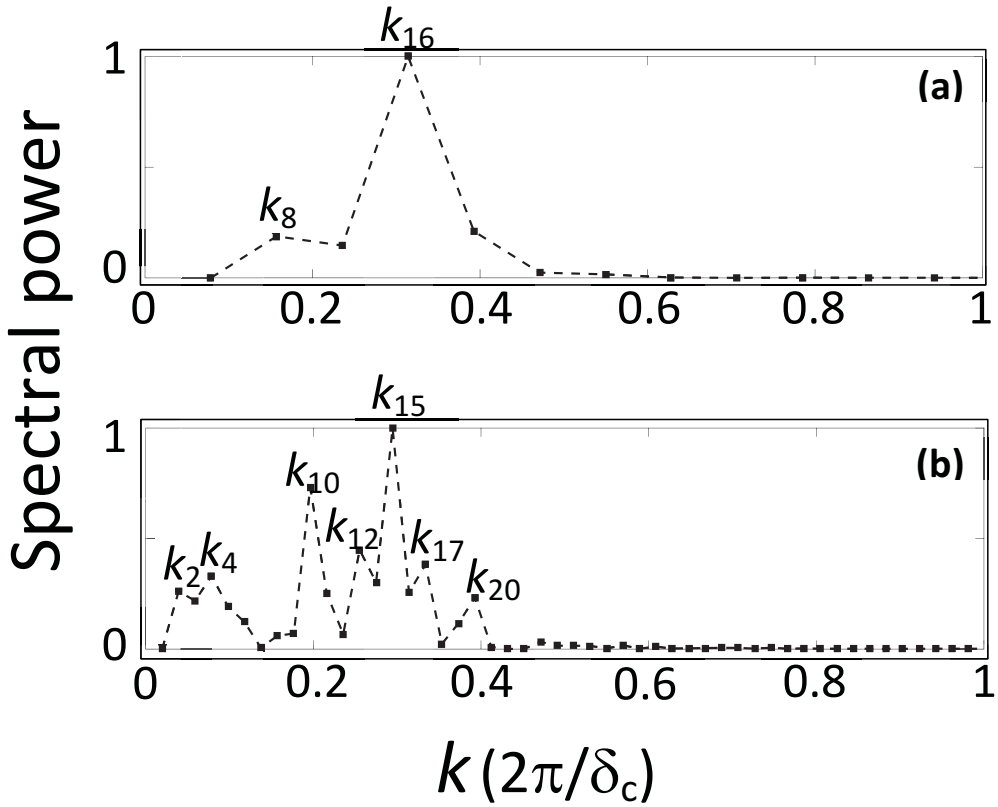


Figure 3–2: The normalized spectral power of the 1D interface $x = f(y, t)$ with model parameters MM($n = 1$; $\text{Le} = 0.6$; $\theta_{\text{ign}} = 0.75$). The unstable k modes in the linear regime under noisy initial conditions are shown for lateral domain sizes corresponding to (a) $L_y = 80 \delta_c$ at $t = 76\tau$, (b) $L_y = 320 \delta_c$ at $t = 69\tau$.

(k_{15}) is closer to k_{\max} of Fig. 3–1(b). The larger the transverse system size L_y , the more dense is the set of excitable modes attainable. Thus, the number of modes that can be potentially excited becomes larger, with the fastest growing mode becoming closer to the analytical prediction (k_{\max} of Fig. 3–1(b)) in the bigger system. Our numerical results are also consistent with other studies on the effect of system size on the mode selection mechanism [44, 31].

3.1.2.2 Effect of Lewis number on linear mode amplitudes

The stability of the combustion front mode with respect to the Lewis number is shown in Fig. 3–3 for the case of MM($n = 1; \text{Le}; \theta_{\text{ign}} = 0.75$). The Lewis number axis is reference to Le_o given by Eq.(3.8). The curves are obtained using Eq. (3.3). Each curve corresponds to a given growth rate, thus the intersection of a $k = \text{const}$ line with a given curve gives the growth rate of that k mode at a specific Le . The range of unstable k modes narrows with increasing Lewis number. As discussed above, the number of attainable transverse k modes is limited by the system transverse size (Fig. 3–1(b)). The discrete k modes obtained using a system with a lateral size $L_y = 80 \delta_c$, for two different values of Le , are marked (●)

Figure 3–3 also includes the evolution of the amplitude and a typical late-time morphology for two different values of the Lewis number ($\text{Le} = 0.05, \text{Le} = 0.6$) and the same initial perturbation mode $k = 0.05\pi/\delta_c$. After an initial transient period, the amplitude in both cases grows linearly with time. It is noteworthy that for the smaller values of Le , the amplitude of the perturbation grows faster and thus the system will transit more rapidly to what is expected to be a strongly non-linear regime. Conversely, as $\text{Le} \rightarrow \text{Le}_o$ the growth

rate drops. Systems with Le in this range take longer to transition from the linear to the non-linear regime, and they are expected to exhibit only weakly non-linear behaviour, even at late times.

3.1.3 Quasi-Linear Regime as $\text{Le} \rightarrow \text{Le}_o$

The results of the last sub-section suggest that as $\text{Le} \rightarrow \text{Le}_o$ the amplitude governing fluctuations of the combustion front will evolve slowly from zero at intermediate to late times, possibly even saturating at very late times. As a result, the transition of the combustion front from linear to non-linear growth dynamics will be long, making it plausible that its morphologies, in this parameter regime, can be qualitatively analyzed over long time periods in terms of the fastest growing linearly unstable k modes. This intermediate regime, which we call here the *quasi-linear regime*, is further examined below.

3.1.3.1 Effect of initial condition and system size on the dynamics of the interface

We first consider a planar steady-state front with an initial sinusoidal morphological perturbation, for two systems that have the same length $L_x = 2000 \delta_c$ but different widths, given by $L_y = 80 \delta_c$ and $L_y = 320 \delta_c$, respectively. For visualization purposes the figures presented focus on the front and only show a partial view of the whole system that includes a range of $30 \delta_c$ around the front. For the initial sinusoidal perturbation we choose k modes within the corresponding linear unstable range that are commensurate with the width of the system. Figure 3–4 shows two instances in the evolution of the combustion front for model parameters $\text{MM}(n = 1; \text{Le} = 0.6; \theta_{\text{ign}} = 0.75)$, a system with $L_y = 80 \delta_c$, and an initial pure k -mode perturbation corresponding to $k_8 = 0.05\pi/\delta_c$ (see Fig. 3–1(b)). The full simulation

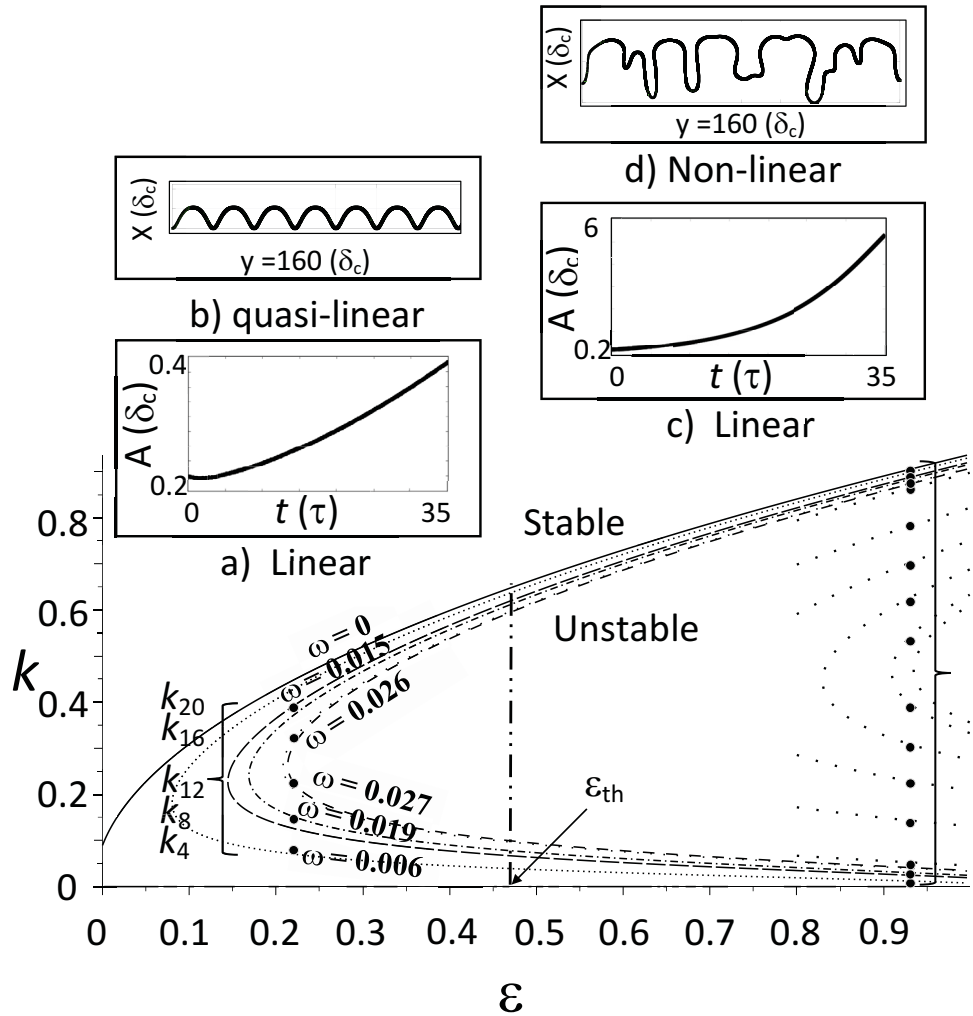


Figure 3–3: Stability space for $MM(n = 1; Le; \theta_{ign} = 0.75)$ for $Le < Le_o$ where the horizontal axis is the parameter ε defined as $(Le_o - Le)/Le_o$ and the vertical axis is the wavenumber k normalized by $\delta_c/2\pi$. Curves which are obtained using Eq. (3.3) define contours of fixed normalized growth rate ($\omega \geq 0$) of perturbations with transverse k mode. Attainable normal modes for system size $L_y = 80\delta_c$ for $Le = 0.6$ and $Le = 0.05$, are denoted by ●. Top-Left inset: (a) and (b) show the evolution of the amplitude and a typical late-time morphology of an interface that was initially perturbed with a sinusoidal wave with $k = 0.05\pi/\delta_c$, for the case of $Le = 0.6$. Top-Right inset: (c) and (d) show the evolution of the amplitude and a typical late-time morphology of a sinusoidally perturbed interface with $k = 0.05\pi/\delta_c$ after a long time in its evolution, for the case $Le = 0.05$. ε_{th} in the figure specifies the border between the shallow amplitude (left side) and the large amplitude (right side) cellular regime.

run corresponds to $t = 1900 \tau$, and steady-state is reached after $t = 70 \tau$. Figure 3–5 tracks

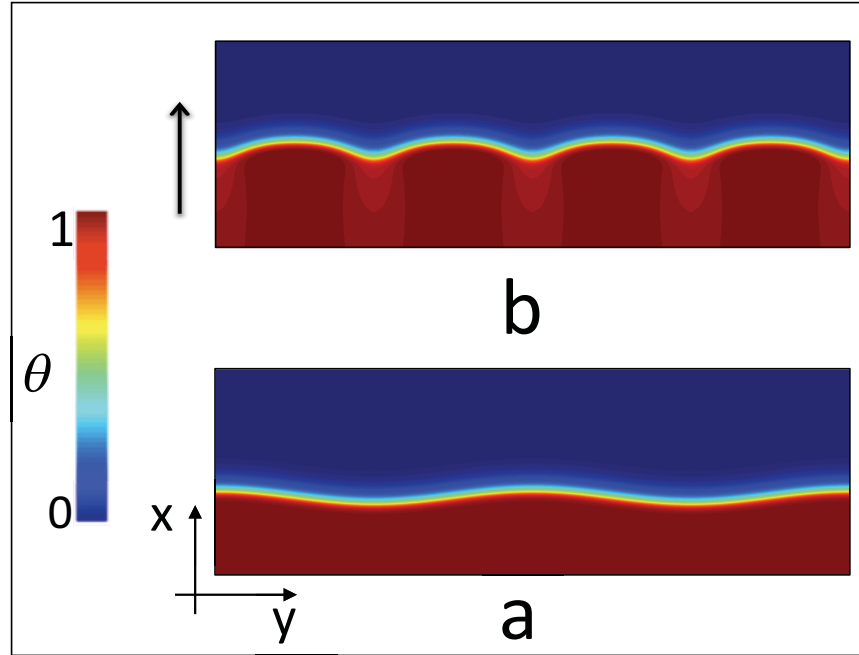


Figure 3–4: Contours of the dimension-less temperature field in a moving frame for model parameters $MM(n = 1; Le = 0.6; \theta_{ign} = 0.75)$ and system size $L_y = 80 \delta_c$. a) initial perturbation wavelength $\lambda = 40 \delta_c$ ($k_8 = 0.05\pi/\delta_c$), b) steady-state front configuration. The arrow shows the direction of propagation along x coordinate. Colour-bar on the left hand side of the figure shows the dimension-less temperature scale.

the evolution of the interface shown in Fig. 3–4, defined via the temperature isotherm $\theta(x, y) = \theta_{ign} = 0.75$. The initial sinusoidal perturbation ($k_8 = 0.05\pi/\delta_c$) flattens due to the high temperature gradient at the tips. Concurrently, troughs become more pronounced as the cells evolve towards their steady-state shape. Deep grooves form at approximately $t = 5\tau$, followed by the flattening of the cell tips signalling an upcoming cell splitting event. Around $t = 25\tau$, the flattened segments become unstable, eventually splitting into two new identical cells and the whole front settles into a steady-state cellular front with half the wavelength (i.e. cell spacing) of the initial perturbation, $k = k_{16} = 0.1\pi/\delta_c$. This mode is

within allowable modes for this system, but also much closer than the initial perturbation to the most unstable linear mode k_{\max} predicted by the dispersion relation in Fig. 3–1(b). The

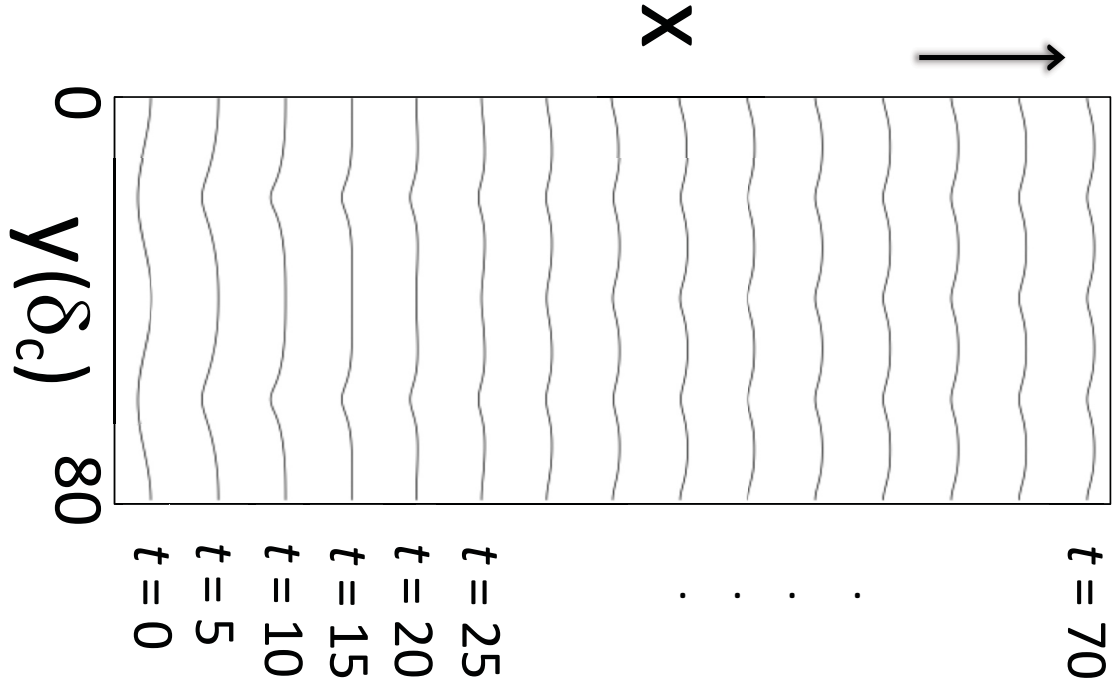


Figure 3–5: The sequence of the time evolution of the front, defined by the isotherm $\theta(x, y) = \theta_{\text{ign}} = 0.75$ in Fig. 3–4. Time is in units of time-scale τ and the isotherm is plotted every 5τ . The arrow defines the direction of propagation along x coordinate.

morphological evolution just described is caused by an interplay between an instability driven by diffusive transport and the effect of surface curvature, as discussed by Zeldovich et al. [192]. Tip splitting as a route for achieving a stable cell array in combustion fronts has been reported in experiments [170, 122] as well as in numerical studies [44, 80, 160, 162]. Tip splitting as a microstructure selection mechanism is also well known in the context of crystal growth [126, 125, 26, 27, 92, 176, 62, 67, 66]. Figure 3–6 shows the evolution of a flame front with the same model parameters and system size as in Fig. 3–4,

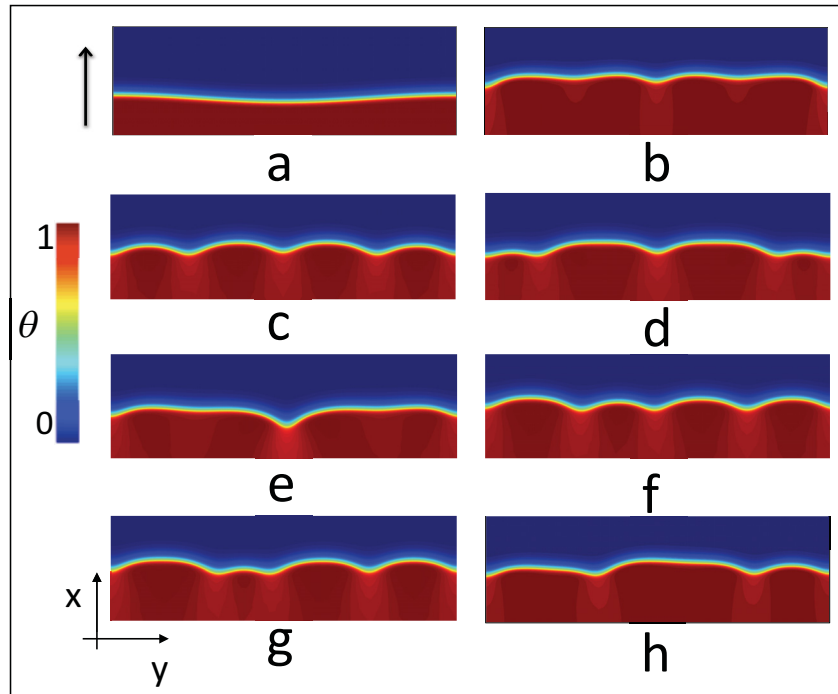


Figure 3–6: Evolution of the dimension-less temperature field for model parameters $\text{MM}(n = 1; \text{Le} = 0.6; \theta_{\text{ign}} = 0.75)$ from (a): the initially perturbed front with wavelength $\lambda = 80 \delta_c$ to (h): the final state in the computation. The arrow shows the direction of propagation along x coordinate. Colour-bar on the left hand side of the figure shows the dimension-less temperature scale.

but with an initial pure k -mode perturbation corresponding to $k_4 = 0.025\pi/\delta_c$ (see Fig. 3–1(b)). Here, we observe that the initial front in (a) undergoes several cell-merging and tip-splitting events and, at least to the end of our simulation in (h) at $t = 1900\tau$, the system does not reach steady-state. Note that the initial perturbation mode $k_4 = 0.025\pi/\delta_c$ is equal to $2\pi/L_y$, the smallest wavenumber allowed by this system size.

In Fig. 3–6(a) the initial sinusoidal perturbation has a wavelength equal to the width of the system. This initial perturbation, which is both very small in the context of the dispersion relation and theoretically the lowest attainable k in the linearly unstable regime for this system size, fails to select a unique wavelength (spacing) in this range as it is overrun by higher order finite-size effects. Consequently, it does not reach a steady-state. As seen in Fig. 3–6, rather than developing a single spacing wavelength compatible with the system size, the front develops a combination of different wavelengths whose competition leads to successive local cell-merging and tip-splitting events but does not settle into a single mode steady-state. It is possible that numerical fluctuations play a role, but in any case, these are smaller than the thermal fluctuation one would expect in a real physical system. We expect that the same model parameters and initial condition in a wider system can lead to a single spacing steady-state corresponding to that of one of the faster growing allowable modes of the linear dispersion curve, after undergoing one or more tip splitting instabilities.

To explore this, we considered the same model parameters as in Fig. 3–6, with an initially perturbed interface having k_4 or k_8 modes in a wider system of lateral size $L_y = 320\delta_c$. Two instances of the late-time evolution of the front, for each initial condition,

are presented in Fig. (3–7). In both cases the system reaches a steady-state with wavelength k_{14} (in Fig. 3–1(b)), which is close to the steady-state wavelength k_{16} reached by the smaller system (Fig. 3–4(b)) with an initial perturbation of $k = k_8 = 0.05\pi/\delta_c$. As expected, when considering the larger system, both cases lead to a single spacing steady-state corresponding to a wavelength close to the fastest growing modes (i.e. k_{\max}) in the linear regime of the model, after undergoing several tip splitting events.

The spectral power density of the interface, after reaching the steady-state for the conditions of Fig. 3–7, is shown in Fig. 3–8. The dominant steady-state mode selected, k_{14} (marked by \blacktriangledown in Fig. 3–1(b)), is remarkably close to the value of k_{\max} predicted by the dispersion relation. The predilection of the system to settle into a steady-state with a dominant mode close to the mode with the highest growth rate predicted by the linear stability analysis was further confirmed by simulating the same model parameters and system size $L_y = 320 \delta_c$ with an initial perturbation mode equal to k_{14} , which resulted in a steady-state pattern identical to the ones in Fig. 3–7 (left/right). Note that the steady-state spacing selected in the case of the larger system (dominant mode = k_{14}) is closer to the wavelength of the mode with the highest growth rate predicted by the linear stability analysis (k_{\max}) than the steady-state spacing selected in the case of the smaller system (dominant mode = k_{16}). The higher density of allowable modes in the vicinity of k_{\max} available to the larger system likely accounts for this wavelength selection mechanism.

It is instructive to examine the evolution of the front for an initial morphologically noisy interface, which contains a combination of many modes and thus can be used to examine their interaction. For this purpose, we examine the evolution of an initially noisy front, obtained by perturbing a planar steady-state solution with a local point-to-point

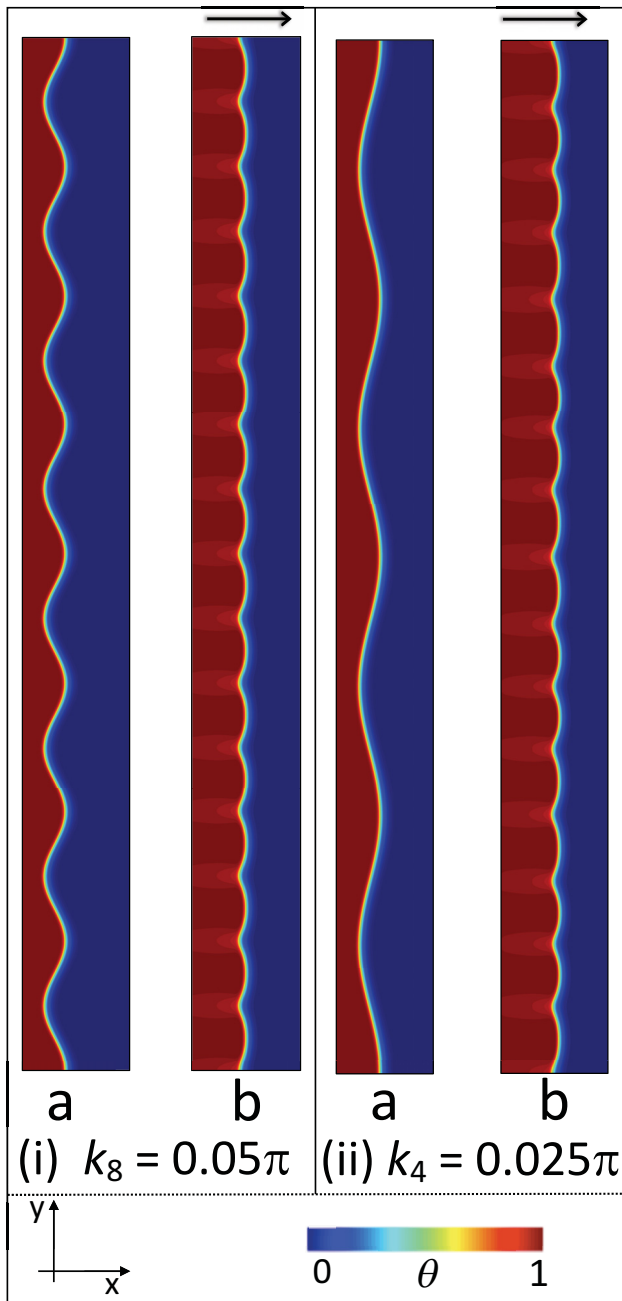


Figure 3–7: Contour plots of dimension-less temperature field for model parameters $\text{MM}(n = 1; \text{Le} = 0.6; \theta_{\text{ign}} = 0.75)$ in the system $L_x = 2000$ and $L_y = 320$. Left: a) initial perturbation with $k = 0.05\pi/\delta_c$ b) steady-state. Right: a) initial perturbation with $k = 0.025\pi/\delta_c$ b) steady-state. Top arrows show the direction of propagation along x coordinate. Colour-bar shows the dimension-less temperature scale.

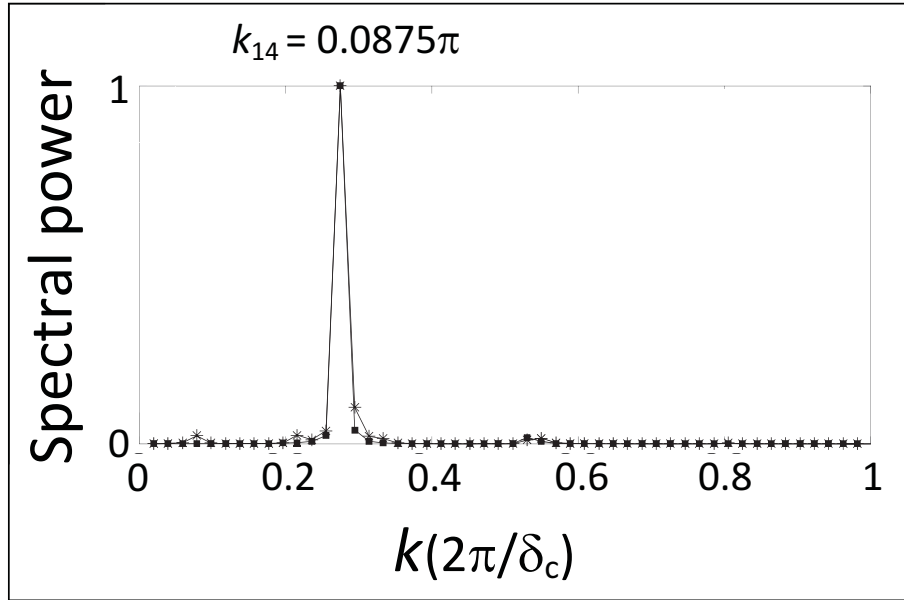


Figure 3–8: The normalized spectral power of the interface $x = f(y, t)$ of the steady-state for the two different initial perturbation modes in Fig. 3–7: $k_8 = 0.05\pi/\delta_c$ (■) and $k_4 = 0.025\pi/\delta_c$ (*).

random morphological fluctuation with small amplitude for computational domains with $L_y = 80 \delta_c$ and $L_y = 320 \delta_c$. To study the long-time dynamics of the system, in both cases, a sufficiently large simulation box in the growth direction was chosen, with $L_x = 5000 \delta_c$. The duration of the simulation for smaller and larger system size was 4580τ and 5500τ , respectively.

Here we find that the front morphology does not converge to steady-state in either case. Instead, the front develops a state where cells are randomly created and annihilated due to localized tip-splitting and cell merging. A partial view of the resulting temporal history of a 1D front $x = f(y, t)$ in the larger domain ($L_y = 320 \delta_c$) is shown in Fig. 3–9. Figure 3–10 presents the spectral power of the 1D interface that develops in the larger and smaller system at late times. These spectra indicate, as expected, that the front adopts a pattern that

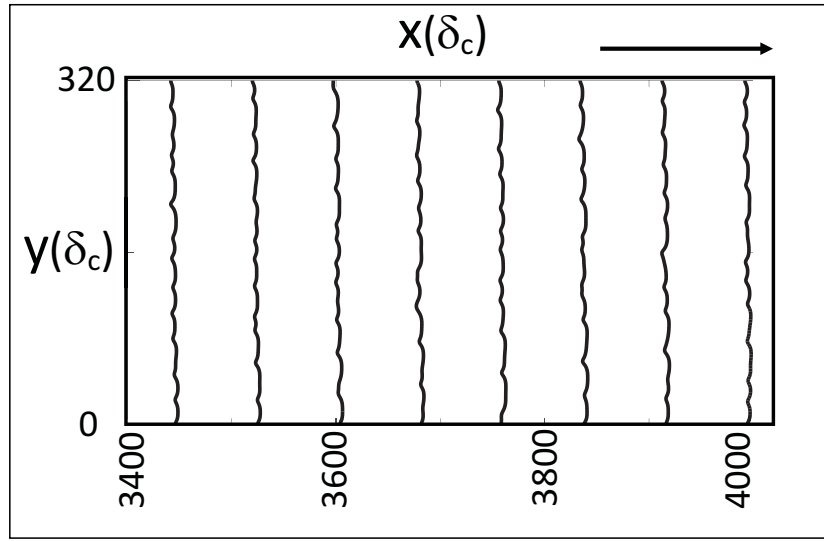


Figure 3–9: Temporal history of evolution of 1D front corresponding to isotherm $\theta(x, y) = \theta_{\text{ign}}$ for model parameters MM($n = 1$; $\text{Le} = 0.6$; $\theta_{\text{ign}} = 0.75$) with initial morphologically noisy interface and in the system size $L_x = 5000 \delta_c \times L_y = 320 \delta_c$. The isotherm is plotted every $\sim 82\tau$. The arrow shows the direction of propagation.

is, to lowest order, dominated by the modes available to the system (see Fig. 3–1(b)). The spectral power in Fig. 3–10 reveals that the larger system can trigger more of the modes from Fig. 3–1(b) in the states it adopts, consistent with the earlier discussion about the correlation between system size and mode selection. It is found that the peaks comprising the spectral power of the interface rise and fall during its evolution. As anticipated for the quasi-linear regime, the growth rate of each peak during a "rising" phase closely follows the growth rate predicted from the linear dispersion relationship in Fig. 3–1(b)).

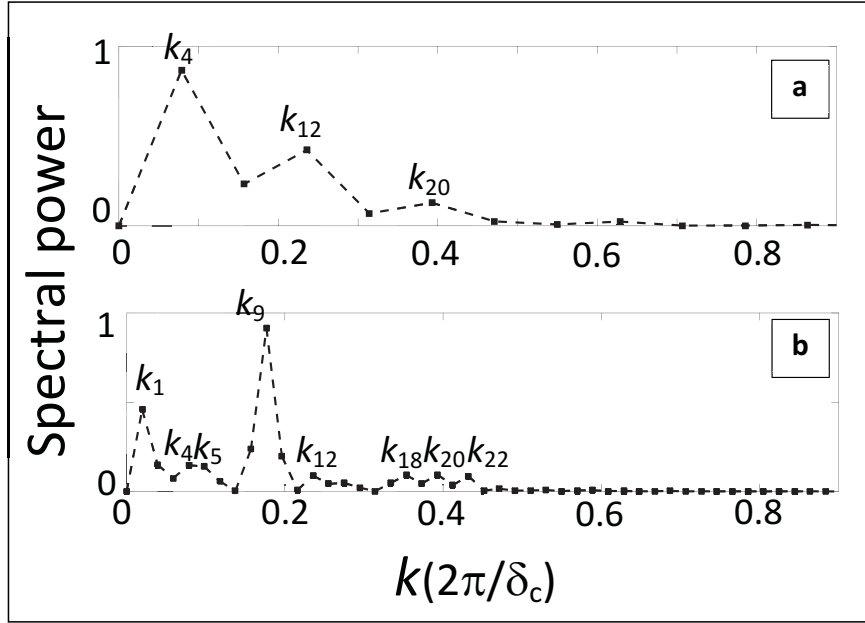


Figure 3–10: The normalized spectral power of the interface $x = f(y, t)$ for model parameters MM($n = 1$; $\text{Le} = 0.6$; $\theta_{\text{ign}} = 0.75$): a) $L_y = 80 \delta_c$ at $t = 76\tau$, b) $L_y = 320 \delta_c$ at $t = 69\tau$. Interfaces evolve from a noisy initial condition. The modes into which the late-time interface decomposes are indicated for each system size.

3.1.3.2 Effect of Lewis number on the morphology

As discussed earlier, when the value of the Lewis number Le decreases a rapid transition to strongly non-linear behaviour is expected, signalled by complex interface morphologies and large tip-to-groove amplitudes. To further illustrate this, we examined simulations with model parameters MM($n = 1$; $\text{Le}; \theta_{\text{ign}} = 0.75$) where $0.1 \leq \text{Le} \leq 0.6$. Since the time scale τ in our system depends on the value of the Lewis number (see appendix B), we rescale time for each Le studied here according to

$$\tau(\text{Le}') = \left(\frac{1 + \frac{\theta_{\text{ign}}}{\text{Le}'(1-\theta_{\text{ign}})}}{1 + \frac{\theta_{\text{ign}}}{\text{Le}(1-\theta_{\text{ign}})}} \right) \tau(\text{Le}), \quad (3.10)$$

where a reference time-scale, τ_{ref} , is chosen to correspond to the largest Lewis number employed ($\text{Le} = 0.6$). The size of the computational domains used is given by $L_x = 600 \delta_c$ and $L_y = 160 \delta_c$. To isolate the effect of Le we use the same initial conditions in all cases, consisting of a planar steady-state with a sinusoidal perturbation of wavenumber $k = k_8 = 0.05\pi/\delta_c$.

Typical late-time interface configurations for different Lewis numbers are shown in Fig. 3–11. The times indicated in the figure are with respect to the reference time-scale τ_{ref} . The observed trend is consistent with the results in Fig. 3–3 and our previous discussion. For the larger values of the Lewis number, the front develops a shallow cellular morphology and reaches a steady-state with spacing dominated by a single mode. With lower values of the Lewis number, highly non-linear effects dominate the evolution of the front, including strong mode interactions, non-symmetrical cells of different depths, and overhangs. Figure 3–12 plots the dependence of the cell amplitude with Le . Cell depth h is defined as max-to-min positions on the interface. For Lewis number in the range depicted in the figure ($0.5 \leq \text{Le} \leq 0.7$) and for the given model parameters, a front develops a single mode steady-state. The average amplitude of the cells decreases with increasing Lewis number and becomes very small as Le approaches its critical value (Le_0).

3.1.4 Non-Linear Front Dynamics for Small Le : Seaweed Fronts

This section examines non-linear combustion fronts in the limit of low Lewis number ($\text{Le} < 0.4$). In this regime, nonlinear effects dominate the dynamics and the front develops complex morphologies involving multiple deep cells with overhangs, or dendritic fingers.

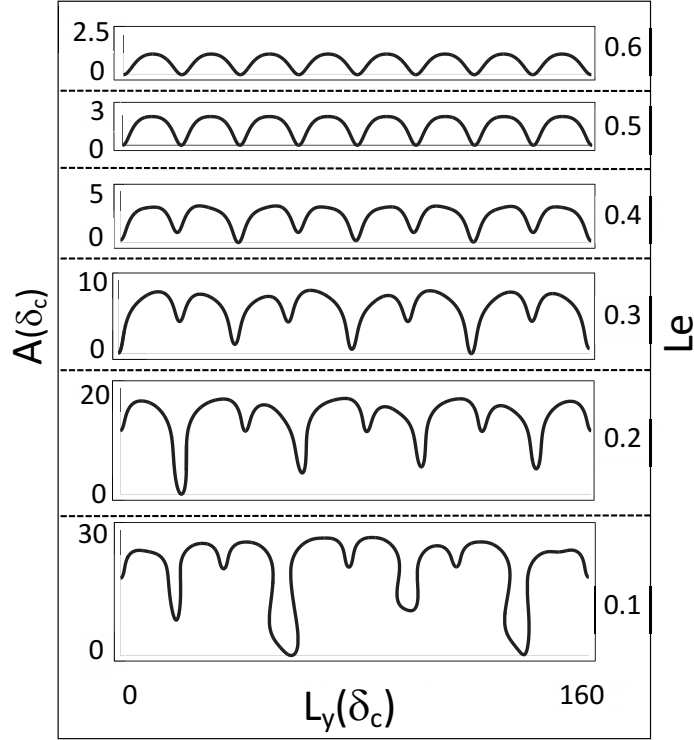


Figure 3–11: Amplitude of cellular pattern for model parameters $\text{MM}(n = 1; \text{Le}; \theta_{\text{ign}} = 0.75)$ for range of Lewis numbers $0.1 \leq \text{Le} \leq 0.6$. A sinusoidal perturbation with $k = 0.05\pi/\delta_c$ mode is used for the initial condition. The time of each image is $t_{\text{Le}=0.1} = 1281.33 \tau_{\text{ref}}$, $t_{\text{Le}=0.2} = 885.24 \tau_{\text{ref}}$, $t_{\text{Le}=0.3} = 669.02 \tau_{\text{ref}}$, $t_{\text{Le}=0.4} = 469.24 \tau_{\text{ref}}$, $t_{\text{Le}=0.5} = 386.04 \tau_{\text{ref}}$, $t_{\text{Le}=0.6} = 332.8 \tau_{\text{ref}}$. The reference time τ_{ref} corresponds to $\text{Le} = 0.6$.

As a specific case study, we probe the front dynamics for model parameters $\text{MM}(n = 1; \text{Le} = 0.05; \theta_{\text{ign}} = 0.75)$. To investigate the size effect in the non-linear regime of the front evolution, two domain sizes were used, $(L_x = 600 \delta_c, L_y = 80 \delta_c)$ and $(L_x = 600 \delta_c, L_y = 160 \delta_c)$. A planar steady-state solution for each case is perturbed initially with a sinusoidal wave with $k = 0.05\pi/\delta_c$ and $k = 0.025\pi/\delta_c$, respectively. The evolution of the front morphology $x = f(y, t)$ for the smaller domain is shown in Fig. 3–13. The combustion front, defined as the isotherm $\theta(x, y) = \theta_{\text{ign}} = 0.75$, is plotted every $\Delta t = 2.6 \tau$. The

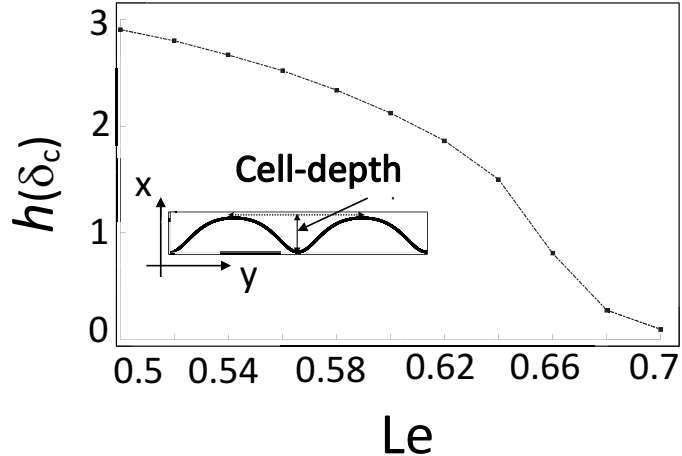


Figure 3–12: Cell depth parameter h in units of δ_c versus Le . Inset shows a steady-state cellular interface for model parameters $MM(n = 1; 0.5 \leq Le \leq 0.7; \theta_{ign} = 0.75)$ at late time, $t = 300 \tau(Le)$. Cell depth measures the max-to-min positions on the interface.

duration of the simulation was 416τ . Three stages of the front evolution are indicated in Fig. 3–13, regions i, ii, and iii.

At the early times of stage i, the perturbed front evolves into crests that have better access to the oxidizer than the troughs since, by geometry, replenishing of burned fuel is more effective ahead of the crests. Thus the crests grow faster than the bottom of the troughs, which remain close to their initial position, and the front develops cells that deepen. When the cells are deep enough they develop a lateral instability. All fingers tip split, shortly after which elimination of two pairs of new fingers occurs. In Fig. 3–13, this corresponds to the end of region i. As the surviving cells continue to grow and deepen in region ii, a lateral instability begins to develop again, with some of the tip-split fingers becoming overgrown while others grow until they become unstable themselves at the end of region ii. Throughout regions i and ii, no steady-state pattern emerges as cells grow, split and compete, with some becoming eliminated while others grow.

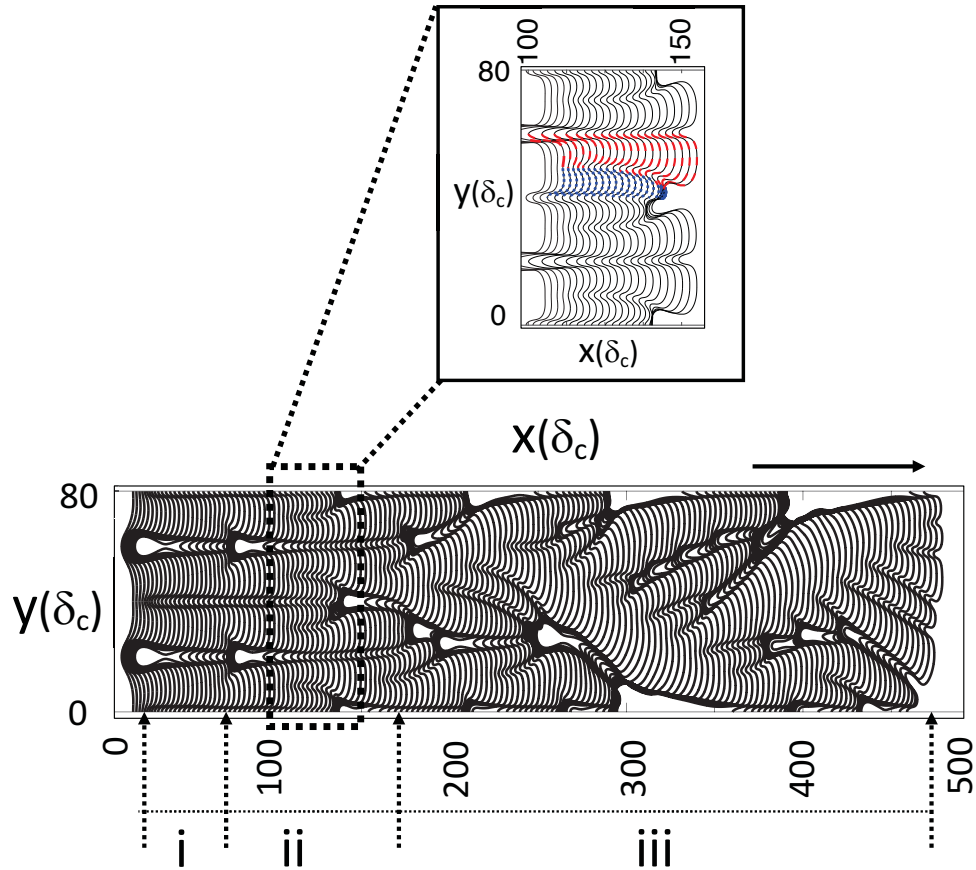


Figure 3–13: (Colour online) Temporal history of evolution of 1D front corresponding to isotherm $\theta(x, y) = \theta_{\text{ign}}$ for model parameters MM($n = 1$; $\text{Le} = 0.05$; $\theta_{\text{ign}} = 0.75$) with initial sinusoidal wave mode $k = 0.05\pi/\delta_c$ and in the system size $L_x = 600\delta_c$, $L_y = 80\delta_c$. Dotted arrows define the approximate border between zones **i**, **ii**, and **iii**. Inset: zoom-in of a tip-splitting event and a cell elimination event in region **ii**. Colours represent different length scales emerging in the tip-splitting process, with **dashed red line** representing a large cell and **dotted blue line** a small cell. The direction of front propagation is shown by the arrow.

A highly non-linear regime follows in region **iii**. The front does not establish a dominant growth pattern due to system size confinement. Instead, one of the surviving cells from region **ii** undergoes a rapid series of tip-splitting and cell overgrowth events, with one of the tertiary branches eventually overgrowing all previous branches in the system.

The evolution of this surviving branch then follows itself a series of tip splitting instabilities into primary and tertiary branches. The pattern of side-branching behaviour shown in Fig. 3–13 is the hallmark of *seaweed* dendritic growth.

The above process of finger instability, tip-splitting, and cell elimination in region ii are better depicted in the inset of Fig. 3–13. It is noteworthy that the mode dominating the front pattern at early stages is fairly close to $k_{\max} = 0.15\pi/\delta_c$, the fastest growing mode predicted by the linear stability analysis for the same model parameters shown in Fig. 3–1(a).

The evolution of the combustion front for the larger system ($L_y = 160 \delta_c$) is shown in Fig. 3–14. The isotherm defining the combustion front $\theta(x, y) = \theta_{\text{ign}} = 0.75$ is plotted every $\sim 5.12 \tau$, and the duration of the complete simulation corresponds to 460τ . The front evolution initially follows a similar qualitative evolution to that of the smaller system for stages i and ii described above. After the second stage, however, the front establishes a “quasi-regular” pattern. This can be seen in Fig. 3–14 starting with the four surviving secondary branches (dashed-dotted green cells). These split into eight tertiary branches (dash-dotted red cells at $x/\delta_c \sim 150$). Only one of these survive, to split a little later into quatertertiary branches (dashed-dotted blue cells). Among these, only one survive and grow wide enough laterally to become comparable in original secondary branches (dashed-dotted green cell)). After this point, the above process likely repeats again, making the morphology statistically repetitive. However, to confirm this for sure, a statistical analysis of branch number and spacing over a much greater time would have to be measured.

We compare the numerically approximated k modes associated with various primary (dotted green cells), secondary (dash-dotted red cells), and tertiary (blue (dark gray) cells)

splittings in Fig. 3–14 with the linear modes from the dispersion relation (Fig. 3–1(a)) for the given model parameters ($\text{Le} = 0.05$, $\theta_{\text{ign}} = 0.75$) and the corresponding system size. Our analysis shows that the length scale of the dotted green cells corresponds to an approximate wavenumber $k = k_{11} = 0.1375\pi/\delta_c$, which is remarkably close to $k_{\max} = 0.15\pi/\delta_c$. These cells, however, split into the eight branches (dash-dotted red cells) with dominant mode $k = k_8 = 0.1\pi/\delta_c$, which is not close to the fastest growing mode in the corresponding dispersion relation. A detailed analysis of spacing selection in the non-linear regime is beyond the scope of this work. Spacing selection in the non-linear regime has a long history in solidification studies [5, 65] and while insight can be gained from analyses like the one above, it still represents a largely unsolved problem. The difference in the front

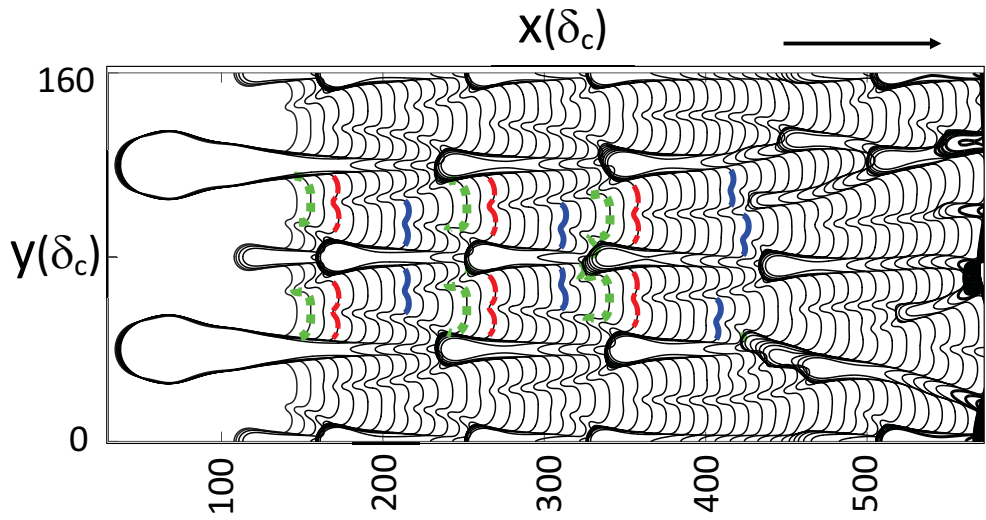


Figure 3–14: (Colour online) Temporal history of evolution of 1D front corresponds to isotherm $\theta(x, y) = \theta_{\text{ign}}$ for model parameters MM($n = 1$; $\text{Le} = 0.05$; $\theta_{\text{ign}} = 0.75$). The initial interface is a sinusoidal wave mode $k = 0.025\pi/\delta_c$ and system size is $L_x = 600\delta_c$, $L_y = 160\delta_c$. Colours represent different length scales emerging in the tip-splitting process, with dotted green line representing a cell from a primary tip-split event and dash-dotted red line and blue (dark gray) line representing cells formed during secondary and tertiary splitting, respectively. The direction of front propagation is shown by the arrow.

evolution in the two cases examined in this section can be traced to the difference in system width. Initially both systems develop four main branches with approximate separation corresponding to a wave mode close to $k = k_{\max} = 0.15\pi/\delta_c$. The larger system then transitions to establishing eight branches with a wavenumber approximately $k_8 = 0.1\pi/\delta_c$, while the smaller system fails to do so due to system size effects that hinder the growth and further tip splitting of smaller branches.

Kilker et al. [87] recently published a paper on cellular instabilities in premixed flames with stepwise ignition temperature kinetics and first-order reaction $n = 1$. In their work, they derive an analytical equation governing the dynamics of a two-dimensional interface in strongly non-linear regime of combustion by employing asymptotic analysis. Their numerical results indicate that their interface equation can only predict the correct behaviour of the combustion interface if the values of the Lewis number are slightly below its critical values. However, when the deviation of Lewis number from its critical value increases, the analytical equation may only approximate the solution of the original problem. The main reason for this is that for a range of small Lewis number values, the interface intersects itself and overhangs appear in the morphology, which essentially violates the assumptions based on which asymptotic analysis is performed. Consequently, the complete dynamic behaviour of the system, as shown in Fig. (3–13,3–14), can only be captured by solving the coupled partial differential equations of continuum master model Eqs. (2.22) and (2.24).

3.2 Adding Thermal Dissipation to the Master Model Equations

In this subsection, we will modify the master model to include heat dissipation in the form of linear newtonian cooling term $-\Upsilon(T - T_o)$, where Υ is the coefficient that measures the intensity of heat loss [J/m³sK]. This assumes cooling into the third dimension for in a 2D simulation. In dimensionless units, the set of Eqs. (2.22) become modified to

$$\begin{cases} \frac{\partial \theta}{\partial t} = \nabla^2 T + W - \Gamma \theta \\ \frac{\partial \phi_{ox}}{\partial t} = \frac{1}{Le} \nabla^2 \phi_{ox} - W \end{cases} \quad (3.11)$$

In Eq. (3.11), the dimension-less heat dissipation rate is given by $\Gamma = \Upsilon \tau / \rho c_p$ where τ is the characteristic time of the problem. To find the steady state solution of these equations, we transform them to a co-moving reference frame $\xi = x - ut$, where the interface is at $\xi = 0$ and u is the steady-state velocity of a planar front. We carry out our analysis in units that assume the steady-state velocity u is unity. However, the assumption made only simplifies the derivation and does not affect the end result. We solve the above equations on either side of the interface and apply a set of continuity conditions for the fields and their derivatives across the interface defined at $\xi = 0$. These are given by

$$\begin{aligned} [\theta] &= 0 & [\phi_{ox}] &= 0 \\ \left[\frac{d\theta}{d\xi} \right] &= 0 & \left[\frac{d\phi_{ox}}{d\xi} \right] &= 0, \end{aligned} \quad (3.12)$$

where $[\cdot]$ denotes a jump across the interface. The modified version of Eqs. (3.1) for the far-field values in the presence of heat dissipation are given by

$$\begin{aligned}\theta(+\infty, y) &= 0 & \theta(-\infty, y) &= 0 \\ \phi_{\text{ox}}(+\infty, y) &= 1 & \phi_{\text{ox}}(-\infty, y) &= 0\end{aligned}\quad (3.13)$$

The steady-state solutions of temperature and concentration fields in Eqs. (3.11-3.12-3.13) are derived in Appendix C. Assuming $u = 1$, the steady state dimensionless temperature is given by

$$\theta^{\text{ss}} = \begin{cases} \theta_{\text{ign}} \exp\left(\frac{(\nu - 1)}{2}\xi\right) + \frac{2\theta_{\text{ign}}\nu(1 - \theta_{\text{ign}}\nu)}{2\theta_{\text{ign}}\nu^2 - \nu + 1} \times \\ \left[\exp\left(\frac{(\nu - 1)\xi}{2}\right) - \exp\left(\frac{\theta_{\text{ign}}\nu(1 + \nu)}{2(1 - \theta_{\text{ign}}\nu)}\xi\right) \right] & \xi \leq 0 \\ \theta_{\text{ign}} \exp\left(\frac{-(1 + \nu)\xi}{2}\right) & \xi > 0, \end{cases} \quad (3.14)$$

while the solution for concentration becomes

$$\phi_{\text{ox}}^{\text{ss}} = \begin{cases} \frac{1}{1 + \frac{\theta_{\text{ign}}\nu(1 + \nu)}{2\text{Le}(1 - \theta_{\text{ign}}\nu)}} \exp\left(\frac{\theta_{\text{ign}}\nu(1 + \nu)}{2(1 - \theta_{\text{ign}}\nu)}\xi\right) & \xi \leq 0 \\ \frac{-1}{1 + \frac{\theta_{\text{ign}}\nu(1 + \nu)}{2\text{Le}(1 - \theta_{\text{ign}}\nu)}} \exp(-\text{Le}\xi) + 1.0 & \xi > 0, \end{cases} \quad (3.15)$$

where the dimension-less parameter $\nu = \sqrt{1 + 4\Gamma}$ has been defined. Typical profiles of temperature and concentration for model parameters MM ($n = 1$; $\text{Le} = 0.75$; $\theta_{\text{ign}} = 0.75$; $\Gamma = 0.01$) are plotted in figure (3-15). To contrast the case with dissipation from the case of an

adiabatic combustion front, the corresponding temperature and concentration profiles for the same model parameters with ($\Gamma = 0$), are also displayed in Fig. (3–15).

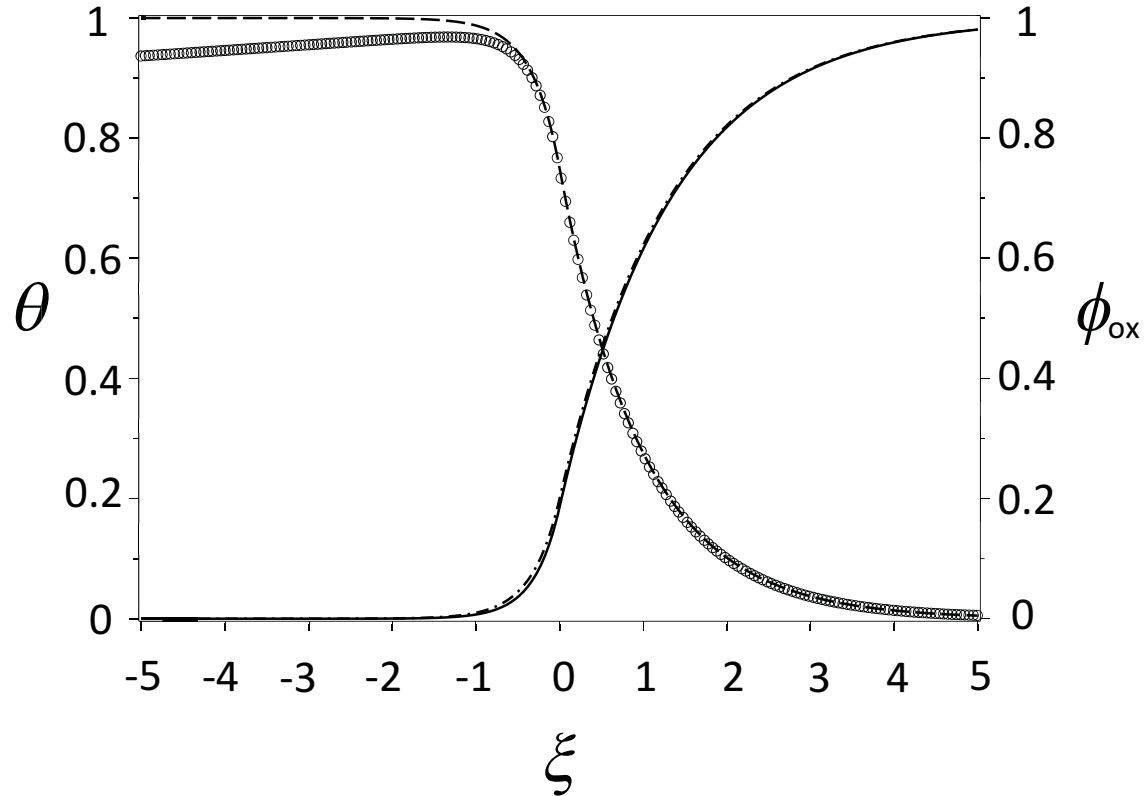


Figure 3–15: One dimensional analytical solutions for the dissipative model $MM(n = 1; Le = 0.75; \theta_{ign} = 0.75, \Gamma = 0.01)$: $\circ\circ\circ$ temperature, — concentration, and for an adiabatic model $MM(n = 1; Le = 0.75; \theta_{ign} = 0.75; \Gamma = 0)$: - - - temperature, -.-.- concentration.

The above results show that while heat dissipation has an appreciable effect on the steady-state temperature of the combustion front, specifically in the combustion and product zones, the concentration of oxidizer profile seems to remain nearly unchanged under non-adiabatic condition (Fig. 3–15). As a consequence, the heat dissipation effects are expected to affect thermo-diffusive instabilities, and may alter or dominate the linear regime of dynamics and the resulting cellular patterns.

It is instructive to investigate how heat-dissipation influences the cellular patterns in combustion front. The remainder of this chapter examines the linear stability regime of the combustion front modelled by Eqs. (3.14-3.15). We study the liner regime of the system under non-adiabatic conditions by using analytical and numerical linear perturbation analysis as we did previously for the adiabatic case. We do so using an approach similar to that of [22]. To our knowledge, this is the first time this analysis has been derived for a non-adiabatic 2D combustion front assuming the stepwise ignition kinetics.

3.2.1 Derivation of linear dispersion-relation with thermal dissipation

Here, we only derive the dispersion relation for first-order kinetics (denoted by $n = 1$). Derivation for zero-order case can be done analogously. In what follows, we only present the main results and the detailed derivations are postponed to Appendix C.

To find the linear response of a system to small spatial disturbances, both steady-state solutions of fields in Eqs. (3.14-3.15) as well as the 1D combustion interface are perturbed as follows

$$\begin{aligned}\theta(\xi, y, t) &= \theta^{\text{ss}}(\xi) + \theta'(\xi, y, t) \\ \phi_{\text{ox}}(\xi, y, t) &= \phi_{\text{ox}}^{\text{ss}}(\xi) + \phi'(\xi, y, t) \\ F(y, t) &= (u = 1)t + f'(y, t),\end{aligned}\tag{3.16}$$

where perturbations are given by,

$$\begin{aligned}\theta'(\xi, y, t) &= \hat{\theta}(\xi) \exp(\omega t + iky) \\ \phi'(\xi, y, t) &= \hat{\phi}(\xi) \exp(\omega t + iky) \\ f'(y, t) &= \hat{f} \exp(\omega t + iky).\end{aligned}\tag{3.17}$$

In this notation, the hat parameter is the amplitudes of a perturbation, k , and ω its normal wave-number and amplification, respectively. The two-dimensional interface $F(y, t)$ in Eqs. (3.16), is defined from the ignition interface condition $\theta(F(y, t), y, t) = \theta_{\text{ign}}$, which in the co-moving reference frame, with $u = 1$, gives $F(y, t) = (u = 1)t + \xi$.

Applying the boundary conditions in Eq. (3.12) to the perturbation fields in Eq. (3.16) and their derivatives gives the following conditions at $\xi = 0$,

$$\left\{ \begin{array}{l} \theta'(\xi = 0^+) = \theta'(\xi = 0^-) = \frac{f' \theta_i(1 + \nu)}{2} \\ \\ \phi'(\xi = 0^+) = \phi'(\xi = 0^-) = \frac{-f' \text{Le}(\theta_{\text{ign}} \nu(1 + \nu))}{\theta_{\text{ign}} \nu(1 + \nu) + 2 \text{Le}(1 - \theta_{\text{ign}})} \\ \\ \frac{\partial \theta'(0^+)}{\partial \xi} - \frac{\partial \theta'(0^-)}{\partial \xi} = \frac{f' \theta_{\text{ign}}(1 + \nu) \nu}{2(\theta_{\text{ign}} \nu - 1)} \\ \\ \frac{\partial \phi'(0^+)}{\partial \xi} - \frac{\partial \phi'(0^-)}{\partial \xi} = f' G(\nu, \text{Le}), \end{array} \right. \tag{3.18}$$

where $G(\nu, \text{Le})$ is defined by

$$G(\nu, \text{Le}) = \frac{\text{Le}^2}{1 + \frac{2\text{Le}(1 - \theta_{\text{ign}})}{\theta_{\text{ign}}\nu(1 + \nu)}} + \frac{\theta_{\text{ign}}^2 (\nu(1 + \nu))^2}{(-2\theta_{\text{ign}}\nu + 2)^2 \left(1 + \frac{\theta_{\text{ign}}\nu(1 + \nu)}{\text{Le}(1 - \theta_{\text{ign}}\nu)}\right)}, \quad (3.19)$$

and where it is recalled that $\nu = \sqrt{1 + 4\Gamma}$.

We next insert Eqs. (3.16) into Eqs. (3.11) (with $u = 1$), and keep only linear order in the perturbations while cancelling terms of steady-state solutions. This leads to a set of partial differential equations (PDEs) for the perturbations emerges (see Appendix C). Substituting Eqs. (3.17) into these PDEs, and solving for the perturbations gives

$$\theta'(\xi) = \begin{cases} n \exp(p_+ \xi) + \frac{mA}{(\omega + k^2 + \Gamma) - l_+^2 - l_+} \exp(l_+ \xi) & \xi \leq 0 \\ a \exp(p_- \xi) & \xi > 0, \end{cases} \quad (3.20)$$

for the temperature perturbation, and

$$\phi'(\xi) = \begin{cases} m \exp(l_+ \xi) & \xi \leq 0 \\ b \exp(q_- \xi) & \xi > 0, \end{cases} \quad (3.21)$$

for concentration perturbation, where a, b, m, n are arbitrary constants. By substituting Eqs. (3.20-3.21) into Eqs. (3.18), we arrive at the following linear algebraic equations for

free constants,

$$\left\{ \begin{array}{l} a - \frac{f' \theta_{\text{ign}}}{2} (1 + \nu) = 0 \\ n + \frac{A m}{(\omega + k^2 + \Gamma) - l_+^2 - l_+} - \frac{f' \theta_{\text{ign}} (1 + \nu)}{2} = 0 \\ a p_- - \left(n p_+ + \frac{A m l_+}{(\omega + k^2 + \Gamma) - l_+^2 - l_+} \right) - \frac{f' \theta_{\text{ign}} (1 + \nu) \nu}{2(\theta_{\text{ign}} \nu - 1)} = 0 \\ m = b \\ (b q_- - m l_+) - f' G(\nu, \text{Le}) = 0, \end{array} \right. \quad (3.22)$$

where subsequent parameters have been defined,

$$\begin{aligned} A &= \frac{\nu(\nu + 1)\theta_{\text{ign}}}{2(1 - \theta_{\text{ign}} \nu)} \left(1 + \frac{\theta_{\text{ign}} \nu (1 + \nu)}{2 \text{Le} (1 - \theta_i \nu)} \right), \\ q_{\pm} &= \frac{1}{2} \left[-\text{Le} \pm \sqrt{\text{Le}^2 + 4(k^2 + \text{Le} \omega)} \right], \\ l_{\pm} &= \frac{1}{2} \left[-\text{Le} \pm \sqrt{\text{Le}^2 + 4(k^2 + \text{Le} \omega + A \text{Le})} \right], \\ p_{\pm} &= \frac{1}{2} \left[-1 \pm \sqrt{1 + 4(\omega + k^2 + \Gamma)} \right], \end{aligned} \quad (3.23)$$

To ensure the non-trivial solution for this system of equations, the determinant of coefficient of homogenous equations Eqs. (3.22) is set to zero, and after doing some algebra following dispersion relation is derived (see Appendix C)

$$\begin{aligned} \Delta(\omega, k, \text{Le}, \Gamma) &= -G(\nu, \text{Le}) A(p - l) \\ &\quad + (q - l) \left[\frac{\theta_{\text{ig}}(1 + \nu)}{2} \left(\frac{\nu}{\nu \theta_{\text{ig}} - 1} + (1 - 2p) \right) \dots \right. \\ &\quad \left. \dots \times \left((1 - \text{Le})(\omega - l) - A \text{Le} + \Gamma \right) \right] = 0, \end{aligned} \quad (3.24)$$

where p , l , and q are equal to p_+ , l_+ , and q_- in Eqs. (3.19). Equation (3.24) reduces to dispersion relation Eq. (23) of [22] for first-order adiabatic combustion front in the adiabatic limit (i.e. $\Gamma = 0$). The analytical dispersion relation in Eq. (3.24) for model parameters MM($n = 1$; $Le = 0.6$; $\theta_{ign} = 0.75$; $\Gamma = 0.01$) is plotted in Fig. (3–16) with a solid blue line.

3.2.2 Numerical linear dispersion-relation with thermal dissipation

In order to verify the analytical dispersion relation Eq. (3.24), we apply the same numerical technique as introduced in 3.1.1 for an adiabatic combustion front. This analysis is only performed for first-order kinetics ($n = 1$), but the discussion presented in this section can also be applied to the zero-order case. The numerical analysis is conducted for the set of model parameters MM($n = 1$; $Le = 0.6$; $\theta_{ign} = 0.75$; $\Gamma = 0.01$). The resulting numerical dispersion data along with the corresponding analytical solution Eq. (3.24) are presented in Fig. (3–16). For comparison, the analytical results for the adiabatic cases MM($n = 1$; $Le = 0.6$; $\theta_{ign} = 0.75$) and MM($n = 1$; $Le = 0.56$; $\theta_{ign} = 0.75$) are also plotted in the Fig. (3–16).

The analytical results in Figure (3–16) for the case of dissipation (solid blue line) shows that growth rate of very low k modes, in contrast to the adiabatic cases (solid red line and dashed lines), do not tend to zero and it becomes plateau instead. This implies that under non-adiabatic conditions, a planar interface is unstable to oscillations. Similar results were also obtained by Joulin et al. [80] in their study of non-adiabatic cellular flames, where they study the dynamics of cellular front in the kinetic-limited regime of combustion and in the context of thermo-diffusive instabilities.

Figure (3–16) also shows numerical results for the dissipative system $\text{MM}(n = 1; \text{Le} = 0.6; \theta_{\text{ign}} = 0.75; \Gamma = 0.01)$ (marked by ●). The numerical data converge onto the analytical dissipative solution at higher k modes, but deviate for low k , where their growth rate is governed more closely by the growth dynamics of an effective adiabatic system (dashed line –discussed below). It is plausible that this issue is caused by the finite-size of the numerical domain, which does not support the growth of wavelengths longer than the system size. Moreover, because the relatively small dissipation does not have time to influence the decay rate of the system-sized modes, these effectively follow adiabatic decay rates.

Both the range and growth rate of linearly unstable k modes is larger with dissipation than the adiabatic case, and in the former case the fastest growing mode shifts toward the higher k modes. Inspection of Fig. 3–1(a) thus suggests that the high- k behaviour of the dispersion relation with dissipation ought to resemble that of an adiabatic system with a *lower* Lewis number. This is seen in Fig. (3–16) where the plot of the dispersion relation for the adiabatic case $\text{MM}(n = 1; \text{Le} = 0.56; \theta_{\text{ign}} = 0.75)$ (dashed line in Fig. 3–16) is shown to match the analytic case with dissipation fairly well for $k >\sim 0.2$. This effective adiabatic case matches the numerical data with dissipation over all k examined, consistent with the discussion of the previous paragraph. This analysis suggests that, for high k modes, introducing heat dissipation has a similar effect as decreasing Lewis number on linear growth rates of these modes.

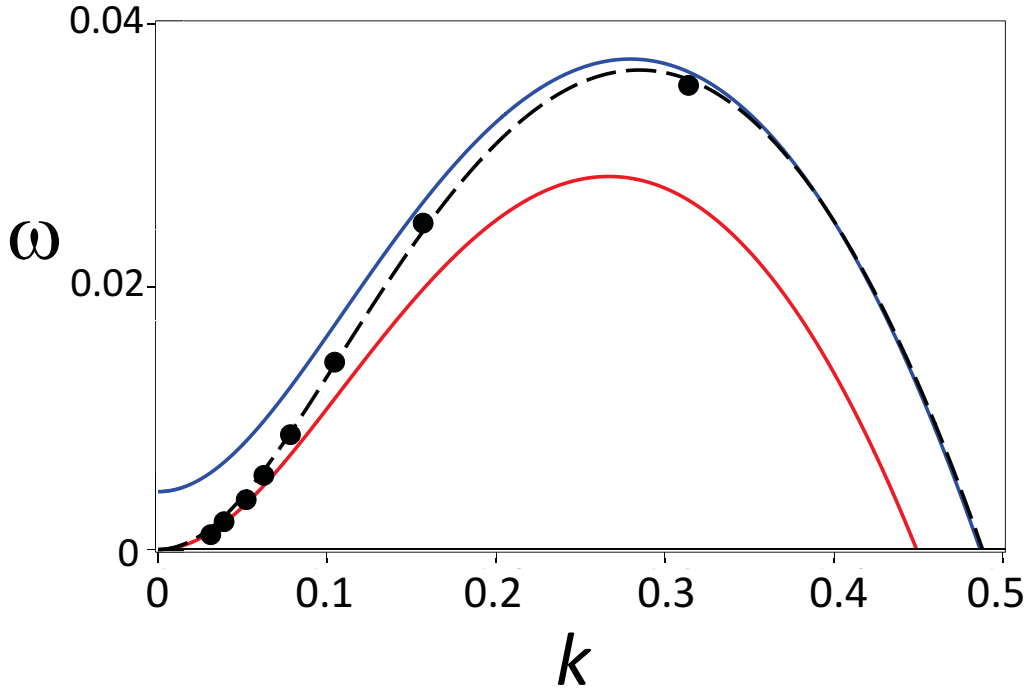


Figure 3–16: Dispersion relation for $\text{MM}(n = 1; \text{Le} = 0.6; \theta_{\text{ign}} = 0.75, \Gamma = 0.01)$: — analytical, ● numerical; $\text{MM}(n = 1; \text{Le} = 0.6; \theta_{\text{ign}} = 0.75, \Gamma = 0)$: — analytical; $\text{MM}(n = 1; \text{Le} = 0.56; \theta_{\text{ign}} = 0.75, \Gamma = 0)$: - - - analytical.

3.2.3 Summary

To summarize, we found that the combustion front develops a cellular morphology below a critical value of the Lewis number. The linear stability of the cellular fronts was investigated numerically and found to agree very well with the dispersion relation predicted analytically by Brailovsky et al. We addressed the influence of the size of the computational domain and Lewis number on linear mode selection. Our results indicate that lowering the value of the Lewis number broadens the range of instability modes that can be triggered and increases the growth rates of the most unstable k modes.

For values of the Lewis number Le close to unity, the transition from the linear to the non-linear (i.e. late-time) regime becomes prolonged and is characterized by very shallow amplitude cell structures. We identified this regime as a “quasi-linear” regime in the sense that the long time behaviour of the front can be qualitatively explained in terms of the growth modes and growth rates available to the linear system. The dynamics of this regime were explored and discussed. For lower Lewis number values ($\text{Le} < 0.4$) the transition to the fully non-linear regime occurs early in the evolution of the front. Non-linear effects dominate the dynamics, characterized by initially large amplitude cellular structures that develop into complex morphologies with overhangs. We explored this non-linear regime, and the influence of finite size effects on the late-time dynamics of tip splitting and merging that dominates front morphology, emphasizing parallels with isotropic dendritic microstructures in solidification phenomena.

The dendritic patterns simulated in this work are similar to those observed in experiments of flame propagation over a bed of nano-aluminum powder burning with a counter-flowing oxidizer [104], which are also obtained in the limit of low-Lewis numbers (Fig. 3–13 and Fig. 3–14). Such patterns are analogous in their physics to those observed in directional solidification [92]. Similar patterns have been observed in simulations of slow combustion in the absence of convection effects and by assuming simple threshold mechanism for ignition [33]. Conti et al. discussed these patterns as a result of competition between the stabilizing effect of heat field (thermal diffusion length along with ignition threshold) and the destabilizing effect of oxygen field (which tends to increase the surface area) These competing forces are analogues to heat diffusion and surface tension in solidification [92]. Other examples of this parallel include the analogy between Saffman-Taylor combustion

finger and dendrite solidification fingers [142]. Dendritic patterns are paradigms of pattern formation when there is a competition between diffusion-limited transport and a stabilizing force at the interface. To our knowledge our simulations are the first to simulate such patterns in combustion fronts at experimentally relevant domain sizes and parameters.

Cellular instabilities in these experiments are observed in quasi-two-dimensional geometry where three-dimensional buoyancy is suppressed. Furthermore, this configuration intensifies the destabilizing effect of reactant transport, which plays the same role as in the thermal-diffusion instability. It is noteworthy that the three-dimensional experiments of cellular and fingering instabilities of solid fuel combustion that are conducted in microgravity conditions, exhibit analogous patterns [81, 83]. The similarity of the results demonstrates the equivalence of quasi 2-D configuration and microgravity in counteracting the gravitational effects.

Our examination of combustion fronts in under adiabatic condition will continue in the next chapter, which will address the front dynamics considering discrete fuel particles rather than a continuum fuel source, as well as stochasticity.

The second part of this chapter studied the linear regime of planar combustion front under conditions of heat dissipation. Our results show that high- k modes growing in the presence of heat dissipation can be effectively described by the amplification rate of the same modes growing under adiabatic conditions. For small k modes, however, different behaviour is observed between our numerical and analytical results when heat dissipation is considered. Our analytical result indicates that the dispersion relation goes to a constant as $k \rightarrow 0$, while our numerical results reveal that the growth of low- k modes vanishes as

$k \rightarrow 0$. It is plausible that this is an artifact of finite size effects used in our simulations, which suppresses the growth of low- k modes.

CHAPTER 4

Cellular instabilities of combustion fronts in random discrete media

In this chapter, we study pattern forming and dynamics of propagating combustion fronts in random heterogenous media in the framework of thermo-diffusive instabilities and by using the master model of combustion in the discrete limit. The heterogenous combustion system comes closest to a realistic realization of experimental combustion flames in a suspension of metal particles, which is the focus of this study [81, 60, 171]. However, the results and discussion for this specific system also can be applied to a more general case of interface propagation in heterogeneous excitable media which has a vast range of applications from biology to materials science. For example in biology, the dynamics of calcium waves released from spatially random distributed sources, has been studied using Fire-Diffuse-Fire (FDF) model [140]. In this model, the calcium waves, assuming that the local field (action potential) is above a definite threshold, release from collective discrete sources. In this case the dynamics of the system can be described by diffusive equation with these spatially discrete sources. Similar phenomena are observed in the combustion of particulate fuel in hot oxidizer gas, where the action potential is replaced by the local temperature of particles, and the threshold criteria is represented by the ignition temperature of solid metal fuels.

Here, we examine the role of the heterogeneity of a medium (which enters the model through spatially discrete fuel particles) on the dynamic behaviour of a moving front, and the origin of its thermo-diffusive instabilities. We will focus on cellular patterns.

It is expected that the stochasticity of the combustion process, in general, can expedite the pattern formation, or even alter the morphology of a resulting pattern. To this end we use discrete limit of master model (Eqs. (2.22-2.25)) to describe the dynamics of a moving front. In contrast to the continuum limit where the discreteness of fuel particles is introduced implicitly through effective heat/mass transport coefficients and reaction rate (Eqs. 2.17-2.21), in the current case it appears explicitly in the source term W (Eq. 2.25).

Before we proceed further, at this point we shall once again specify the conditions of the combustion system that distinguish when the continuum-limit or discrete-limit approach must be used.

Comparing the combustion model in the discrete-limit and continuum-limit

Equations of both continuum and discrete limits are derived based on the assumption of medium heterogeneity. In the former case we use the effective-medium approach in which we assume the heterogeneity of a medium, hereafter denoted by average inter-particle spacing l_p , is significantly smaller than the thermal length of a flame δ_c . In general, a continuum-limit approach is valid in the following situations, and discrete modelling should be employed otherwise.

- When solid phase concentration is above its stoichiometric value, mixture is called fuel-rich and inter-particle spacing becomes significantly smaller than thermal length of the flame front. For instance in experiments of fuel-rich aluminium particle suspension, the characteristic thermal length of the flame front $\delta_c = \mathcal{O}(10^{-4})[\text{m}]$, is

almost 10 times larger than the average particle size $r_p \sim 10\mu m$ and thus the heterogeneity of a medium can be ignored

- Equivalently, increasing the thermal conductivity of a medium, can effectively lessen the impact of heterogeneity of a medium on dynamics of a moving front. One possible scenario for this case, for instance, is when the combustible mixture contains inert gas with high thermal conductivity. Besides the effective conductivity of a medium (mixture of oxidant, inert gas, and solid particles) depends on, and increases by increasing the initial concentration of solid phase, thereby enlarges the thermal length of the flame front

4.1 Analysis of cellular flame front instability- Adiabatic random discrete case

Our numerical investigations of cellular instabilities of a combustion front in the continuum limit, in chapter 3, showed that a planar front below a critical Lewis number (Le_c) develops cellular patterns. This value of Lewis number corresponds to the boundary that separates the stable from cellular unstable regime and in the continuum limit is given by Eq. (3.8) for the first-order kinetics $n = 1$, and by Eq. (3.9) for the zero-order kinetics $n = 0$. These results revealed the effect of Lewis number, initial condition, and computational domain size on “early”, “intermediate”, and “late” stages of dynamics of a cellular front.

In this chapter we examine the impacts of discrete, randomly distributed media on combustion. We limit our study only to the combustion system with zero-order kinetics.

This type of kinetics is most consistent with experiments of combustion flames in suspension of particles, where concentration of solid fuel is below its stoichiometric value, and there is an ample amount of oxidizer. The results of this chapter will be presented as follows: We first analyze the linear regime of cellular instabilities of a combustion front propagating in a heterogenous random media using numerical stability analysis. The resulting numerical dispersion relation then will be compared with the analytical solution of Brailovsky et al. [22] for the continuum combustion limit (Eq. 3.4 for $n = 0$), and their differences will be discussed in the context of the heterogeneity of the random medium. Specifically, we derive *effective* model parameters that describe combustion in the discrete random fuel particle limit as the combustion of an effective continuum. This process is aided by the effective-model analysis shown in appendix B. Following the stability analysis, we examine the role of stochastic particle distribution (including inter-particle spacing and particle size distribution) and the effect of Lewis number on the long-time non-linear dynamics of cellular fronts.

To probe the dynamics of cellular patterns in 2D computational domains, we modified the numerical algorithm established for continuum-limit combustion fronts (see 3.1.1), to include spatially random particles. In addition, we develop numerical algorithms to generate initial configurations of randomly distributed particles within a computational domain. In the following section we will give a brief review of these algorithms. A more complete version of these numerical algorithms along with the computational codes can be found in (https://bitbucket.org/hosseinphy/phd_files).

4.1.1 Numerical method to study cellular flame front instability in random media

We use the same C++ finite-difference AMR-based code that we implemented to study a combustion front in the continuum limit (see 3.1.1) with minor adjustments to account for randomness in the fuel source on the adaptive mesh. The threshold for the local refinement of the computational mesh is increased, while the frequency of the adaption is increased to guarantee the accuracy of our calculations. The purpose of this modification is to accurately capture fluctuations in local fields –due to the randomness of the combustion medium– in the interface and pre-heat zones, while still allowing enough of the far field to be adapted to a coarser mesh in order to allow significant speed-up of the numerical calculation. The smallest AMR grid size, was set to $dx = 0.04$ in units of characteristic length-scale of heterogeneity of the medium (i.e. inter-particle spacing d , when particles are placed on a regular square lattice). The time step was determined accordingly, using the numerical stability criteria for the two dimensional diffusion equation. Particles are spatially resolved in each adaption cycle with the highest level of refinement. A simulation is conducted within a two dimensional rectangle (L_x, L_y) where the spatial coordinates x and y were parallel and normal to the principal direction of flame propagation, respectively. In our simulations far-field boundary conditions, given by Eqs. (3.1), are applied in the principle direction of flame propagation. To model an adiabatic combustion chamber, the no-flux conditions in the form presented by Eqs. (3.2), are imposed on the lateral boundaries of the simulation box.

4.1.1.1 Numerical representation of discrete particle

To represent the spatial extent of particles in finite-difference scheme we need to discretized a particle. In the two-dimensional simulations reported here, particles are randomly placed on a uniform square lattice so that the volume (area in 2D) occupied by each particle indexed by i is given by,

$$V_p = \sum_{j=1}^m H(r_p - |\vec{x}_i - \vec{x}_j|) \Delta x^2, \quad (4.1)$$

where $\vec{x}_i = (x_i, y_i)$, and $r_p = m \Delta x$ specify the centre and radius of a particle, respectively, where Δx is the size of the numerical grid spacing at the highest refinement level (i.e. dx), and j indexes the elements inside a particle. The source term of Eq. (2.25) for zero-order kinetics ($n = 0$), becomes specialized to the situation here by setting $g(|\vec{x} - \vec{x}_i| - r_p) = (1/V_p) H(r_p - |\vec{x} - \vec{x}_i|)$. In a two-dimensional finite difference scheme, the dimension-less inverse combustion time is $A = l_p^2/(t_R^* \alpha)$, where l_p , t_R^* , and α are average inter-particle spacing, physical combustion time, and thermal diffusivity of the medium (see appendix A). This method of discretization of particles in finite-difference methods is also suggested in other studies [173].

4.1.1.2 Sampling random dispersion of fuel particles

In study of combustion front propagation through a heterogenous random media, dynamic behaviour of a front can be marginally affected or dominated by the random nature of the combustible media. The dynamics of a moving interface in such a stochastic process thus need to be treated by statistical analysis methods, performing statistical averaging over many independent samples of a system with identical particles. Each sample is a

realization of a possible configuration of randomly distributed particles in space, and identified by its *structural* parameters including, the ensemble-averaged inter-particle spacing or equivalently average number density of particle centres, as well as particle-size distribution. Through these indices, one can subsume the effect of microscopic fluctuations, and describe the dynamics in terms of macroscopically measurable quantities.

In developing the numerical algorithm to generate a 2D sample of dispersed particles following assumption have been made: (1) Particles are impenetrable and are represented by 2D hard disks¹ with diameter D_p . The heat conductivity of particle is much higher than the gaseous phase. This will be used later when we calculate the effective Lewis number. Also the temperature within a solid phase is assumed to be uniform. (2) Fuel particles, once generated, become locked to their positions. This is consistent with our earlier assumption that the diffusion of solid fuel is negligible. We also assume particles can be distributed either “uniformly” or in a “non-uniform” fashion, where in the former case the sample is statistically isotropic² and homogeneous² while the non-uniform sample is neither isotropic nor homogenous in general.

To generate a *uniform* fuel particle sample we used the numerical algorithm proposed by Torquato [175]. In this method particles are generated and initially placed at positions on a uniform square lattice in a computational domain, where the centre of particle

¹ This assumption is introduced to ensure that there is no overlap between particles.

² A medium is said to be statistically isotopic (homogenous) if the joint probability describing the stochastic process is rotationally (translationally) invariant. Statistical homogenous sample the n -point probability function depends not on the absolute position but on the relative displacement.

i is given by the Cartesian coordinates (x_i, y_i) . The particles are then forced to move to new positions, which are generated by two random numbers X and Y . These moves are accepted as long as there is no overlap between particles, and refused otherwise. This procedure continues repeatedly until the ratio of accepted moves to the total number of moves approaches its limit 0.5 and does not change in time. As a result a uniform distribution of particles will be achieved.

We use a different algorithm to produce a *non-uniform* fuel sample. In this method particles are randomly and sequentially placed inside an empty 2D box. If a particle can be placed inside a box without overlapping other particles, it remains fixed. If it overlaps other particles, another attempt has to be made to find a new location. This process repeats until no more additions are allowed. In this method, in contrast to the “uniform” sample, no-flux boundary conditions for particles are employed. One drawback of this method is that the saturation, in principle, may occur only after an infinite amount of time. Nevertheless, this algorithm is designed to mimic particle distributions in the actual closed chamber [175].

We re-scale length in our equations Eqs. (2.22-2.25) using the length-scale of the *regular* heterogenous medium, whose characteristic length scale is inter-particle distance denoted by d . The thermal diffusion time associated with this length $\tau = d^2/\alpha$ is used to rescale time. The number density N_s is defined as the number of particle centres N in each domain within an area $d \times d$, and $\Phi_s = N_s \pi D_p^2 / 4$ represents the area fraction of the domain occupied by metal particles. The average inter-particle spacing in a random medium, l_p , is calculated in our numerics by statistical averaging of the two-particle probability density function, and will be given in units of d .

A sample random distribution of fuel particles is generated numerically by the algorithm we use by setting the surface area fraction (volume fraction in 3D) to Φ_s , and the number density of particles N_s to a desired values. The diameter of a particle D_p is then found from the definition of Φ_s above. The computational codes to generate uniform and non-uniform samples are available in (https://bitbucket.org/hosseinphy/phd_files). In this study we use RandomLib library to generate a uniformly distributed random numbers with double precision in $(0, 1)$. The source codes and examples of RandomLib can be found in <http://randomlib.sourceforge.net/html>.

It is instructive to obtain an estimation for the inter-particle spacing, d , in a regular discrete medium, relative to the characteristic length δ_c for the continuum limit. We assume the continuum limit of the heterogenous medium with identical particles is achieved when $\Phi_s = 1$, and corresponds to a maximum packing of particles. In this case, the continuum-limit inter-particle spacing is given by $d_c = D_p$ and thus the characteristic length of the system in the continuum limit (called the thermal length of a flame δ_c in chapter 3) in 2D can be written as $\delta_c = \sqrt{\pi N_c / 4} d_c$, where N_c is defined as the number of particle centres in each domain within an area $\delta_c \times \delta_c$. The ratio of inter-particle spacing in the discrete limit to that in the continuum limit, assuming particle size in both limits is same, can thus becomes $d = (\sqrt{N_c} / \sqrt{N \Phi_s}) \delta_c$. Using this relation, one can obtain the characteristic length of the heterogenous medium in terms of thermal length of a flame in the continuum limit.

4.1.2 Cellular combustion front in random media: Early-time regime

The early-time dynamics of a cellular combustion front in the continuum limit, was studied in Chapter 3 by examining the linear growth rate ω of a periodic perturbation of a planar interface with the wave number k . In the case of combustion front propagation in a random media on the hand, this approach of examining the linear regime may very likely become dominated by non-linear effects due to random nature of a combustible media. To investigate the early-time in this case, we devise a new approach, where we let a planar front to evolve in the presence of external perturbations (spatially random particles) and track the 1D ignition interface defined by $\theta(x, y, t) = \theta_{\text{ign}}$, in time. A simulation is initiated by a steady-state solution of the continuum combustion front. The amplification rate of the excited modes ω , can be calculated from the spectral power density of a 1D interface $x = f(y, t)$, using Fourier analysis. The growth rate for each excited mode amplitude A is defined by $\omega = (1/A)dA/dt$, and the regime is considered linear as long as the growth rate increases linearly in time.

This chapter examines uniformly random particle distributions with zero-order kinetics. As a working assumption, we continue to suppose that a combustion front in random media develops cellular morphologies below the critical Lewis number that is derived in the continuum limit (Eq. 3.9). However, it will be seen that this limit in a random medium, as we discuss later, shifts relative to its continuum value.

The analysis in this section is performed using a sample of uniformly random distributed particles. We choose this sample over the non-uniform one, because in this system a larger fraction area Φ_s of solid fuel particles can be achieved. In a non-uniform sample on the other hand, the area fraction cannot practically exceed $\Phi_s = 0.4$, which may completely

or partially alter the cellular regime that we wish to examine. Non-uniform samples will be used to study the late-time dynamics of cellular front propagating in non-homogenous random media in the next section.

The structural parameters of a uniform sample are set to ($\Phi_s = 0.7$, $N_s = 16$). The diameter of a particles, using $D_p = \sqrt{4\Phi_s/N_s\pi}$, is equal $D_p = 0.236 d$. To ensure the statistical homogeneity of the random medium, we let the particle deposition simulation –that precedes the combustion simulation– run long enough that the state of uniform distribution of particles is achieved. In our case this state was obtained after 5000 iterations while the configuration of the system was saved every 50 iteration. In this homogenous state, since the two-particle correlation function only depends on the relative distance of particles, one can obtain the inter-particle spacing from the ensemble-averaged two-particle probability density function (for more details see chapter 3 and chapter 12 in [175]). The value of inter-particle spacing in random distribution of particles, for the structural parameters ($\Phi_s = 0.7$; $N_s = 16$), is $l_p \sim 0.3 d$.

The numerical simulation of a combustion front propagation in this random media was carried out using model parameters MM($n = 0$; $Le = 0.3$; $\theta_{ign} = 0.75$) within a computational domain with lateral dimension of $L_y = 160 d$. Considering the stochastic nature of combustion process in random media and its possible effects on dynamics of a propagating front, and to obtain a better estimation of the linear dispersion relation, we perform ensemble averaging over sufficiently two stochastic realizations. The domain is also considered large enough to exploit self-averaging within each realization. A typical example of three time slices in the early-time evolution of a combustion front propagating in a random particle distribution in shown in Figure 4–1.

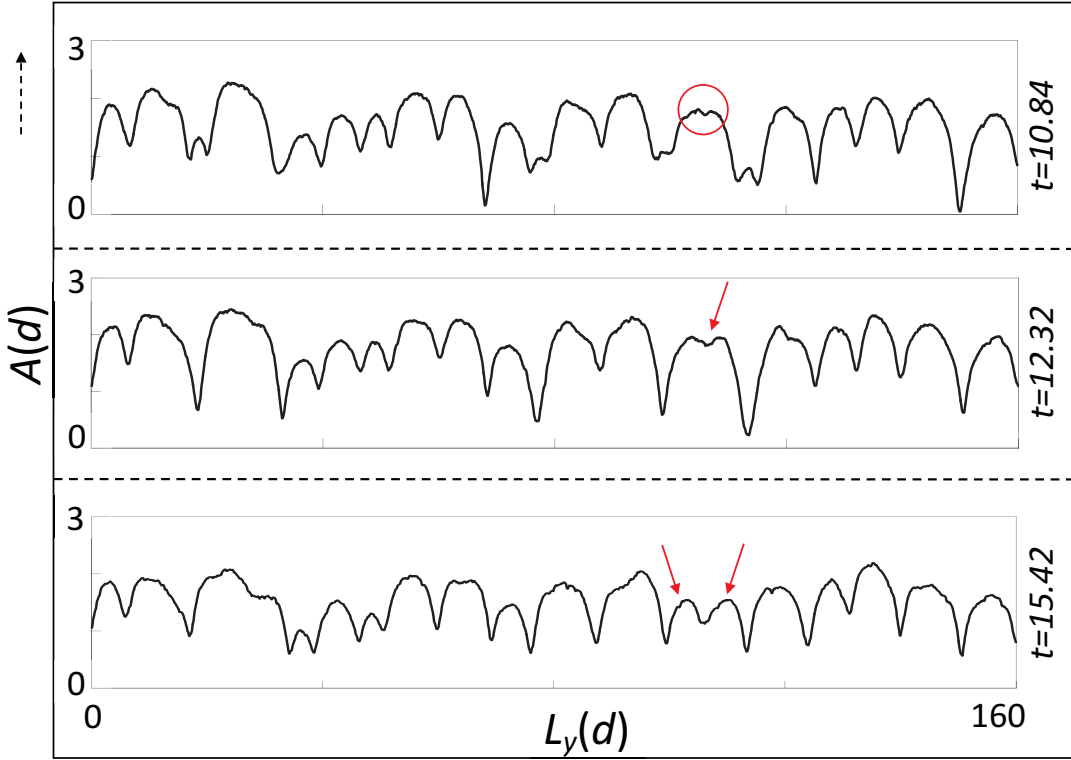


Figure 4–1: Amplitude of a combustion front propagating in a uniform random media with parameters $\Phi_s = 0.7$, $N_s = 16$ and for model parameters MM($n = 0$; $Le = 0.3$; $\theta_{ign} = 0.75$). In this figure, the process of tip-splitting which is followed by amplitude reduction is depicted in three subsequent instances. The two new tips in the third image are shown by the arrows. Time is in units of the characteristic time τ .

Figure 4–2 shows a early-time power spectrum of the interface in the front propagating in Figure 4–1. The power spectrum evolves to this form in a series of steps. Initially, the front evolution becomes perturbed by the heterogeneity, resulting in excitation of wide range of wave modes. The distribution of modes is initially centred around high k modes. As time proceeds, around $t \sim 2.5\tau$ the modes with much higher wave number are phased out and the lower k -modes start to interact with each other and the length-scale of the random media. This time frame is treated as a transient time. Around $t = 5\tau$ in simulation time, the amplitude of lower k modes start raising relatively fast, while high k modes fall

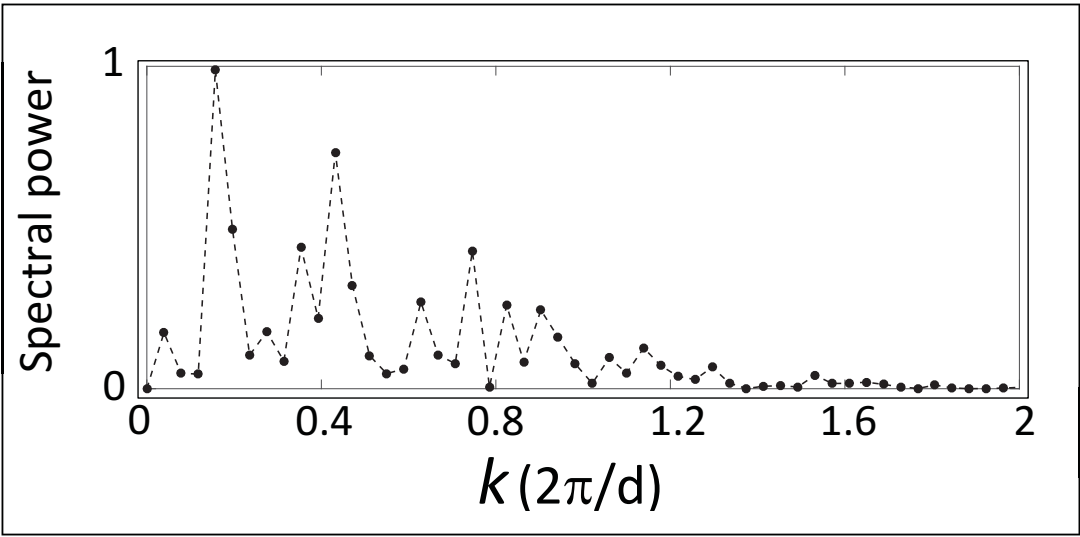


Figure 4–2: The normalized spectral power of 1D interface $x = f(y, t)$ at $t = 30\tau$ for model parameter MM($n = 0$; $\text{Le} = 0.3$; $\theta_{\text{ign}} = 0.75$) corresponding to a uniform random heterogenous medium with ($\Phi_s = 0.7$, $N_s = 16$).

quickly. As a result, the distribution of modes shifts towards lower k modes (i.e. $k = 0$) whose amplitudes are on average larger. The presence of high k modes with very small (but non zero) amplitudes signals random fluctuations in the particle distribution. These maintain approximately the same amplitude. The amplitude of low- k modes, however, continue to grow in time with almost the same amplification rate and become large compared to their initial values, starting very soon after the transient period (from $t = 5\tau$ to $t \sim 7\tau$).

The peaks of these aforementioned low- k modes in the interface spectrum correspond to an emerging statistically wider spacing in the principle direction of the front propagation(i.e. $+x$). This indicates that the dynamics of the front may dominated by nonlinear effects.These wider cells eventually become laterally unstable against the medium heterogeneity and the medium randomness. This leads to a tip-splitting event, such as the one

shown in Fig. (4–1). The figure shows that at $t = 10.84\tau$ the cell denoted by \circlearrowleft becomes slightly perturbed by a local disturbance. While growing, this cell become unstable at $t = 12.32\tau$ and eventually splits into two smaller cells at $t = 15.42\tau$. At this time the two new cells with initially small amplitudes (shown by the red arrows) likely grow with their amplification rates following the linear dispersion prediction of chapter 3, although only for a short time. These surviving cells further continue to grow and deepen, eventually becoming subjected to lateral instabilities, and another tip-splitting. During this process which repeats itself until end of our simulation ($t \sim 30\tau$), the growth rate of k modes after each tip-splitting event approximately follows the linear dispersion relation.

The amplification rate of modes that form in the interface of Fig. (4–1) just after $t \sim 12\tau$, are calculated and displayed in Fig.(4–3)³. In this figure the mean value of the growth rate ω for two realizations are depicted by (\blacksquare) where the blue error bars reflect the standard deviation from the two measurements. This large deviation from the main value is mainly due to the small number of the observations (two realizations in this case), and can be reduced further by using larger number of realizations. Also shown in the figure is the analytical solution of Brailovsky et al. [22] in the continuum-limit, for the same parameters as the random combustion front corresponding to the blue data. The numerical dispersion relation for the random-particle front has the same trend as the analytical solution, but it predicts comparatively higher values of ω for the specified k modes . This

³ The numerical method to calculate early-time growth rate of excited modes is revised from the approach reported here, where we looked at later times to extract growth. The details of this new approach will be presented in an upcoming publication.

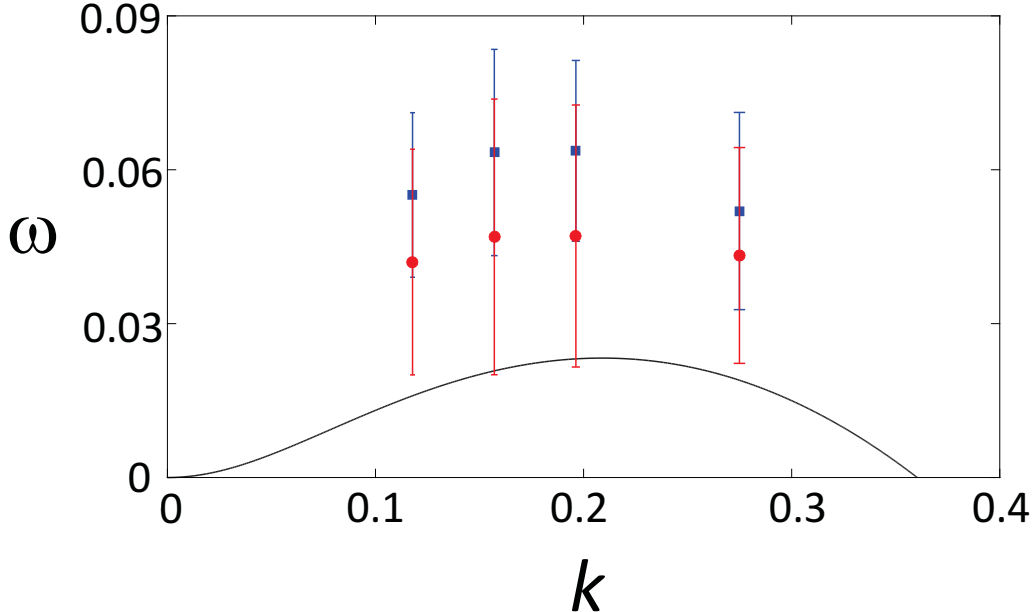


Figure 4–3: Dispersion relation for model parameters $\text{MM}(n = 0; \text{Le} = 0.3; \theta_{\text{ign}} = 0.75)$: — analytical solution in the continuum limit, ■ numerical results for a combustion front in the random medium; $\text{MM}(n = 0; \text{Le} = 0.45; \theta_{\text{ign}} = 0.75)$: ● numerical results for a combustion front in the random medium. The random medium is specified by $\Phi_s = 0.7, N_s = 16$. Error bars indicate the inaccuracy in calculating the growth rate ω for each case.

can be explained in the context of thermo-diffusive instabilities of a combustion front in random media. Specifically, in a heterogenous medium, the random nature of the reaction centres effectively acts to reduce the gradient of the local temperature (through local heat dissipation) thereby reducing the stabilizing effect of heat diffusion on instabilities. Therefore, the amplitude of linearly unstable modes tend to grow faster compared to that in the continuum-limit. The highest peak measured with Fourier analysis at $t = 15.42\tau$ corresponds to $k = 0.05\pi/d$. It is this mode that is most significant to the shape of the interface in Fig. (4–1).

The numerical results presented in this section, qualitatively resemble the early-time evolution of seaweed structures for range of low Lewis numbers in the continuum limit, for the same lateral dimension of the computational domain (see 3.1.4, Fig. 3–13–3–14). In particular, in both cases, the early stages of cellular front are dominated by non-linear effects that lead to non-symmetric deep cellular structures, such as tip-splitting and merging events. Moreover, their linear amplification rates of unstable cellular modes qualitatively corresponds to a continuum situation of higher Lewis number. The effect of Lewis number on linear regime of a combustion front was summarized in Fig. (3–3) in chapter 3. These qualitative similarities between cellular morphologies in random media and the early-time continuum cellular structure of low Lewis number suggests that perhaps the effect of random particle distribution on cellular pattern at high Lewis number values may be effectively mapped onto continuum patterns formed at lower Lewis numbers. We investigate this further in the next section.

4.1.3 Effect of Lewis number: Correspondence between pattern formation in discrete random and continuum-limit media

Our numerical results for linear dispersion relation which are presented in Fig.(4–3), show that the relative linear growth rate of unstable k modes in random media are larger compared to the analytical solution in the continuum limit. In addition, as we showed in chapter 3, the linear dispersion responds in a similar way, at least qualitatively, to lowering of the Lewis number (Fig. 3–1(a)). This raises the question whether there is a correspondence between Lewis number and randomness in the fuel particle distribution. In this section we aim to address this question by employing the effective medium version of

discrete-limit Eqs. (2.22) and (2.25). Using this method, effective parameters for combustion rate W , thermal diffusivity α , and oxidizer mass diffusivity D_{ox} (and their ratio $\text{Le} = \alpha/D_{\text{ox}}$) are obtained by volume-averaging over length-scale of interest which is significantly larger than the characteristic length of heterogenous medium, i.e. the average inter-particle spacing l_p .

We compute the effective Lewis number corresponding to a random distribution of particles, we use the following expression derived by Choy et al. [30]. They obtained the effective conductivity of a medium in which solid particles are assumed as 2D impenetrable disks with thermal conductivity κ_s that are dispersed in a gaseous phase with thermal conductivity κ_g as

$$\frac{\kappa^e}{\kappa_g} = f(\Phi_s) = 1 + 2\Phi_s + 2\Phi_s^2, \quad (4.2)$$

where κ^e denotes the effective conductivity of a medium (mixture of solid and gas phases) and the conductivity of gaseous phase is specified by κ_g . We should note that in deriving Eq. (4.2) the conductivity of solid inclusions is assumed to be much larger than that of the gaseous phase $\kappa_s \gg \kappa_g$. By using Eq. (4.2), and assuming that the mass diffusivity of oxidizer D_{ox} is constant and does not change in the presence of solid particles, the effective Lewis number Le^e can be written in the following form (appendix B)

$$\text{Le}^e = \frac{\alpha^e}{D_{\text{ox}}} = f(\Phi_s) \frac{\alpha_g}{D_{\text{ox}}}, \quad (4.3)$$

where $\alpha^e = \kappa^e/\rho c_p$ and $\alpha_g = \kappa_g/\rho c_p$ are the effective thermal diffusivity and thermal diffusivity of a medium without solid phase, respectively. The assumption of constant D_{ox} is only valid if particles leave an extremely porous product (rust) as they burn (oxidize),

which allows complete diffusion of oxidizer throughout the remaining un-oxidized particles.

According to Eq. (4.3) the effective Lewis number depends on the area fraction (volume fraction in 3D) occupied by solid metal particles Φ_s . The continuum-limit of chapters 2 and 3 corresponds to $\Phi_s = 1$, with Lewis number corresponding to $Le^e(\Phi_s = 1)$. To simplify notation, we hereafter denote Le as the Lewis number of the continuum limit. Using this notation, the effective Lewis number in random media Le^e can be expressed in terms of its value in the continuum limit as

$$Le^e(\Phi_s) = \frac{f(\Phi_s)}{f(\Phi_s = 1)} Le. \quad (4.4)$$

This relation implies that the Lewis number in a random medium, where the area fraction occupied by particles is smaller with reference to the continuum limit, is effectively lower than the corresponding value in that limit. Furthermore, as it was pointed out earlier in this thesis, we expect the cellular stability boundary to shift with respect to its continuum limit. The approximate value of the effective critical Lewis number Le^e , corresponding to this stability boundary, can be obtained by substituting Eqs. (3.9) for critical Lewis number Le_c for zero-order kinetics in the continuum limit [22] into Eq. (4.4). This gives

$$\begin{aligned} Le_c^e(\theta_{ign}, k = 0, n = 0, \Phi_s) &= \frac{f(\Phi_s)}{f(\Phi_s = 1)} \left[\frac{R}{2 \exp(R) - R - 2} \right], \\ \theta_{ign} &= \frac{1 - \exp(-R)}{R}. \end{aligned} \quad (4.5)$$

The critical Lewis number in the random media for the first-order kinetics also can be obtained in the similar way. Based on this equation, the cellular stability boundary is shifted towards lower values of Lewis number by a factor of $f(\Phi_s)/f(\Phi_s = 1)$, and can be

determined by knowing the ignition temperature θ_{ign} and for a given area fraction Φ_s of particles in random media.

We examined if the effective Lewis number in Eq. 4.4 numerically allows us to map the behaviour of combustion fronts in random media onto the effective behaviour of continuum combustion fronts. Figure (4–3) shows random combustion front data for $\text{Le} = 0.3$ and $\text{Le} = 0.45$, as well as the analytical dispersion relation of the continuum model of chapter 3 for the case of $\text{Le} = 0.3$. As a reminder, ($\Phi_s = 0.7$; $N_s = 16$), and $L_y = 160 d$ in the case of the random combustion front, and a planar steady-state solution is used for initial condition. The data represent averaged growth rates from two random configurations of the system. For $\Phi_s = 0.7$, Eq. (4.4) gives $\text{Le}^e = 0.3$ as the effective Lewis number corresponding to $\text{Le} = 0.45$. Comparing the (●) data and (■) data in Fig. (4–3), shows that the randomness of particles in discrete limit of combustion, at least qualitatively, has the same effect as lowering the Lewis number in the continuum limit. Also, as discussed previously, the tip-splitting process in cellular regime of combustion in random media resembles the same mechanism in seaweed structures (Fig. 3–14). Moreover, the characteristic length of the patterns in both cases are nearly commensurate and is given by $k \sim 0.05 \pi/d$.

On the other hand, the above numerical results indicate that the effective Lewis number data in Fig. (4–3) do not quantitatively match the analytical solution as we conjectured from the theoretical discussion above. The discrepancy between these two results may be attributed to the accuracy of our calculation as shown by the large error bars in Fig. (4–3). These error bars give indication of variation of the mean growth rates ω , and can be reduced by increasing the number of initial realizations. Another possible scenario is that the effective Lewis number given by Eq. (4.4) is not accurate enough to capture the effect

of small-scale fluctuations of the combustion front due to the heterogeneous nature of the fuel particle distributions.

4.2 Cellular combustion front in random media: Late-time regime

This section studies the effect of random particle distribution on the long-time dynamics of the cellular front. The results of this section will provide deeper understanding of the formation process and stability of cellular patterns in random heterogenous media. For this purpose numerical simulations are performed by assuming both uniform and nonuniform random distribution of particles. Similar to the last section, this study limits itself only to the zero-order kinetics $n = 0$ which is more realistic choice for a combustion flame in suspension of particles.

We first examine the effect of random heterogenous medium on the morphology of cellular patterns for a range of inter-particle spacing and particle sizes. Additionally, we probe the effect of Lewis number on combustion front propagation in randomly distributed particles by using the concept of effective Lewis number that was introduced in the last section. We finish our investigation of this section by studying the cellular pattern formation in samples with a non-uniform random particle distribution and for a range of inter-particle spacing and particle size distribution.

4.2.1 Effect of stochastic nature of particle system on cellular fronts

Our numerical findings of the early-time evolution of a combustion front in a random particle distribution reveal that the dynamics of a front becomes rapidly dominated by non-linear effects, characterized by early non-symmetric deep cellular patterns. At later times, these cells become unstable due to the heterogeneity of a medium causing successive tip-splitting, and never reach a steady-state. This subsection examines the late-time evolution of combustion fronts propagating in random media.

Figure. (4–4-(a)) shows a numerical simulation of the evolution of a random combustion front for model parameters $\text{MM}(n = 0; \text{Le} = 0.3; \theta_{\text{ign}} = 0.75)$ in a rectangular domain whose dimensions are set to $(L_x = 200 d, L_y = 80 d)$. To represent a random media, we use identical particles that have a uniformly random distribution characterized by $\Phi_s = 0.7; N_s = 16; D_p = 0.236 d$. The average inter-particle spacing for the given set of parameters is $l_p \sim 0.3 d$. The simulation is initiated by a flat interface with the solution of a planar front along the direction of the front. The 1D front represents the isotherm $\theta(x, y) = \theta_{\text{ign}}$, and the total simulation time is $t = 30 \tau$. The position of 1D interface $x = f(y, t)$ is plotted every $\Delta t = 0.32 \tau$

Figure (4–4-(a)) shows that the combustion front first develops primary branches some of which are eliminated shortly after their emergence. The surviving ones then continue to grow and eventually either split and give rise to smaller cells, or become terminated. The mechanism of tip splitting and cell elimination is analogous to what we observed before in dendritic seaweed structures in the continuum limit for low Lewis numbers (Fig. (3–13))

⁴. However, the cellular structure in this case has some features that distinguish it from the patterns in the continuum limit.

In order to examine these aforementioned differences quantitatively, we calculate the spectral power density of the 1D interface in Figure (4–4-(a)). This is shown in Figure (4–5-(a)). The peaks in the power spectrum are amplitudes of discrete k modes that can be accommodated within a system size L_y (see Fig. 3–1-(b)). These modes characterize the length-scales of the cellular structures. The mode $k = 0.175 \pi/d$ in Fig. (4–5-(a)) corresponds to the visual inspection of the primary finger width (prior to tip-splitting), which is $l \sim 11.5 d$. This indicates that the cell spacing, on average, is smaller for the combustion front in a random medium compared to seaweed structure in the continuum case, for the same lateral dimension L_y and Lewis number (Fig. 3–13). It is noted that the power spectra shown here are suggesting of trends only, and more quantitative measurements from these would require many more interface realizations to be ensemble-averaged.

Fig. (4–4-(b)) shows the effect of a random medium with larger inter-particle spacing on the pattern formation of the combustion front. Here, the number density of particles is set to a smaller value $N_s = 4$ ($\Phi_s = 0.7$). The particle size (diameter) and inter-particle spacing for the new number density thus become $D_p = 0.472 d$ and $l_p \sim 0.6 d$, both two times larger than before. Compared to Fig. (4–4-(a)), cellular patterns appear after a longer transient time. This happens due to the larger inter-particle spacing, which eliminates the

⁴ The seaweed structures in Fig. (3–13,3–14) are obtained for first-order kinetics, however, we also expect that it would be observed for zero-order kinetics, but at relatively smaller values of Le.

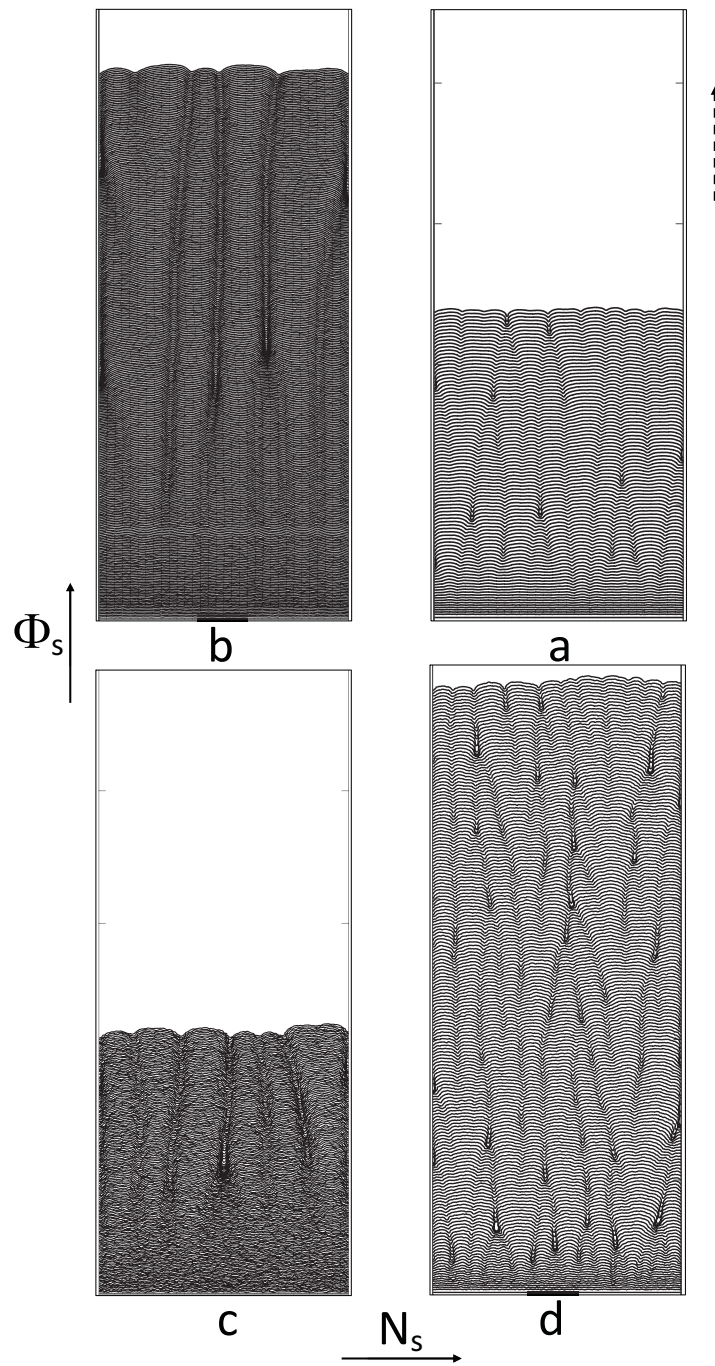


Figure 4–4: Temporal history of evolution of 1D front $x = f(y, t)$ corresponds to isotherm $\theta(x, y) = \theta_{\text{ign}}$ for model parameters $\text{MM}(n = 0; \text{Le} = 0.3; \theta_{\text{ign}} = 0.75)$ and for a uniform random particle distribution with area fraction Φ_s and number density: a) $N_s = 16$, and b) $N_s = 4$; and for area fraction $\Phi_s = 0.4$ and number density: c) $N_s = 4$, and d) $N_s = 16$. The direction of front propagation is shown by the dashed arrow.

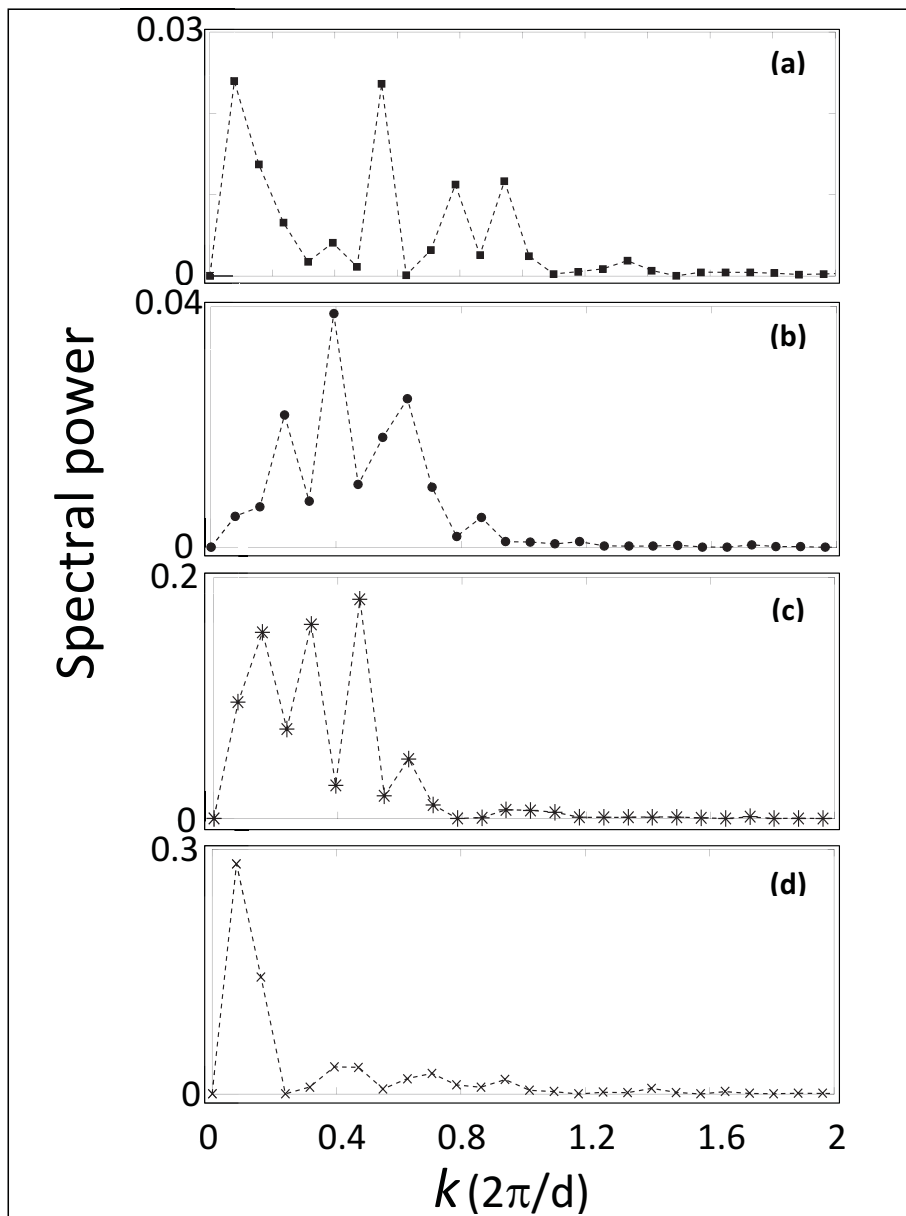


Figure 4–5: The spectral power of the interface $x = f(y, t)$ of combustion fronts in Fig. (4–4) taken at $t = 30\tau$ for model parameters MM($n = 0$; $\text{Le} = 0.3$; $\theta_{\text{ign}} = 0.75$) and for a uniform random heterogenous medium with a) $\Phi_s = 0.7$, $N_s = 16$; b) $\Phi_s = 0.7$, $N_s = 4$; c) $\Phi_s = 0.4$, $N_s = 4$; d) $\Phi_s = 0.4$, $N_s = 16$.

high- k mode selection in the linear instability process. Thus, relative to the larger number density $N_s = 16$, the number of cellular branches is decreased while the cell spacing, on average, is increased. This is better presented in Fig. (4–5-(b)), which shows the spectral power density of the 1D interface in Fig. (4–4-(b)) at $t = 30\tau$. It is seen that the modes of characterizing the cellular front patterns are shifted towards the lower k mode for this case of lower number density, signalling the increase in cellular spacing length-scales. The mode corresponding to the visual inspection of the average primary cell width in Fig. (4–5-(b)) is equal to $k = 0.125\pi/d$.

We next investigate the effect of area fraction Φ_s on cellular patterns. We fix the value of the number density to $N_s = 4$ and set the area fraction to $\Phi_s = 0.4$ for which the particle diameter $D_p = 0.357d$ and average inter-particle spacing $l_p \sim 0.55d$ are obtained. The result of this simulation is presented in Fig. (4–4-(c)). This result indicates that by keeping the number density of particles constant as the area fraction decreases, the number of emerging cellular branches remains almost the same while their spacing is decreased their spacing is the same, the cell-depth are changing. Considering that the inter-particle spacing is roughly the same in the systems (b) and (c), the discrepancy between their cellular morphology can be attributed to the different particle size in each case. The smaller size of particles in the case (c), compared to (b), essentially reduces the amount of heat generation locally which leads to reducing the stabilizing effect of heat conduction. In this situation the front instabilities are promoted to grow faster and develop slightly deeper cells. Under these conditions, the k -numbers corresponding to these instabilities are expected to have larger amplitudes than the two previous examples. The distribution and amplitudes of unstable k modes of the 1D cellular interface at $t = 30\tau$ are shown in Fig. (4–5-(c)). As

compared with the spectral power density Fig. (4–5-(b)), for the same N_s and higher Φ_s , the distribution of modes is now roughly the same and the cell spacing similar, consistent visual inspection of Fig. (4–4-(c)). However, the amplitude of the excited modes in Fig. (4–5-(c)) are nearly 5 times larger than those observed in Fig. (4–5-(a)) and Fig. (4–5-(b)), which is likely due to the deeper grooves/cusps that develop in this case.

Comparing the features of cellular pattern for Fig. (4–4-(a)) with ($\Phi_s = 0.7; N_s = 16$) Fig. (4–4-(c)) with ($\Phi_s = 0.4; N_s = 4$), it is thus observed that decreasing both N_s and Φ_s generally results in the appearance of deeper cells and larger cell spacing. This distinction can also be observed from their corresponding spectral power density in Fig. (4–5), and is observed in other random realizations as well. A key observation made from the above data is that decreasing both N_s and Φ_s appears to result in a transition away from seaweed-like dendritic structures of the combustion front, and more towards a cellular front.

To complete this analysis, we probe the dynamics of a combustion front in the random medium with small particle size but large number density. The simulation is conducted in random media whose area fraction and number density is set to $\Phi_s = 0.4$, and $N_s = 16$, respectively. The particle diameter and inter-particle spacing for the given area fraction and number density becomes $D_p = 0.178 d$ and $l_p \sim 0.3 d$. The simulation result is presented in Fig. (4–4-(d)). This results show that with increasing number density (lowering inter-particle spacing), a seaweed-like structure morphologically analogous to that in Fig. (4–4-(a)) emerges again, except here the features are finer and more deep-grooved. This can be attributed to the smaller particle size. As we explained earlier, a combustion front in a random medium where particles are small is more unstable against the local perturbations due to the reduced stabilizing effect of heat conduction. The difference between the

cellular structure in Fig. (4–4-(a)) and Fig. (4–4-(d)) is also reflected in their corresponding spectral power density in Figure (4–5-(d)). This shows activity at similar k -modes as Fig. (4–4-(a)) but a higher amplitude at the smallest k -mode, which is plausibly the undulation between larger primary branches (each with its own smaller sub-branches), that is leading to the deeper grooves observed in Fig. (4–4-(d)).

The numerical results of this section reveal that decreasing the number density of fuel particles will reduce the number of excited modes which leads to a gradual transition from seaweed-like front morphologies toward cellular-type structures, with correspondingly deeper spacing between cells. The results of this sub-section also suggest that there may be a similarity in behaviour between the distribution of fuel particles on the cellular-seaweed transition behaviour that is analogous to changing low-Lewis number as studied in the continuum case.

4.2.2 Effect of Lewis number on the late-time dynamics of a cellular front

Here we examine the effect of Lewis number on dynamics of a propagating front in a random medium. The random distribution of particles is assumed to be uniform and is identified by ($\Phi_s = 0.7$; $N_s = 16$; $D_p = 0.236 d$). The inter-particle spacing for this sample is $l_p \sim 0.3 d$. The model parameters are set to $MM(n = 0; Le; \theta_{ign} = 0.75)$ where we choose an effective Le based on the area fraction of particles $\Phi_s = 0.7$ by employing Eq. (4.4). The system under consideration here is essentially identical to the one that we studied in the last section (Fig. 4–4-(a)), except the Lewis number in that case is $Le = 0.3$, while here it is replaced by its effective value $Le = 0.45$, to presumably recover the same

behaviour with a random distribution of particles as was the case in the corresponding continuum system. The simulation is done in a computational domain with dimensions of ($L_x = 200 d$, $L_y = 80 d$), where as a reminder d is the inter-particle spacing when particles are placed on a regular square lattice and its value is given by $d = \sqrt{(N \pi D_p^2)/(4 \Phi_s)}$, N being the number of particle centres in each domain within an area ($d \times d$). The fossilized temporal history of a 1D front $x = f(y, t)$ corresponds to isotherm $\theta(x, y) = \theta_{\text{ign}}$ is plotted in figure(4–6). The duration of the simulation was $t \sim 38 \tau$ and the interface position is plotted every $\Delta t = 0.32 \tau$. As it is clear from Fig. (4–6), the morphology of cells is clearly

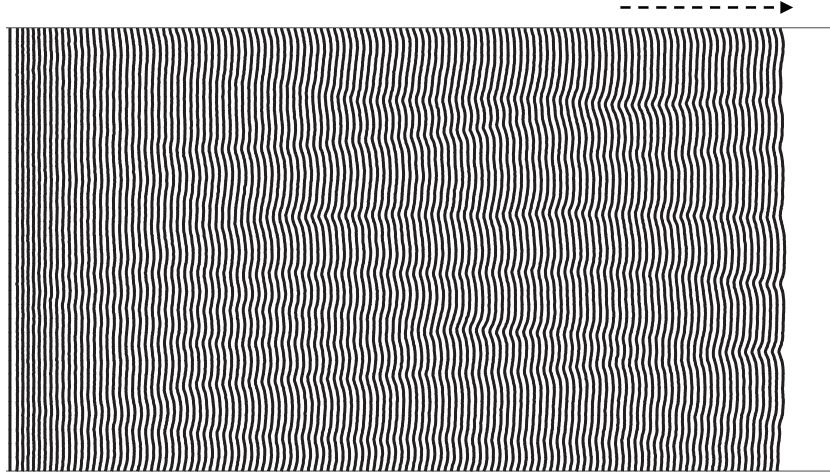


Figure 4–6: Temporal history of evolution of 1D front corresponds to isotherm $\theta(x, y) = \theta_{\text{ign}}$ for model parameters MM($n = 0$; $\text{Le} = 0.45$; $\theta_{\text{ign}} = 0.75$) and for a uniform random particle distribution with $\Phi_s = 0.7$ and for $N_s = 16$. The direction of front propagation is shown by the dashed arrow.

changed from the seaweed-like structure with deep cells in Fig. (4–4-(a)) to a shallow cellular pattern.

Figure (4–7) plots the spectral power of the 1D interface in Fig. (4–6) at $t = 30 \tau$. It shows that the amplitude and number of k modes in this interface decreases compared to Fig. (4–5-(a)). The highest peak in both cases, belongs to the lowest mode $k = 2\pi/L_y$

which may be an undulation at the scale of the finite-size of the system. The activity around the broader peak around $k \approx 0.127\pi/d$ is consistent with the development of the shallow cells seen in Fig. (4–7). It was seen in chapter 3 that increasing the Lewis number lead to decreasing growth rate of instabilities and lead to shallow cells, morphologically similar to those in Fig. (4–6). Thus, it appears that combustion fronts in a random media at high Lewis number may have the similar characteristics as the ‘quasi-Linear’ regime in the continuum limit in chapter 3. Further work is required to elucidate this effect quantitatively.

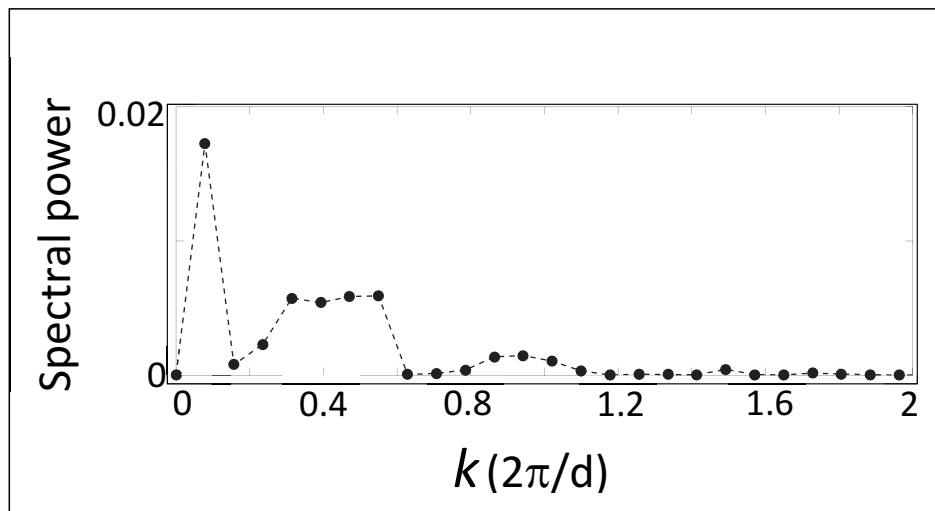


Figure 4–7: The spectral power of the interface $x = f(y, t)$ of combustion front in a random media with identified by $(\Phi_s = 0.7; N_s = 16)$ and for model parameters MM($n = 0$; Le = 0.45; $\theta_{ign} = 0.75$).

4.2.3 Effect of uniformity of a random particle distribution of cellular patterns

In this section we examine the dynamics of a cellular flame front in non-uniform random media. So far we investigated the dynamics of combustion front propagating in a random medium, where uniform distribution of particles was assumed. In these isotropic and homogenous systems the characteristic length-scale is the average inter-particle distance that is derived from the two-particle correlation function. In the non-uniform samples, however, particles are randomly distributed with area fraction (and inter-particle spacing) that is not a constant, but varies locally in space. Also the saturation limit for area fraction in the non-uniform cases are significantly lower than that in the uniform sample, which may have a stronger local effects on the dynamics of the front. Thus, the dynamics of a front in this case may strongly depend on the randomness of the medium over length-scales that are commensurate with thermal length of the flame.

In order to compare the outcome of this section with our previous results for uniform samples, simulations are conducted within a computational domain with the same size as before (i.e. $L_x = 200 d$ and $L_y = 80 d$), and model parameters for zero-order kinetics as $\text{MM}(n = 0; \text{Le} = 0.3; \theta_{\text{ign}} = 0.75)$. We initially set the target values for a specific distribution to ($\Phi_s = 0.4, N_s = 1$). The particle size is $D_p = 0.71 d$. In order to find an estimate of inter-particle spacing in this case, we perform statistical averaging of correlation function over 100 of these non-uniform realizations. The statistical inter-particle spacing obtained is $l_p \sim 1.17 d$ which is comparatively larger than that for the higher area fraction cases in the uniform samples that we have studied before (Fig. (4–4)). A simulation is initiated by the steady-state solution of a planar interface. The evolution of a typical 2D front is displayed in Fig. (4–8). The duration of the simulation was $t = 116 \tau$, and the time of this

image is $t = 98\tau$. The particles in the figure are marked by black dots. Here, cellular pattern emerges with a relatively large cell-spacing. The reason for the emergence of this morphology, as we explained before, is that small length scales are suppressed due to the large particle spacing. The existing cells then can only be perturbed by morphological instabilities with larger wavelengths. Therefore, once these cells formed it takes a comparatively longer time for cells to split. The dynamic behaviour of this combustion front also can be seen from the fossilized version of temporal history of the front in Fig. (4–9–(a)). It is clear from the figure that the cell-depth (defined as max-to- min positions on the interface) is increased compared to its continuum counterpart of these parameters examined in chapter 3, indicating the destabilizing effect of random media.

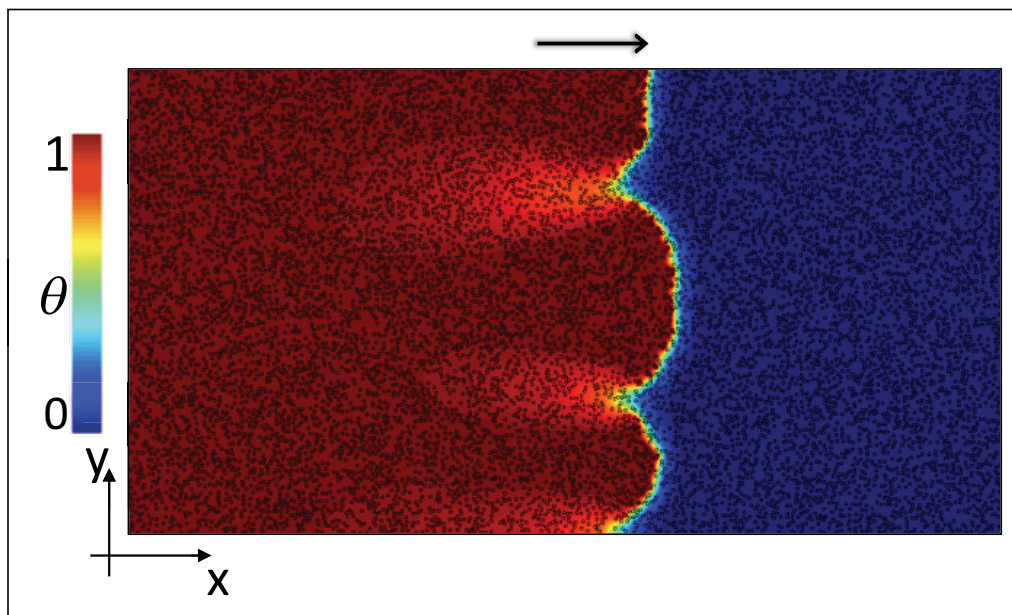


Figure 4–8: Contours of the dimension-less temperature field for model parameters $\text{MM}(n = 0; \text{Le} = 0.3; \theta_{\text{ign}} = 0.75)$ and in a non-uniform random medium with $(\Phi_s = 0.4; N_s = 1)$. The steady-state solution of a planar front is used as the initial condition. The arrow shows the direction of propagation along x coordinate. Colour-bar on the left hand side of the figure shows the dimension-less temperature scale.

We next investigate the effect of both number density and area fraction in non-uniform samples, where we used the same computational domain size and model parameters as in Fig. (4–8). We prepared samples of non-uniform random particles for two values of area fraction ($\Phi_s = 0.4$, $\Phi_s = 0.1$), and for each, examined three number densities ($N_s = 1$, $N_s = 2$, and $N_s = 4$). The results of these simulations are displayed in Fig. (4–9). This figure shows that for the same area fraction, the number of cellular branches increases by increasing the number density. This again, is the result of large number density which reduces the heterogeneity of the medium and thus allows modes of smaller wavelengths to become unstable in the resulting pattern. Moreover, for samples with $N_s = 1$ and $N_s = 2$ for both area fractions ((a,b) and (d,e)), no primary tip-splitting event is observed, at least up to the end of our simulations. As we increase the number density to $N_s = 4$ for both $\Phi_s = 0.4, 0.1$ in samples (c) and (f), the combustion front clearly experiences tip-splitting. Additionally, by decreasing the area fraction Φ_s , while keeping the number density constant, the number of branches do not change while cells become deeper grooved, i.e. larger max-to-min distance of cells. Since for the lower area fraction, the particle sizes are smaller, and as we already discussed in the previous sub-section, the destabilizing effect of randomness becomes more significant.

Fig. (4–9) shows that the morphology of a combustion front responds to changes in number density and area fraction in non-uniform samples in an analogous manner as was observed in uniform samples, except in this case the combustion front tends to be rougher. Comparing Fig. (4–9-(c)) with Fig. (4–4-(c)) (for cases of the same number density and area fraction) shows that the morphology in non-uniform particle distributions is different

from the uniform case. The number of cell branches is reduced while their cell spacing increases. This might be due to the larger statistical inter-particle spacing in the non-uniform case. Also the pattern in non-uniform case is less symmetric which is related to local fluctuation of area fraction.

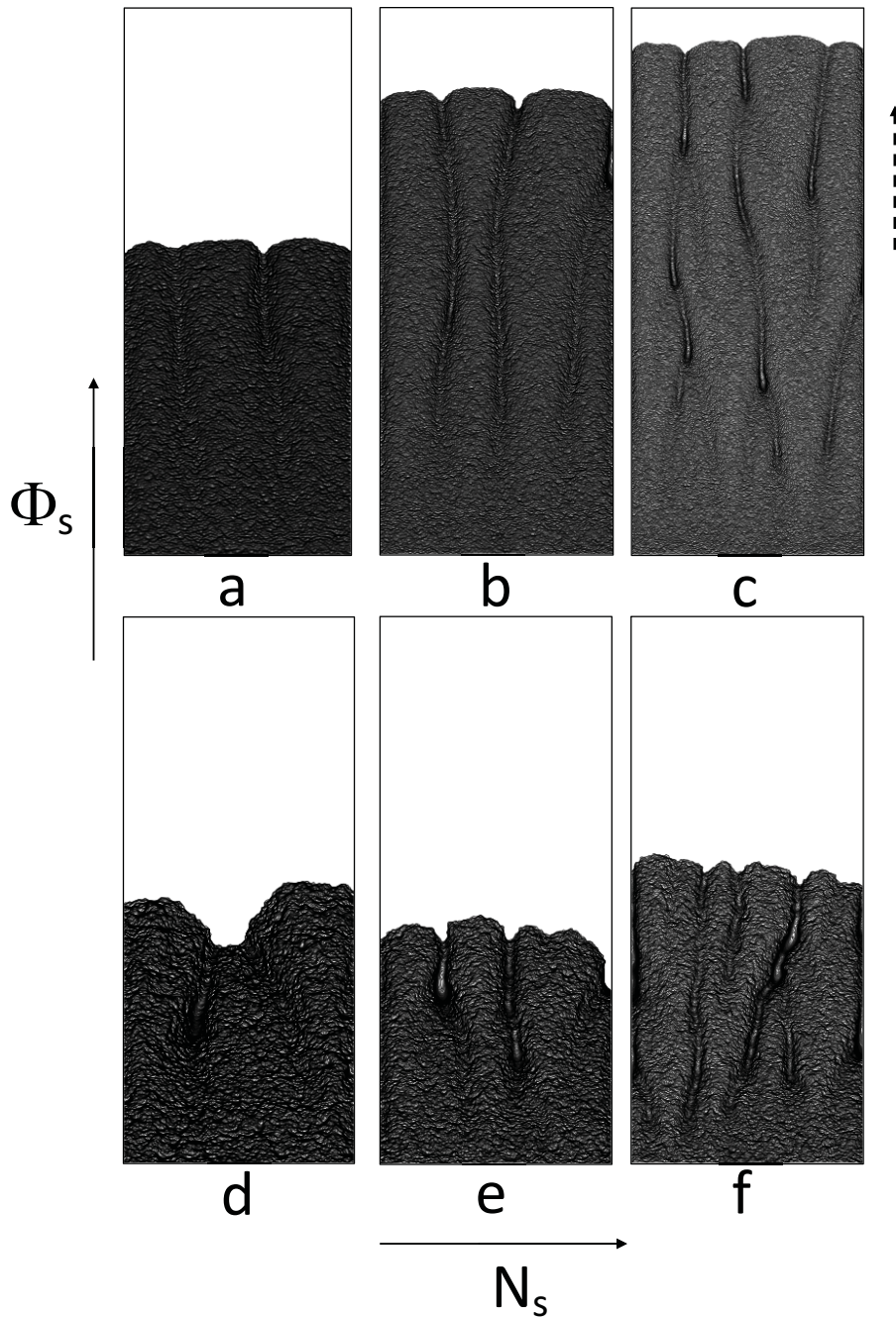


Figure 4–9: Temporal history of evolution of 1D front $x = f(y, t)$ corresponds to isotherm $\theta(x, y) = \theta_{\text{ign}}$ for model parameters $\text{MM}(n = 0; \text{Le} = 0.3; \theta_{\text{ign}} = 0.75)$ and for a non-uniform random particle distribution with area fraction $\Phi_s = 0.4$ and number density: a) $N_s = 1$, b) $N_s = 2$, and c) $N_s = 4$; and for area fraction $\Phi_s = 0.1$ and number density: d) $N_s = 1$, e) $N_s = 2$, and f) $N_s = 4$. The direction of front propagation is shown by the dashed arrow.

4.3 Summary

This chapter investigated the dynamics of a combustion front propagating in a random media using zero-order kinetics ($n = 0$), and a small value of Lewis number ($\text{Le} = 0.3$), for which the cellular pattern is observed in the corresponding continuum limit case of chapter 3. Our numerical results of early-time evolution of a combustion front show that the amplification rate of modes of morphological instabilities does not follow the linear regime prediction as we observed in the continuum limit in chapter 3. This can be attributed to non-linear effects due to the particle stochasticity, which dominate the dynamics of the cellular growth and result in the emergence of complex structures. This structure composed of non-symmetric deep cells that undergo tip-splitting, repeatedly. However, very early growth rate of the excited modes seems to *statistically* follow the linear regime of an effective Lewis number.

Our numerical calculation for unstable modes in their early-time regime predicts a relatively faster growth rate than the analytical solution for the continuum limit derived by [22]. These numerical findings suggest that the destabilizing effect of random medium is qualitatively analogous to lowering the Lewis number in the corresponding continuum limit. To test the correspondence between random media and low Lewis number hypothesis, we derived an analytical expression for the *effective* Lewis number Le^e in terms of area fraction of the random medium Φ_s and Lewis number in the continuum limit Le . This expression indicates that the Lewis number is effectively reduced in randomly distributed particle media. Our numerical results in the early stages of front evolution for increasing Lewis numbers, as predicted by the aforementioned effective Lewis number criterion,

show that the growth rate of unstable modes is indeed reduced and becomes more consistent with the analytical linear dispersion relation [22].

The late-time dynamics of cellular pattern formation in random media was also investigated. We specifically studied the effect of area fraction and number density on number of cellular fingers and cell spacing. These results indicate that for both uniform and nonuniform samples of random particles, changing the area fraction will change the cell-depth, while changing the number density changes the morphology. For the highest value of number density and area fraction $\Phi_s = 0.7; N_s = 16$ which is near its continuum limit, we observed a seaweed-like cellular structures corresponding to the lower Lewis number structure in the continuum limit. By decreasing both Φ_s and N_s , the number of cellular branches decreases while the cell spacing increases. Also we found that the robustness of a cellular pattern against perturbations, increases by decreasing the number density. The same effects of number density and area fraction on cellular morphology are also observed for non-uniform samples, except in these systems since only small area fractions are possible, inter-particle spacing on average is larger and thus combustion fronts become rougher.

Our numerical observations for the effect of Lewis number on the late-time dynamics show that in general the random distribution of particles is qualitatively analogous to the effect of low-Lewis numbers in the continuum limit. We show that by increasing the Lewis number, the morphology of seaweed-like structure will change to regular shallow cells. This morphology is similar to what we observed in the continuum limit for high Lewis numbers in the regime that was called “quasi-linear” regime. The results of this chapter show a possibility of connecting –in a statistical sense– the morphologies of combustion

fronts in random particle suspensions to those in continuum media, as a function of the Φ_s and N_s of the distribution.

CHAPTER 5

Conclusion

In this work we study the morphological pattern formation of non-isothermal solid-gas combustion fronts, focusing on cellular morphologies. In these combustion systems, the propagation of chemical fronts accompanied by heat release from an exothermic chemical reaction, such as oxidation. The instabilities and resulting cellular patterns of solid-gas combustion fronts are examined in the framework of thermo-diffusive instability model, assuming both continuous and random reactant (solid metal particles) distributions, and for the physical parameters of the problem (i.e. order of the chemical reaction $n = 0, 1$, ignition temperature T_{ign} , and Lewis number Le). In our numerical simulations, by employing a novel adaptive mesh refinement algorithm we achieve experimentally relevant system sizes.

We introduced a unified mathematical combustion model coined the “master model” for combustion of solid metal particle fuel in the presence of oxidizer for zero and first-order kinetics. The master model is discussed in two different limits of combustion, namely, discrete random and continuum limit. In the former case, the set of equations that governs the dynamics of a combustion front in the heterogenous combustible medium, is derived based on the combustion of particulate fuel in hot oxidizer gas. This combustion process is also examined in the limit of a continuum fuel source. In general, a continuum-limit approach is valid when the heterogeneity of a medium, denoted by the average inter-particle spacing l_p , is significantly smaller than the thermal length of a flame

(i.e. $l_p \ll \delta_c$). The corresponding equations for a combustion front in this limit is derived by coarse-graining over length scale much larger than inter-particle spacing. The gas-less limit ($\text{Le} \rightarrow \infty$) of master model for both kinetic orders ($n = 0, 1$), was examined analytically to connect the master model to previously established models.

Our numerical results for a combustion front in the continuum limit, show that a front for the values of Lewis number below a critical Lewis number Le_c , develops a cellular morphology. The transition from a planar front to a cellular structure can be explained in the context of thermo-diffusive instability mechanism. The linear regime of the cellular fronts is investigated numerically and found to agree well with the dispersion relation predicted analytically by Brailovsky et al. Our results indicate that lowering the value of the Lewis number, broadens the range of instability modes that can be triggered, and increases the growth rates of the most unstable k modes. The effects of system size on the liner regime of cellular flame front is also addressed. The outcome of this analysis reveals that the lateral system size L_y can only accommodate a discrete number of modes, and modes that are incommensurate with harmonics of these size-specific modes will not grow as fast in the early-time regime, or at all. These results also indicate that in a wider system, the number of modes that can be potentially excited becomes larger, with the fastest growing mode becoming closer to the analytical prediction. The numerical findings for the late-time evolution of a combustion front, suggest that for the values of Lewis number Le close to its critical value Le_c , the transition from linear to non-linear (i.e. late time) will be prolonged. The morphology of front in this regime is characterized by its shallow-cell structure, which can be described *qualitatively* based on the fastest growth modes available in the linear regime. For this reason, this regime is called “quasi- linear” regime. By lowering

the value of Lewis number below $\text{Le} \sim 0.4$, the cellular morphology altered significantly and becomes complex, featuring non-symmetric deep cells and overhangs. By further decreasing the value of Lewis number, cellular fingers undergo a series of tip-splitting events and the evolution becomes dominated by side branching which is the hallmark of seaweed dendritic growth, emphasizing parallels with isotropic dendritic microstructures in solidification phenomena. The transition from shallow cellular morphology to more complex seaweed dendritic patterns for the first-order kinetics ($n = 1$) occurs for $\text{Le} \leq 0.1$. Our investigation of the influence of system size on the late-time dynamics of tip splitting and merging, indicate that the system size-effect can prevent a cellular front from establishing a dominant growth pattern and instead the cellular branches undergo a rapid series of tip-splitting and cell overgrowth events. In a larger system size, on the other hand, a cellular front can develop more regular patterns by the process of tip splitting and merging which likely repeats again, making the morphology statistically repetitive. However, to confirm this for sure, a statistical analysis of branch number and spacing over a much greater time would have to be measured. The dendritic patterns simulated in this work are similar to those observed in experiments of flame propagation over a bed of nano-aluminum powder burning with a counter-flowing oxidizer conducted by Malchi et al. It is noteworthy that the physical dimension of our computational domain is roughly close to their experimental setup. To our knowledge, our simulations are the first to simulate such patterns in combustion fronts at experimentally relevant domain sizes and parameters. Such patterns are also analogous in their physics to those observed in directional solidification. Other examples of this parallel include the analogy between Saffman-Taylor combustion finger and dendrite solidification fingers. Dendritic patterns are paradigms of pattern formation

when there is a competition between diffusion-limited transport and a stabilizing force at the interface.

The early-time evolution of a cellular combustion front for the first-order kinetics under heat dissipation conditions is examined, numerically and analytically. Our numerical results of the dispersion relation, in line with our analytical solution, predict that the growth rate of high- k modes in the presence of heat dissipation, can be effectively described by the same modes as in the adiabatic condition, but with their amplification rate increased. These results, thus suggest that the high- k mode behaviour of the dispersion relation in heat dissipative regime can be thought of as that of an adiabatic system but with *lower* Lewis number. The numerical dispersion relation for low- k modes, however, exhibits different behaviour from the analytical solution. The dispersion relation, as predicted by the analytical solution, goes to a constant as $k \rightarrow 0$, while our numerical results show that the growth of low- k modes vanishes as $k \rightarrow 0$. It is plausible that this is an artifact of finite size effects used in our simulations, which suppresses the growth of low- k modes. The analytical dispersion relation for very low- k modes, is analogous to the results of Joulin et al. in their study of non-adiabatic cellular flames, where they used the kinetic-limited model with the Arrhenius reaction rate that is relevant for premixed gaseous flames with high activation energy.

The numerical inspection of the early-time evolution of a combustion front propagating in the random discrete medium, was carried out for the zero-order kinetics $n = 0$, and set of physical parameters ($\text{Le} = 0.3; \theta_{\text{ign}} = 0.75$). A continuum-limit combustion front for the given set of parameters develops a shallow-cell structure. According to the results the dynamics of a front, even at the early times of evolution, is dominated by non-linear effects

that are caused by particle stochasticity, leading to the appearance of a complex cellular pattern. These high-amplitude cells, as they grow wider, become laterally unstable and split. The modes that are triggered following a tip splitting, however, seem to follow the linear growth regime for a short time period, which may happen due to amplitude reduction of cells before and during a tip-splitting event. Moreover, the numerical results for unstable modes in the early-time regime, predict a relatively faster growth rate than the analytical solution for the continuum limit, which may suggest that the destabilizing effect of random medium is, at least qualitatively, analogous to lowering the Lewis number in the corresponding continuum limit. This mechanism can be understood based on the random nature of the reaction centres (i.e. fuel particles) that effectively acts to reduce the gradient of the local temperature (through local heat dissipation) thereby reducing the stabilizing effect of heat diffusion on instabilities. To examine the destabilizing effect of a random medium quantitatively, we derive an analytical expression for the *effective* Lewis number in random media Le^e in terms of area fraction of particles Φ_s and Lewis number in the continuum limit Le . Our numerical results in the early stages of front evolution for increasing the Lewis number, as predicted by the effective Lewis number criterion, show that the growth rate of unstable modes is indeed reduced and becomes more consistent with the analytical linear dispersion relation. The morphology of a cellular combustion front in a random medium in late-time regime, as suggested by our numerical results, can be characterized as functions of the parameters of random distribution (i.e. area fraction Φ_s , and number density N_s of fuel particles). According to our findings for both uniform and nonuniform samples of random particles, changing the area fraction will change the cell-depth (max-to-min distance of cells), while changing the number density changes the

morphology. For the highest value of number density and area fraction that we could achieve in our numerical simulations ($\Phi_s = 0.7$; $N_s = 16$), a seaweed-like structure corresponding to the lower Lewis number morphology in the continuum limit is observed. By lowering both Φ_s and N_s , the number of cellular branches decreases while the cell spacing increases. The same effects of number density and area fraction on cellular morphology are also observed for non-uniform samples, except in these systems since only small area fractions are possible, inter-particle spacing on average is larger and thus combustion fronts become rougher. These results also indicate that the robustness of a cellular pattern against perturbations increases by decreasing the number density. The numerical analysis for the late-time dynamics shows that, in general, the random distribution of particles is qualitatively analogous to the effect of low-Lewis numbers in the continuum limit. Increasing Lewis number, based on the effective Lewis number criterion, will reduce the impact of random particle distribution, leading to transition from a complex seaweed-like structure to a shallow-cell pattern. This morphology is similar to what we observed in the continuum limit for high Lewis numbers in the regime that was called “quasi-linear” regime. The results of the numerical analysis of pattern formation of combustion fronts in random media seem to suggest connections –in the statistical sense– between cellular morphology in random particle suspensions to those in continuum media, as a function of the Φ_s and N_s of the distribution. To confirm this, However, a statistical analysis over a sufficiently large number of realizations of a random medium and for a much greater time would be required.

Although this study focuses on combustion fronts, the results of the investigation presented above, are worth discussing within the context of other propagating reaction-diffusion front where stability mechanisms similar to thermo-diffusive instabilities are present such as isothermal reaction-diffusion fronts.

Appendix A

**Derivation of combustion equations in a discrete heterogenous medium using one
particle combustion in hot oxidizer gas**

A.1 One particle combustion in the presence of oxidizer

In deriving the analytical equations governing one particle combustion, we made same assumptions and follow the same approach developed by [166]. The reaction mechanism (kinetics) for the particle combustion in a hot oxidizer gas depends on the particle size and can be classified in the following way:

1 - Combustion of small particle ($r_p \sim 1\mu m$):

Reaction kinetics for these particles is well described by Arrhenius kinetics during which the temperature of the particle increases with gas temperature, exponentially. The reaction of this kind occurs under thermal equilibrium between particle and the oxidizer gas surrounding it. The rate of reaction increases with gas-particle temperature. This regime where the combustion of particles is merely depends on the reaction kinetics, is called “Kinetic-limited” regime.

2 - Combustion of intermediate and large particles ($r_p > 7\mu m$):

For large particles, on the other hand, the mechanism of the reaction is different, and can not be only described by Arrhenius kinetics. In these systems, particle temperature, in contact with hot oxidizer gas, keeps increasing according to Arrhenius kinetics, until the rate of heat generation by the particle becomes greater than rate of its heat dissipation to the gaseous environment. At this point, the particle ignites and its temperature exceeds the gas temperature. The reaction after ignition occurs on the surface of the particle. During this surface reaction, the main factor that controls the particle combustion is the oxidizer's transfer rate from the bulk towards the surface of the particle. The time it takes for the oxidizer to reach the surface of the particle is longer than relatively short surface reaction

time. This regime of combustion, in which the surface reaction depends on the migration rate of oxidizer concentration towards the particle surface is called “diffusion-limited” regime. In this work, we consider only large metal particles for which diffusion-limited discussion can be applied. In order to derive the combustion rate of such a particle, the following assumption and simplification are made:

- reaction (oxidation) occurs on the surface of a particle according to the Arrhenius rate

$$K(T_s) = k_o \exp\left(\frac{-E}{RT_s}\right), \quad (\text{A.1})$$

where T_s is the temperature of the particle’s surface

- the surface reaction occurs very fast that there is always a lack of oxidizer in the vicinity of the particle surface.
- The particle burns in a quiescent, infinite spherically gaseous environment and the convection effect is neglected
- The combustion is treated as a steady-state process and spatial temperature and concentration profiles of gaseous species remain constant. Also, the temperature in solid is assumed to be uniform and as one local point of particle reaches ignition temperature, the whole particle ignites. This can be justified regarding the high thermal conductivity in metal particles
- We assume a particle shrinks as it burns and it leaves an extremely porous product (rust), which allows complete diffusion of oxidizer throughout the remaining un-oxidized particle. Though, this assumption is not valid if the product is very

dense, where we would need to take diffusion of oxidizer into solid phase (particle+product) into account.

We are going to solve the mass balance equation for this problem in general below, and specialize it at the end to small and large particles. To do so, one must notice that there are two zones in which the mass balance equation should be solved: inside the layer surrounding a particle which is called Kundsen layer ($r_p < r < r_\delta$) and outside of this layer ($r_\delta < r < r_\infty$), where r_p , and $r_\delta = r_p + \delta$ are the radius of particle and the Kundsen layer, respectively. However, since δ is the molecular mean free path (nanometer) and the particle's radius is in order of micrometer, we can assume $r_\delta \sim r_p$ and solve mass balance equation for range of $r_p < r < r_\infty$. The mass flow rate within this region is only due to the reaction (oxidizer consumption), and there is no other source and /or sink of mass. Hence, we write the mass balance equation for the particle in the spherical coordinate as

$$\frac{dm_{\text{ox}}}{dt} = -4\pi r_p^2 D_{\text{ox}} \frac{dC_{\text{ox}}}{dr}. \quad (\text{A.2})$$

where C_{ox} is oxidizer concentration, and D_{ox} is the mass diffusivity. We take the integral from both sides of Eq. (A.2) from r_p to r_∞ , and consider the following boundary conditions for concentration,

$$\left\{ \begin{array}{l} C_{\text{ox}}(r = r_\infty) = C_{\text{ox}}^o \\ C_{\text{ox}}(r = r_p) = C_{\text{ox},r_p}, \end{array} \right. \quad (\text{A.3})$$

where the amount of oxidizer in bulk is represented by C_{ox}^o , the concentration difference on the surface of particle is given by

$$\frac{(dm_{\text{ox}}/dt)}{4\pi r_p D_{\text{ox}}} = C_{\text{ox}}^o - C_{\text{ox},r_p}, \quad (\text{A.4})$$

which can also be written in the following form

$$\frac{(dm_{\text{ox}}/dt)}{4\pi r_p^2 D_{\text{ox}}/r_p} = (C_{\text{ox}}^o - C_{\text{ox},r_p}). \quad (\text{A.5})$$

Therefore the mass flow rate, $W = (dm_{\text{ox}}/dt)/(4\pi r_p^2)$ [kg/m²s], becomes

$$W = \beta (C_{\text{ox}}^o - C_{\text{ox},r_p}). \quad (\text{A.6})$$

where $\beta = D_{\text{ox}}/r_p$ is defined as the mass transfer rate ($[\beta] = \text{m/s}$).

In general, the mass transfer rate is a function of radius of particle; for large (small) particles β is small (large). Since W is solely due to the surface reaction we can also write

$$W \left(\equiv \frac{1}{4\pi r_p^2} \frac{dm_{\text{ox}}}{dt} \right) = \beta (C_{\text{ox}}^o - C_{\text{ox},r_p}) = K(T_s) C_{\text{ox},r_p}, \quad (\text{A.7})$$

Using this equation, it is straightforward to relate the amount of oxidizer on the surface of particle to that of bulk as

$$C_{\text{ox},r_p} = \frac{\beta}{\beta + K(T)} C_{\text{ox}}^o. \quad (\text{A.8})$$

By inserting Eq. (A.8) into Eq. (A.4), the oxidizer mass burning becomes

$$\frac{dm_{\text{ox}}}{dt} = K_{\text{eff}} C_{\text{ox}}^o (4\pi r_p^2) \quad (\text{A.9})$$

The effective reaction rate K_{eff} is defined as $D_a^* \beta$, where $D_a^* = \frac{K(T_s)}{K(T_s) + \beta}$ is the dimensionless Damköhler parameter which is a function of particle's radius (through the β term).

K_{eff} describes the reaction mechanism of particle during its combustion. When the particle radius is large (at $t = 0$) mass transfer towards particle is small and reaction is kinetic-limited. The rate of combustion is slowly increases with temperature until the surface temperature reaches T_{ign} . At this time the temperature of solid particle becomes much larger than surrounding gas and the reaction rate on the surface, since it is highly temperature dependent, becomes very fast. Thus $\beta \ll K(T_s)$ gives $D_a^* \sim 1$ and the reaction becomes diffusion-limited whose rate is given by $K_{\text{eff}} \sim \beta$. As the reaction progresses, radius of particle shrinks and β gets larger ($\beta \propto 1/r$). However, this combustion process for large particle occurs slowly that D_a^* and thus K_{eff} can be assumed constant. As the particle size becomes smaller than a critical value, β becomes large and D_a^* approaches a very small value ($K(T_s)/\beta$) that yields $K_{\text{eff}} \sim K(T_s)$ i.e. the combustion becomes kinetic-limited. This transition from diffusion-limited to kinetic-limited occurs below certain radius of particles, critical radius r_{cr} .

The “combustion time” of a large particle is the time during which the particle is pre-heated until it ignites plus the reaction time after ignition. We will show that the reaction time of particle is a function of its initial radius which implies that large particles burn slower and longer in time and release more heat than smaller ones. Also it indicates that for very small particles, reaction always is kinetic-limited. The authors of [166] in their numerical work show that below some range of particle radius, particles do not experience ignition.

By using the mass burning rate of oxidizer for one particle (Eq. (A.9)), and taking the chemical stoichiometric coefficient γ into account, one can find the consumption rate of a particle by

$$\frac{dm_p}{dt} = -\gamma K_{\text{eff}} C_{\text{ox}}^o (4\pi r_p^2), \quad (\text{A.10})$$

and the rate of a particle's radius decay reads

$$\frac{dr_p}{dt} = -\frac{\gamma K_{\text{eff}} C_{\text{ox}}^o}{\rho_s}, \quad (\text{A.11})$$

where we used $m_p(t) = \rho_s V_p(t)$, ρ_s is density of solid fuel, and V_p is the volume (surface area in 2D) of a particle. By defining the degree of conversion for particle η as

$$\eta = \frac{m_p(0) - m_p(t)}{m_p(0)}, \quad (\text{A.12})$$

the conversion rate using Eq. (A.10) can be written in the following form

$$\frac{d\eta}{dt} = \frac{3\gamma K_{\text{eff}} C_{\text{ox}}^o r_p^2}{\rho_s r_o^3} \quad (\text{A.13})$$

where r_o is the particle's radius at time of ignition. By using the definition of $K_{\text{eff}} = D_a^* \beta = (D_a^* D)/r_p$, Eq. (A.13) in 3D gives,

$$\frac{d\eta}{dt} = \frac{3\gamma D_{\text{ox}} C_{\text{ox}}^o D_a^*}{\rho_s r_o^2} \left(\frac{r_p(t)}{r_o} \right)^{L-2}, \quad (\text{A.14})$$

or in general

$$\frac{d\eta}{dt} = \frac{L\gamma D_{\text{ox}} C_{\text{ox}}^o D_a^*}{\rho_L r_o^2} \left(\frac{r_p(t)}{r_o} \right)^{L-2}. \quad (\text{A.15})$$

where L is a dimension of the problem, and ρ_L is the density of solid fuel in this dimension.

By defining combustion time as $t_R^* = \int_0^{t_R^*} D_a^* H(t' - t_{\text{ign}}) dt' = \frac{\rho_L r_o^2}{L \gamma D C_{\text{ox}}^o}$, the final form of Eq. (A.15) becomes

$$\frac{d\eta}{dt} = \frac{D_a^*}{t_R^*} \left(\frac{r_p(t)}{r_o} \right)^{L-2}. \quad (\text{A.16})$$

where $t_{\text{ign}}(\vec{x})$ is the time at which the local position on the surface of a particle, \vec{x} , ignites. As pointed out earlier, the limits of Damköhler parameter (or equivalently K_{eff}) reflects the transition of particle combustion from kinetic-limited to diffusion-limited; It becomes unity shortly after particle ignition and remains almost constant for duration of particle combustion. It eventually approaches zero after particle's burnout ($r_p < r_{\text{cr}}$). This behaviour thus can be represented by a Heaviside functions $H(t_R^* - (t - t_{\text{ign}}))$. The functionality of D_a^* can be derived precisely by solving the equations of gas and solid temperature coupled to that of oxidizer concentration [166]. Therefore by inserting the Heaviside form of D_a^* in Eq. (A.16), the conversion rate for $L = 2$ becomes

$$\frac{d\eta}{dt} = \frac{1}{t_R^*} H(t_R^* - (t - t_{\text{ign}})). \quad (\text{A.17})$$

According to Eq. (A.17) the rate of particle combustion in 2D (disks) is constant, assuming that enough oxidizer available to burn the particle. This is also consistent with our definition of the combustion time of a particle. According to its definition, t_R^* , varies directly with the square of particle's radius. For small particles, where reaction is kinetic-limited, however, combustion time of the particle is proportional to its radius. Therefore, large particles (in the diffusion-limited regime), have relatively long combustion time and their radius shrinks slowly over time. Therefore, we can assume that the reaction rate of combustion, on average, is constant .

So far we have assumed that the change of oxidizer concentration on the surface of particle is only due to the surface reaction according to Eq. (A.8). This assumption is not always valid as the local concentration around the particle may vary either due to the presence of other particles (for instance in fuel-rich mixtures where the reaction starves from oxidizer) or due to mass diffusivity of oxidizer (i.e. finite Le). Therefore we shall represent oxidizer concentration at the surface of particle, in general, by a concentration field $C_{ox}(\vec{x}, t)$ that can change locally in space and time.

We next specialize the reaction rate of a particle for different reaction orders and in different limits of mass diffusivity.

A.1.1 Combustion of cloud of particles

To derive a more realistic relation for particle combustion, we need to relax the assumption of an isolated particle and consider the effects of the cloud of particles on the rate of reaction of one particle (Eq. A.17) through assuming different reaction kinetics (referred to by the “reaction orders” $n = 1, 0$ in the text) and/or different limits of mass diffusivity (i.e. finite and infinite Lewis number). The modified reaction rate, then will be used to derive heat and mass balance equations for the coupled PDE of the master model for both continuum and discrete case.

- **The limit $n = 0$; $\text{Le} \rightarrow \infty$**

In the $n = 0$ limit, where amount of oxidizer in the bulk is sufficient to allow fuel particles to react completely, and in the absence of mass diffusivity, the concentration of oxidizer in the vicinity of the particles is constant and is equal to its value in bulk (or at least its

gradient on the surface of particle is negligible). In this situation particles can effectively burn independently. This means the reaction time of one particle in a cloud of particles is equal to that of a single particle Eq. (A.17).

- **The limit $n = 0$; Le finite**

When oxidizer diffusion is rate limiting, the amount of oxidizer in the vicinity of particles is less than the bulk value ($C_{ox} < C_{ox}^o$) and depends on mass diffusivity D_{ox} . In this situation, the local oxidizer, should appear in the reaction rate. To find the functional form of oxidizer's concentration in the vicinity of particles, one can use the steady-state solution of concentration ϕ_{ox} by solving Eqs. (2.4) for zero-order ($n = 0$) continuum combustion. These solutions in a co-moving frame, ($\xi = x - u t$, u is the normal velocity of a planar front), can be written in the following form,

$$\phi_{ox}(\xi) = \begin{cases} 1 + \frac{[1 - \exp(\text{Le } R)] \exp(-\text{Le } \xi)}{\text{Le } R \exp(\text{Le } R)} & \xi \geq 0 \\ \frac{1 - \exp(\text{Le } (R + \xi))}{\text{Le } R \exp(\text{Le } (R + \xi))} + \frac{R + \xi}{R} & -R \leq \xi < 0 \\ 0 & \xi < -R \end{cases} \quad (\text{A.18})$$

where R is the dimension-less reaction zone, over which the concentration is depleted after ignition time, and is derived from the self-consistency relation

$$\theta_{\text{ign}} = \frac{1 - \exp(-R)}{R} \quad (\text{A.19})$$

Equations. (A.18-A.19) are derived in [22]. Linearizing Eq. (A.19) in terms of the small parameter R , substituting it into Eq. (A.18) and evaluating the result at the position of front ($\xi = 0$) gives

$$\phi_{\text{ox}}(\xi = 0) = 1 + \frac{1 - \exp(2\text{Le}(1 - \theta_{\text{ign}}))}{2\text{Le}(1 - \theta_{\text{ign}}) \exp(2\text{Le}(1 - \theta_{\text{ign}}))} \quad (\text{A.20})$$

Replacing $\phi_{\text{ox}}(\xi = 0)$ by $C_{\text{ox}}/C_{\text{ox}}^{\text{o}}$, and using the relation $\overline{\text{Le}} = 2\text{Le}(1 - \theta_{\text{ign}})$, we arrive at

$$C_{\text{ox}} = C_{\text{ox}}^{\text{o}} \left[1 + \frac{1 - \exp(\overline{\text{Le}})}{\overline{\text{Le}} \exp(\overline{\text{Le}})} \right] \quad (\text{A.21})$$

for the oxidizer concentration which allows us to specialize Eq. (A.15) to the following form for this limit,

$$\frac{d\eta}{dt} = \frac{L \gamma D_{\text{ox}} C_{\text{ox}}^{\text{o}} (1 + G) D_a^*}{\rho_L r_o^2} \left(\frac{r_p}{r_o} \right)^{L-2} \quad (\text{A.22})$$

where $G = (1 - \exp(\overline{\text{Le}})) / (\overline{\text{Le}} \exp(\overline{\text{Le}}))$. We note that in the limit of zero mass diffusivity, G term is zero and we recover Eq. (A.17) for ($n = 0$; $\text{Le} \rightarrow \infty$). Specifically, by defining new combustion time $t'_R = \frac{\rho_L r_o^2}{L \gamma D_{\text{ox}} C_{\text{ox}}^{\text{o}} (1+G)}$, Eq. (A.22) becomes

$$\frac{d\eta}{dt} = \frac{D_a^*}{t'_R} \left(\frac{r_p}{r_o} \right)^{L-2} \quad (\text{A.23})$$

Comparing new combustion time t'_R with the old one t_R^* , shows that $t'_R = \frac{1}{1+G} t_R^*$. This indicates that in the presence of mass diffusion, the combustion time of one particle is

smaller than that of one single particle. we can write Eq. (A.23) in 2D as

$$\frac{d\eta}{dt} = \frac{1}{t_R^*} H(\phi_{ox}(\vec{x}, t)), \quad (\text{A.24})$$

which is analogous to Eq. (A.17), except the Heaviside function in this limit is expressed in terms of available local oxidizer. The smaller reaction time of particle in this limit due to finite Lewis number, is implicitly represented by the Heaviside function.

- **The limit $n = 1$; $\text{Le} \rightarrow \infty$**

In the limit $n = 1$, when the amount of oxidizer in bulk is less than its stoichiometric value, particle combustion is slaved to local available concentration, even under condition of zero mass diffusivity. In this case, the concentration C_{ox} becomes a function of position and time ($C_{ox}(\vec{x}, t)$). Using this assumption the conversion rate of particle Eq. (A.15) becomes

$$\frac{d\eta}{dt} = \frac{L \gamma D_{ox} D_a^* C_{ox}(\vec{x}, t)}{\rho_L r_o^2} \left(\frac{r_p}{r_o} \right)^{L-2} \quad (\text{A.25})$$

By expressing $C_{ox}(\vec{x}, t) = \phi_{ox}(\vec{x}, t) C_{ox}^o$, Eq. (A.25) along with the combustion time definition $t_R^* = \rho_L r_o^2 / \gamma D_{ox} C_{ox}^o$, becomes (for dimension $L = 2$),

$$\frac{d\eta}{dt} = \frac{D_a^* \phi_{ox}(\vec{x}, t)}{t_R^*} \quad (\text{A.26})$$

This equation indicates that even though the combustion rate of an isolated particle, after ignition, is constant (which is specified by $D_a^* = H(t_R^* - (t - t_{ign}))$), it does follow the local oxidizer concentration $\phi_{ox}(\vec{x}, t)$. Hence it is better to re-write Eq. (A.26) in the following

form,

$$\frac{d\eta}{dt} = \frac{\phi_{\text{ox}}(\vec{x}, t)}{t_R^*} \quad (\text{A.27})$$

- **The limit $n = 1$; Le finite**

In this limit, not only the concentration of oxidizer in bulk is insufficient for the oxidation process, but also the local concentration is different from its bulk value because of the diffusion of mass. Similar to the limit ($n = 0$; Le finite), we use a steady-state solution of first-order ($n = 1$) reaction diffusion equations of the master model in the text. This gives (see Appendix B),

$$\phi_{\text{ox}}(\xi) = \begin{cases} \frac{1}{1 + \vartheta} \exp\left(\frac{u \vartheta}{D_{\text{ox}}} \xi\right) & \xi \leq 0 \\ \frac{-\vartheta}{1 + \vartheta} \exp\left(-\frac{u}{D_{\text{ox}}} \xi\right) + 1 & \xi > 0, \end{cases} \quad (\text{A.28})$$

where parameter ϑ and velocity u are defined as,

$$\left\{ \begin{array}{l} \vartheta = \frac{-1 + \sqrt{1 + \frac{4 D_{\text{ox}}}{u^2 t_r^*}}}{2}, \\ u = \sqrt{\frac{\alpha}{t_r^* \left(\frac{\theta_{\text{ign}}}{1 - \theta_{\text{ign}}} \right) \left(1 + \frac{1}{\text{Le}} \left(\frac{\theta_{\text{ign}}}{1 - \theta_{\text{ign}}} \right) \right)}}, \end{array} \right. \quad (\text{A.29})$$

By substituting the value of concentration at the position of a particle, $C_{\text{ox}}(\vec{x}, t)/C_{\text{ox}}^{\text{o}} = \phi_{\text{ox}}(\vec{x}, t)/(1 + \vartheta)$ into Eq. (A.15) for $L = 2$, and using the definition of combustion time

$t_R^* = \rho_L r_o^2 / \gamma D_{\text{ox}} C_{\text{ox}}^o$, we get

$$\frac{d\eta}{dt} = \frac{D_a^* \phi_{\text{ox}}(\vec{x}, t)}{(1 + \vartheta) t_R^*}, \quad (\text{A.30})$$

This equation indicates that the assumption of the constant-rate reaction for an isolated particle, represented by $D_a^* = H(t_R^* - (t - t_{\text{ign}}))$, does not hold for a particle in this limit. Furthermore, comparing Eq. (A.27) and Eq. (A.31) shows that the reaction rate of a particle in this limit is lower than that in the limit ($n = 1; \text{Le} \rightarrow \infty$) by a factor of $1/(1 + \vartheta)$, and by setting ϑ to zero (i.e. $D_{\text{ox}} = 0$) we recover Eq. (A.27). To simplify the notation, we absorb the factor $1/(1 + \vartheta)$ into $\phi_{\text{ox}}(\vec{x}, t)$, and re-write Eq. (A.30) as,

$$\frac{d\eta}{dt} = \frac{\phi_{\text{ox}}(\vec{x}, t)}{t_R^*} \quad (\text{A.31})$$

A.2 Derivation of combustion equations with heterogeneous random media

The interpretation of the reaction source in our master model depends on the ratio of heterogeneity scale to characteristic length of the flame front. In combustion of suspension of metal (solid) particles, the former is the average inter-particle distance. In this section we will derive more formally the reaction diffusion equations used in this thesis (i.e. the “master equations”) with discrete particle sources. This model was the starting point from which the “smoothed” continuum master model equations introduced in Chapter 2 and studied in Chapter 3. The continuum master model equations will be derived more thoroughly in the next appendix by using the results of this appendix. In what follows we

derive a general form of equations to describe discrete combustion regime. These equations then will be specialized for two different kinetics of reaction ($n = 0, 1$) and different limit of mass diffusivity ($\text{Le} \rightarrow \infty$ and Le finite).

In general, the combustion of solid metal particles in the presence of oxidizer gas can be described by the coupled equations of temperature $T(\vec{x}, t)$ and reaction-diffusion of oxidizer concentration $C_{\text{ox}}(\vec{x}, t)$ given by,

$$\begin{cases} \rho c_p \frac{\partial T(\vec{x})}{\partial t} = \kappa \nabla^2 T(\vec{x}) + Q W \\ \frac{\partial C_{\text{ox}}(\vec{x})}{\partial t} = D_{\text{ox}} \nabla^2 C_{\text{ox}}(\vec{x}) - \frac{1}{\gamma} W, \end{cases} \quad (\text{A.32})$$

where Q , κ , D_{ox} , ρ and c_p are the heat of reaction ([J/gr]), heat conductivity of the medium, mass diffusivity of oxidizer, density and specific heat capacity of the medium. The source term W is adjusted for the heterogeneity of a medium is defined by,

$$W = B \sum_i \frac{d\eta_i}{dt} H(T - T_{\text{ign}}) g(|\vec{x} - \vec{x}_i|, r_p), \quad (\text{A.33})$$

where B is the initial concentration of solid fuel, η is the conversion fraction of the particle whose rate for different limits of reaction kinetics (i.e. zero and first order kinetics) and mass diffusivity (i.e. Le finite, $\text{Le} \rightarrow \infty$) is already derived in the last section (Eqs. (A.17,A.24,A.31)), T_{ign} is the ignition temperature, $H(x)$ is the Heaviside step function. Here $g(|\vec{x} - \vec{x}_i|, r_p)$ is a normalized function with the properties of $g(|\vec{x} - \vec{x}_i| > r_p, r_p) = 0$ and $\int g(\vec{x} - \vec{x}_i, r_p) d\vec{x}$ over particle's volume is unity, where \vec{x}_i and r_p represent centre and radius of the particle i , respectively. This function is introduced to specify the spatial extent of a particle r_p , and can be defined as Heaviside function

$g_i(\vec{x}, r_p) = \frac{1}{V_p} H(r_p - |\vec{x} - \vec{x}_i|)$, where V_p is the initial volume (area in 2D) of a particle. By using the stoichiometric coefficient of the chemical reaction of metal particle oxidation γ , and definition of $g(|\vec{x} - \vec{x}_i|, r_p)$, we can re-write the source term W in terms of available oxidizer concatenation in bulk C_{ox}^{o} , as

$$W = \frac{\gamma C_{\text{ox}}^{\text{o}}}{V_p} \sum_i \frac{d\eta}{dt} H(T - T_{\text{ign}}) H(r_p - |\vec{x} - \vec{x}_i|). \quad (\text{A.34})$$

In the discrete limit it can be further assumed that the inter-particle spacing is at least one order of magnitude larger than their diameter. According to this assumption, it is possible to consider particles as point sources (each represented by a delta function) in space, while their reaction is extended in time. Thus, in the limit where the radius of particle tends to zero, $\lim_{r_p \rightarrow 0} \left(\frac{1}{V_p} H(r_p - |\vec{x} - \vec{x}_i|) \right) = \delta(\vec{x} - \vec{x}_i)$ and Eq. (A.34) becomes

$$W = \gamma C_{\text{ox}}^{\text{o}} \sum_i \frac{d\eta}{dt} H(T - T_{\text{ign}}) \delta(\vec{x} - \vec{x}_i). \quad (\text{A.35})$$

However, in this study we never consider this limit and particles are represented by 2D disks with radius r_p which are numerically resolved.

A.2.1 Deriving equations for discrete combustion in the limit of $n = 0$ and Le finite

Here, the reaction rate of particle combustion is calculated based on particles's geometry (spherical objects in 3D, and disks in 2D) and under diffusion-limited conditions where rate of oxidizer mass diffusion towards the particle is rate limiting (i.e. Le finite), and by assuming that the amount of oxidizer in the bulk is sufficient to allow fuel particles to react completely (i.e. $n = 0$).

To derive the equations in this limit, we insert Eq. (A.24) for the conversion rate of one particle in the limit of ($n = 0$; Le finite) and for a two-dimensional system into Eq. (A.34). Thus Eqs. (A.32) for temperature and oxidizer concentration become,

$$\left\{ \begin{array}{l} \frac{\partial T(\vec{x})}{\partial t} = \alpha \nabla^2 T(\vec{x}) + \\ \quad \frac{Q \gamma C_{\text{ox}}^o}{\rho c_p t_R^*} \sum_i \left[\frac{1}{V_p} H(\phi(\vec{x}, t)) H(T - T_{\text{ign}}) H(r_p - |\vec{x} - \vec{x}_i|) \right] \\ \\ \frac{\partial C_{\text{ox}}(\vec{x})}{\partial t} = D_{\text{ox}} \nabla^2 C_{\text{ox}}(\vec{x}) - \\ \quad \frac{C_{\text{ox}}^o}{t_R^*} \sum_i \left[\frac{1}{V_p} H(\phi(\vec{x}, t)) H(T - T_{\text{ign}}) H(r_p - |\vec{x} - \vec{x}_i|) \right] \end{array} \right. \quad (\text{A.36})$$

where $\alpha = \kappa / \rho c_p$ is the thermal diffusivity of the combustible medium (solid metal particles plus inert and oxidizer gas).

To make equations non-dimensional we use the characteristic length of heterogeneity d and the characteristic time $\tau = \frac{\alpha}{d^2}$, where d is the inter-particle spacing when particles are placed on a regular array. By introducing a dimension-less temperature $\theta = (T - T_o) / (T_{\text{ad}} - T_o)$, where $(T_{\text{ad}} - T_o)$ is equal to $Q \gamma C_{\text{ox}}^o / \rho c_p$, and dimension-less concentration of oxidizer $\phi_{\text{ox}}(\vec{x}, t) = C_{\text{ox}}(\vec{x}, t) / C_{\text{ox}}^o$, where C_{ox}^o is the oxidizer concentration in the bulk, and using characteristic time and length defined above, the non-dimensional form of Eq. (A.36)

reads,

$$\left\{ \begin{array}{l} \frac{\partial \theta(\vec{x})}{\partial t} = \nabla^2 \theta(\vec{x}) + \frac{1}{V_p} \sum_i A \left[H(\phi(\vec{x}, t)) H(\theta - \theta_{ign}) H(r_p - |\vec{x} - \vec{x}_i|) \right] \\ \frac{\partial \phi_{ox}(\vec{x})}{\partial t} = \frac{1}{Le} \nabla^2 \phi_{ox}(\vec{x}) - \frac{1}{V_p} \sum_i A \left[H(\phi_{ox}(\vec{x}, t)) H(\theta - \theta_{ign}) H(r_p - |\vec{x} - \vec{x}_i|) \right], \end{array} \right. \quad (A.37)$$

where $A = d^2/(\alpha t_R^*)$ is the dimension-less constant.

A.2.1.1 Deriving equations for discrete combustion in the limit of $n = 0$ and $Le \rightarrow \infty$

In the combustion regime with zero-order kinetics (denoted by $n = 0$) and in the absence of mass diffusion (i.e. $Le \rightarrow \infty$), the local concentration of oxidizer is constant and equal to the bulk value C_{ox}^o . In this case, the combustion rate of a particle in cloud of particles, is equal to combustion rate of an isolated particle, and the combustion system can only be described by the equation for the local temperature. By inserting the conversion rate of one particle Eq. (A.17) into Eq. (A.34), the non-dimensional form of Eqs. (A.32) gives,

$$\frac{\partial \theta(\vec{x})}{\partial t} = \nabla^2 \theta(\vec{x}) + \frac{1}{V_p} \sum_i A \left[H\left(\frac{1}{A} - (t - t_{ign})\right) H(\theta - \theta_{ign}) H(r_p - |\vec{x} - \vec{x}_i|) \right] \quad (A.38)$$

where $A = d^2/(\alpha t_R^*)$ as before. When the radius of a particle tends to zero, the expression $(1/V_p) H(r_p - |\vec{x} - \vec{x}_i|)$ can be replaced by $\delta(\vec{x} - \vec{x}_i)$, and Eq. (A.38) becomes,

$$\frac{\partial \theta(\vec{x})}{\partial t} = \nabla^2 \theta(\vec{x}) + \sum_i A \left[H\left(\frac{1}{A} - (t - t_{ign})\right) H(\theta - \theta_{ign}) \delta(\vec{x} - \vec{x}_i) \right], \quad (A.39)$$

which is called *discrete box model*. The complete analysis of this model both in 1D and 2D are given in [172, 15, 14].

A.2.2 Deriving equations for discrete combustion in the limit of $n = 1$ for both Le finite and $\text{Le} \rightarrow \infty$

In this limit, since the concentration of oxidizer in the bulk is not sufficient to combust the solid metal particles completely, the reaction rate of a particle depends on the local concentration, whether the mass diffusion is zero or not. By substituting the conversion rate of particle for first-order kinetics (Eq. A.31) into the source term W given by Eq. (A.34), and applying the same discussions for the zero-order case, the dimension-less equations for the combustion system is derived as,

$$\left\{ \begin{array}{l} \frac{\partial \theta(\vec{x})}{\partial t} = \nabla^2 \theta(\vec{x}) + \\ \qquad \frac{1}{V_p} \sum_i A \left[H(\theta - \theta_{\text{ign}}) H(r_p - |\vec{x} - \vec{x}_i|) \phi_{\text{ox}}(\vec{x}, t) \right] \\ \\ \frac{\partial \phi_{\text{ox}}(\vec{x})}{\partial t} = \frac{1}{\text{Le}} \nabla^2 \phi_{\text{ox}}(\vec{x}) - \\ \qquad \frac{1}{V_p} \sum_i A \left[H(\theta - \theta_{\text{ign}}) H(r_p - |\vec{x} - \vec{x}_i|) \phi_{\text{ox}}(\vec{x}, t) \right]. \end{array} \right. \quad (\text{A.40})$$

Equations (A.40) in the limit ($\text{Le} \rightarrow \infty$) reduce to,

$$\left\{ \begin{array}{l} \frac{\partial \theta(\vec{x})}{\partial t} = \nabla^2 \theta(\vec{x}) + \frac{1}{V_p} \sum_i A \left[H(\theta - \theta_{\text{ign}}) H(r_p - |\vec{x} - \vec{x}_i|) \phi_{\text{ox}}(\vec{x}, t) \right] \\ \\ \frac{\partial \phi_{\text{ox}}(\vec{x})}{\partial t} = - \frac{1}{V_p} \sum_i A \left[H(\theta - \theta_{\text{ign}}) H(r_p - |\vec{x} - \vec{x}_i|) \phi_{\text{ox}}(\vec{x}, t) \right], \end{array} \right. \quad (\text{A.41})$$

The non-dimensional equations for discrete combustion with two different reaction kinetics ($n = 0, 1$) and in the limit of non-zero mass diffusivity (i.e. Le finite) can be written in the closed form below

$$\begin{cases} \frac{\partial \theta(\vec{x})}{\partial t} = \nabla^2 \theta(\vec{x}) + W_n \\ \frac{\partial \phi_{\text{ox}}(\vec{x})}{\partial t} = \frac{1}{\text{Le}} \nabla^2 \phi_{\text{ox}}(\vec{x}) - W_n, \end{cases} \quad (\text{A.42})$$

where the source term W_n is given by,

$$W_n = \sum_i A \phi^{(n)} \left[H(\theta(\vec{x}, t) - \theta_{\text{ign}}) H^{(1-n)}(\phi(\vec{x}, t)) g(|\vec{x} - \vec{x}_i| - r_p) \right], \quad n = 0, 1 \quad (\text{A.43})$$

Equations (A.42-A.43) are referred to in the text as the *discrete master model*.

Appendix B

Derivation of effective medium version of discrete combustion equations, and the derivation of the Continuum Master Equations

Here we derive reaction-diffusion equations describing a combustion front propagation in random discrete media, by using *effective* medium approach. For this purpose we use the equations for combustion of cloud of particles in the discrete limit that are already derived in Appendix A. The effective parameters for reaction rate, and thermal/mass diffusivity in a random discrete media will be obtained. These parameters are used in Chapter 4 to study the combustion front propagation in random media. The calculations presented here then will be employed to derive master model in the continuum limit in the next section.

B.1 Effective medium derivation

The *effective* coupled Reaction-diffusion equations describing the combustion of solid metal particles with ignition temperature kinetics, and neglecting solid fuel diffusion, can be derived by coarse-graining over distances that are large compared to the sizes of the heterogeneity. To do so, we use the coupled equations of local temperature $T(\vec{x}, t)$ and reaction-diffusion of oxidizer concentration $C_{\text{ox}}(\vec{x}, t)$, describing the combustion system in random heterogenous media, and are given by Eqs. (A.32-A.34) in Appendix A. By coarse-graining over a length of interest which is much larger than inter-particle spacing, one can write,

$$\begin{cases} \rho c_p \frac{\partial \langle T(\vec{x}) \rangle}{\partial t} = \langle \kappa \nabla^2 T(\vec{x}) \rangle + Q \langle W(C_{\text{ox}}) \rangle \\ \frac{\partial \langle C_{\text{ox}}(\vec{x}) \rangle}{\partial t} = \langle D_{\text{ox}} \nabla^2 C_{\text{ox}}(\vec{x}) \rangle - \frac{1}{\gamma} \langle W(C_{\text{ox}}) \rangle, \end{cases} \quad (\text{B.1})$$

where Q , κ , D_{ox} , γ , ρ and c_p are the heat of reaction ([J/gr]), heat conductivity of the medium, mass diffusivity of oxidizer, stoichiometric coefficient of chemical oxidation reaction , density and specific heat capacity of the medium. In Eqs. (B.1), volume-averaged quantities are denoted by $\langle \cdot \rangle$.

The source term W is adjusted for the heterogeneity of a medium is defined by,

$$\langle W(C_{\text{ox}}) \rangle \approx W^e = \Phi_s W(\langle C_{\text{ox}} \rangle) \quad (\text{B.2})$$

In deriving this equation we assume the length-scale of heterogeneity is much smaller than the distance that oxidizer diffuses in the mean reaction time. In this case reaction occurs homogeneously between oxidizer and particles within a course-grained volume and spatial inhomogeneity only arises on scales larger than the length of interest.

As we assume in derivation of particle combustion in Appendix A, the change in oxidizer diffusion in the presence of solid particles are negligible and thus one can write $D^e = D_{\text{ox}}$. The assumption of constant D_{ox} is only valid if particles as they burn (oxidize) leave an extremely porous product (rust), which allows complete diffusion of oxidizer throughout the remaining un-oxidized particles.

The effective heat conductivity of a random medium, where solid particles represented by 2D impenetrable disks with thermal conductivity κ_s and area fraction Φ_s are dispersed in a gaseous phase with thermal conductivity κ_g , can be written as

$$\frac{\kappa^e}{\kappa_g} = f(\Phi_s) = 1 + 2\Phi_s + 2\Phi_s^2. \quad (\text{B.3})$$

where κ^e denotes the effective conductivity of a medium (mixture of solid and gaseous phases). We should note that in deriving Eq. (B.3) the conductivity of solid inclusions is

assumed to be much larger than that of the gaseous phase $\kappa_s \gg \kappa_g$. To obtain Eq. (B.3) we use the analytical expression derived by Choy et al. [30] for 2D inclusions phase 2 in a background medium phase 1.

By performing coarse-graining and using the effective parameters above, Eqs. (B.1) transfer to

$$\begin{cases} \frac{\partial \langle T(\vec{x}) \rangle}{\partial t} = \alpha^e \nabla^2 \langle T(\vec{x}) \rangle + \frac{Q}{\rho c_p} W^e \\ \frac{\partial \langle C_{\text{ox}}(\vec{x}) \rangle}{\partial t} = D_{\text{ox}} \nabla^2 \langle C_{\text{ox}}(\vec{x}) \rangle - \frac{1}{\gamma} W^e, \end{cases} \quad (\text{B.4})$$

where $\alpha^e = \kappa^e / \rho c_p$ and W^e are the effective thermal conductivity and effective reaction rate, respectively. The effective reaction W^e can be written as $\Phi_s B_{\text{st}} (d\eta/dt) H(T - T_{\text{ign}})$, where B_{st} is the stoichiometric value of solid fuel concentration. We define $B = \Phi_s B_{\text{st}}$ as the initial concentration of solid fuel in a coarse-grained volume. In the continuum limit we set Φ_s to 1 and thus $B = B_{\text{st}}$. The area fraction Φ_s in the reaction term adjust the rate of reaction (heat generation) based on the initial concentration of solid metal particles in the coarse-grained volume.

By introducing a dimension-less temperature $\theta = (T - T_o)/(T_{\text{ad}} - T_o)$, where $(T_{\text{ad}} - T_o)$ is equal to $Q B_{\text{st}} / \rho c_p$, and dimension-less concentration of oxidizer $\phi_{\text{ox}}(\vec{x}, t) = C_{\text{ox}}(\vec{x}, t) / C_{\text{ox}}^o$, where C_{ox}^o is the oxidizer concentration in the bulk, Eqs. B.4, after dropping the averaging operator $\langle \rangle$, can be re-cast as,

$$\begin{cases} \frac{\partial \theta(\vec{x})}{\partial t} = \alpha^e \nabla^2 \theta(\vec{x}) + \Phi_s \frac{d\eta}{dt} H(\theta - \theta_{\text{ign}}) \\ \frac{\partial \phi_{\text{ox}}(\vec{x})}{\partial t} = D_{\text{ox}} \nabla^2 \phi_{\text{ox}}(\vec{x}) - \Phi_s \frac{d\eta}{dt} H(\theta - \theta_{\text{ign}}). \end{cases} \quad (\text{B.5})$$

The effective Lewis number in random media Le^e , by using Eq. (B.3), is given by

$$\text{Le}^e = \frac{\alpha^e}{D_{\text{ox}}} = f(\Phi_s) \frac{\alpha_g}{D_{\text{ox}}}, \quad (\text{B.6})$$

where $\alpha_g = \kappa_g / \rho c_p$ is the thermal diffusivity of a medium without solid phase. By setting $\Phi_s = 1$ in Eq. (B.6), the effective Lewis number in the continuum limit obtained as $\text{Le}^e(\Phi_s = 1)$. To simplify the notation we drop superscript and the argument and let Le stands for the Lewis number in the continuum limit. The effective Lewis number in random media Le^e thus can be written in terms of its value in the continuum limit Le and area fraction of solid particles in random media Φ_s ,

$$\text{Le}^e(\Phi_s) = \frac{f(\Phi_s)}{f(\Phi_s = 1)} \text{Le}. \quad (\text{B.7})$$

The Eq. (B.7) asserts that the Lewis number in the random medium is effectively less than its value in the continuum limit.

B.1.1 Master model derivation

In this section we show the details of the derivation of the Master model equations for the case of first-order kinetics in the continuum limit. Derivation for zero-order case is analogous. This master model equations were presented in Chapter 2 and are used to study the cellular pattern formation in Chapter 3.

The coupled equations for temperature and oxidizer concentration in the continuum limit can be derived by setting Φ_s to unity in Eqs. (B.5) for effective medium, in the

following from

$$\begin{cases} \frac{\partial \theta(\vec{x})}{\partial t} = \alpha \nabla^2 \theta(\vec{x}) + \frac{d\eta}{dt} H(\theta - \theta_{ign}) \\ \frac{\partial \phi_{ox}(\vec{x})}{\partial t} = D_{ox} \nabla^2 \phi(\vec{x}) - \frac{d\eta}{dt} H(\theta - \theta_{ign}), \end{cases} \quad (\text{B.8})$$

where we replaced the effective thermal diffusivity α^e by α . By inserting the conversion rate of particles $d\eta/dt$ in the limit ($n = 1$; Le finite) which is given by Eq. (A.31) in Appendix A, into Eqs. (B.8) we get

$$\begin{cases} \frac{\partial \theta(\vec{x})}{\partial t} = \alpha \nabla^2 \theta(\vec{x}) + \frac{\phi_{ox}(\vec{x})}{t_R^*} H(\theta - \theta_{ign}) \\ \frac{\partial \phi_{ox}(\vec{x})}{\partial t} = D_{ox} \nabla^2 \phi(\vec{x}) - \frac{\phi_{ox}(\vec{x})}{t_R^*} H(\theta - \theta_{ign}), \end{cases} \quad (\text{B.9})$$

where the combustion time of a particle $t_R^* = \rho_L r_o^2 / (L \gamma D_{ox} C_{ox}^o)$ was defined in A.1.1. It is instructive to re-scale length and time in Eq. B.9 by the transformations

$$\delta_c = \frac{\alpha}{u} \quad , \quad \tau = \frac{\alpha}{u^2}, \quad (\text{B.10})$$

where u is the characteristic velocity of a planar front. This leads to the dimension-less form of Eqs. (B.9) given by

$$\begin{cases} \frac{\partial \theta(\vec{x})}{\partial t} = \nabla^2 \theta(\vec{x}) + \frac{\tau}{t_R^*} \phi_{ox}(\vec{x}) H(\theta - \theta_{ign}) \\ \frac{\partial \phi_{ox}(\vec{x})}{\partial t} = \frac{1}{Le} \nabla^2 \phi_{ox} - \frac{\tau}{t_R^*} \phi_{ox}(\vec{x}) H(\theta - \theta_{ign}) \end{cases} \quad (\text{B.11})$$

Introducing $A = \tau/t_R^*$, Eqs. (B.11) take the final form,

$$\begin{cases} \frac{\partial\theta(\vec{x})}{\partial t} = \nabla^2\theta(\vec{x}) + W \\ \frac{\partial\phi_{\text{ox}}(\vec{x})}{\partial t} = \frac{1}{\text{Le}}\nabla^2\phi_{\text{ox}}(\vec{x}) - W, \end{cases} \quad (\text{B.12})$$

with the source term

$$W = \begin{cases} A\phi_{\text{ox}}(\vec{x})H(\theta - \theta_{\text{ign}}) & \text{for } n = 1 \\ A H(\theta - \theta_{\text{ign}})H(\phi_{\text{ox}}) & \text{for } n = 0 \end{cases} \quad (\text{B.13})$$

To calculate u in Eq. (B.10), we need first to obtain the steady-state solutions by transforming Eqs. (B.9) to the co-moving coordinate $\xi = x - ut$, and set the time derivatives to zero. By finding and match the solutions for temperature and concentration in either side of interface (at $\xi = 0$), and using following far-field,

$$\theta(+\infty) = 0, \quad \theta(-\infty) = 1, \quad (\text{B.14})$$

$$\phi_{\text{ox}}(+\infty) = 1, \quad \phi_{\text{ox}}(-\infty) = 0,$$

and continuity conditions of the fields and their derivatives across the interface ($\xi = 0$),

$$\begin{aligned} [\theta] &= 0 & [\phi_{\text{ox}}] &= 0 \\ \left[\frac{d\theta}{d\xi} \right] &= 0 & \left[\frac{d\phi_{\text{ox}}}{d\xi} \right] &= 0, \end{aligned} \quad (\text{B.15})$$

where $[\cdot]$ denotes a jump across the interface, it is straightforward to derive the steady-state solutions for the temperature,

$$\theta^{ss}(\xi) = \begin{cases} \frac{-1}{\alpha t_R^* u^2 (1 + \vartheta) (\frac{\vartheta}{D_{ox}})^2 + \frac{\vartheta}{D_{ox}}} \exp \left[\frac{u(-1 + \vartheta)}{D_{ox}} \xi \right] & \xi \leq 0 \\ \theta_{ign} \exp \left[-\frac{u}{\alpha} \xi \right] & \xi > 0, \end{cases} \quad (B.16)$$

and for the concentration,

$$\phi_{ox}^{ss}(\xi) = \begin{cases} \frac{1}{1 + \vartheta} \exp \left[\frac{u \vartheta}{D_{ox}} \xi \right] & \xi \leq 0 \\ \frac{-\vartheta}{1 + \vartheta} \exp \left[-\frac{u}{D_{ox}} \xi \right] + 1 & \xi > 0, \end{cases} \quad (B.17)$$

where

$$\vartheta = \frac{-1 + \sqrt{1 + \frac{4D_{ox}}{u^2 t_R^*}}}{2}, \quad (B.18)$$

using the continuity conditions for temperature across the interface, $\theta^{ss}(\xi = 0^+) = \theta^{ss}(\xi = 0^-) = \theta_{ign}$, gives the steady-state velocity as,

$$u = \sqrt{\frac{\alpha}{t_R^* \left(\frac{\theta_{ign}}{1 - \theta_{ign}} \right) \left(1 + \frac{1}{Le} \left(\frac{\theta_{ign}}{1 - \theta_{ign}} \right) \right)}}. \quad (B.19)$$

Appendix C
Linear Stability Analysis for Master Model equations with dissipation

C.1 Deriving steady-state solutions and dispersion relation for dissipative combustion model

This appendix section shows the derivation of the steady-state solution and dispersion relation for dissipative first-order combustion model, in the continuum limit of solid fuel sources. Derivation of zero-order case can be done in an analogous way. The combustion system we proposed in the text to describe combustion in the presence of heat dissipation through its boundaries in the form of newtonian cooling (using Eqs. 2.4) is described by

$$\begin{cases} \rho c_p \frac{\partial T}{\partial t} = \kappa \nabla^2 T + Q W - \Upsilon (T - T_o) \\ \frac{\partial C_{ox}(\vec{x})}{\partial t} = D_{ox} \nabla^2 C_{ox}(\vec{x}) - \frac{W}{\gamma}, \end{cases} \quad (\text{C.1})$$

where the parameter Υ is a constant coefficient that measures the intensity of heat loss [W/m^3K]. By introducing a dimension-less temperature $\theta = (T - T_o)/(T_{ad} - T_o)$, and a dimensionless oxidizer concentration $\phi_{ox}(\vec{x}, t) = C_{ox}(\vec{x}, t)/C_{ox}^o$, and by employing following transformation for length and time

$$\delta_c = \frac{\alpha}{u} , \quad \tau = \frac{\alpha}{u^2}, \quad (\text{C.2})$$

where u is the steady-state velocity of a planar front, Eqs. (C.1) can be written in the following form,

$$\begin{cases} \frac{\partial \theta}{\partial t} = \nabla^2 T + W - \Gamma \theta \\ \frac{\partial \phi_{ox}}{\partial t} = \frac{1}{Le} \nabla^2 \phi_{ox} - W, \end{cases} \quad (\text{C.3})$$

where $\Gamma = \Upsilon\tau/\rho c_p$ is the dimension-less heat dissipation rate. Writing the steady-state form of Eqs. (C.3) in a co-moving frame, and rearranging, gives

$$\left\{ \begin{array}{l} \frac{\partial^2\theta}{\partial\xi^2} + u\frac{\partial\theta}{\partial\xi} + \frac{\partial^2\theta}{\partial y^2} - \Gamma\theta + W = 0 \\ \frac{1}{Le}\frac{\partial^2\phi_{ox}}{\partial\xi^2} + u\frac{\partial\phi_{ox}}{\partial\xi} + \frac{1}{Le}\frac{\partial^2\phi_{ox}}{\partial y^2} - W = 0. \end{array} \right. \quad (C.4)$$

Rewriting Eq. (C.4) on either side of the interface ($\xi = 0$) (i.e. preheat zone where $W = 0$, and combustion zone where $W \neq 0$) gives,

$$\left\{ \begin{array}{ll} \frac{\partial^2\theta}{\partial\xi^2} + u\frac{\partial\theta}{\partial\xi} - \Gamma\theta + W = 0 & \xi \leq 0 \\ \frac{\partial^2\theta}{\partial\xi^2} + u\frac{\partial\theta}{\partial\xi} - \Gamma\theta = 0, & \xi > 0 \end{array} \right. \quad (C.5)$$

for dimensionless temperature, and for concentration,

$$\left\{ \begin{array}{ll} \frac{1}{Le}\frac{\partial^2\phi_{ox}}{\partial\xi^2} + u\frac{\partial\phi_{ox}}{\partial\xi} - W = 0 & \xi \leq 0 \\ \frac{1}{Le}\frac{\partial^2\phi_{ox}}{\partial\xi^2} + u\frac{\partial\phi_{ox}}{\partial\xi} = 0, & \xi > 0 \end{array} \right. \quad (C.6)$$

where

$$W = A\phi_{ox}^n = A\phi_{ox}, \quad \text{if } \theta \geq \theta_{ign} \text{ and } n = 1, \quad (C.7)$$

where A is derived below. It is noteworthy that this calculation assumes that the dissipation is small enough the we still can use two zone system instead of three. Otherwise, the temperature and concentration field both have to be solved for three preheat, combustion

and product zone, and the solutions in each of these zones matched at the boundary of each zone.

We next solve Eqs. (C.5-C.6) in each zone, and apply the following conditions for fields and their derivatives,

$$\begin{aligned} [\theta] &= 0 & [\phi_{\text{ox}}] &= 0 \\ \left[\frac{d\theta}{d\xi} \right] &= 0 & \left[\frac{d\phi_{\text{ox}}}{d\xi} \right] &= 0, \end{aligned} \quad (\text{C.8})$$

where $[\cdot]$ denotes a jump across the interface, and far-field values,

$$\begin{aligned} \theta(+\infty, y) &= 0 & \theta(-\infty, y) &= 0 \\ \phi_{\text{ox}}(+\infty, y) &= 1 & \phi_{\text{ox}}(-\infty, y) &= 0 \end{aligned} \quad (\text{C.9})$$

After some straightforward algebra, we arrive at the solutions on either side of the interfaces. For the dimensionless temperature we have,

$$\theta^{\text{ss}}(\xi) = \begin{cases} \theta_{\text{ign}} \exp \left[\frac{u}{2} \left(-1 + \sqrt{(1 + 4\Gamma/u^2)} \right) \xi \right] + \frac{A}{u^2 (1 + \zeta_1) (\zeta_2^2 + \zeta_2 - \Gamma/u^2)} \\ \times \left\{ \exp \left[\frac{u}{2} \left(-1 + \sqrt{(1 + 4\Gamma/u^2)} \right) \xi \right] - \exp [u \text{Le} \zeta_1 \xi] \right\} & \xi \leq 0 \\ \theta_{\text{ign}} \exp \left[-\frac{u}{2} \left(1 + \sqrt{(1 + 4\Gamma/u^2)} \right) \xi \right] & \xi > 0, \end{cases} \quad (\text{C.10})$$

while the solution for the concentration becomes

$$\phi_{\text{ox}}^{\text{ss}}(\xi) \begin{cases} \frac{1}{1 + \zeta_1} \exp[u \text{Le} \zeta_1 \xi] & \xi \leq 0 \\ \frac{-\zeta_1}{1 + \zeta_1} \exp[-u \text{Le} \xi] + 1.0 & \xi > 0, \end{cases} \quad (\text{C.11})$$

where

$$\zeta_1 = \frac{1}{2} \left(-1 + \sqrt{1 + \frac{4A}{\text{Le} u^2}} \right) \quad (\text{C.12})$$

$$\zeta_2 = \text{Le} \zeta_1$$

Applying the continuity condition (Eq. (C.8)) for temperature field across the interface, i.e., $\theta(0^+) = \theta(0^-) = \theta_{\text{ig}}$, allows us to solve for velocity. This gives

$$u = \left(\frac{-1 + \theta_{\text{ign}} \nu}{-1/2 \theta_{\text{ign}} \nu^2 + (\text{Le} - 1/2) \theta_i \nu - \text{Le}} \right) \times \sqrt{-2A \text{Le} (\theta_{\text{ign}} \nu (1 + \nu))^3 \left(-1/2 \theta_{\text{ign}} \nu^2 + (\text{Le} - 1/2) \theta_{\text{ign}} \nu - \text{Le} \right)}, \quad (\text{C.13})$$

where $\nu = \sqrt{1 + 4\Gamma}$. To further simplify the perturbation analysis we normalize the velocity of a planar front $u = 1$. This can be done by choosing the normalization factor A in the following form,

$$A = \frac{\nu(\nu + 1)\theta_{\text{ign}}}{2(1 - \theta_{\text{ign}} \nu)} \left(1 + \frac{\theta_{\text{ign}} \nu (1 + \nu)}{2 \text{Le} (1 - \theta_i \nu)} \right). \quad (\text{C.14})$$

For $\Gamma = 0$, Eq. (C.14) reduces to the one calculated by brailovsky et al. [22]. By inserting Eq. (C.14) into Eqs. (C.10-C.11) and recalling that $u = 1$, the final forms of steady-state solutions are given by,

$$\theta^{\text{ss}}(\xi) = \begin{cases} \theta_{\text{ign}} \exp\left[\frac{(-1+\nu)\xi}{2}\right] + \left(\frac{2\theta_{\text{ign}}\nu(1-\theta_{\text{ign}}\nu)}{2\theta_{\text{ign}}\nu^2 - \nu + 1}\right) \times \\ \left\{ \exp\left[\frac{(-1+\nu)\xi}{2}\right] - \exp\left[\text{Le} \frac{\theta_{\text{ign}}\nu(1+\nu)}{2\text{Le}(1-\theta_{\text{ign}}\nu)} \xi\right] \right\} & \xi \leq 0 \\ \theta_{\text{ign}} \exp\left(-\frac{(1+\nu)\xi}{2}\right), & \xi > 0 \end{cases} \quad (\text{C.15})$$

$$\phi_{\text{ox}}^{\text{ss}}(\xi) = \begin{cases} \frac{1}{1 + \frac{\theta_{\text{ign}}\nu(1+\nu)}{2\text{Le}(1-\theta_{\text{ign}}\nu)}} \exp\left[\frac{\theta_{\text{ign}}\nu(1+\nu)}{2(1-\theta_{\text{ign}}\nu)} \xi\right] & \xi \leq 0 \\ \frac{-1}{1 + \frac{2\text{Le}(1-\theta_{\text{ign}}\nu)}{\theta_{\text{ign}}\nu(1+\nu)}} \exp(-\text{Le}\xi) + 1.0 & \xi > 0 \end{cases} \quad (\text{C.16})$$

We now proceed with the perturbation the of the steady state solutions of fields and of the 2D interface $x = F(y, t)$ with following forms,

$$\theta(\xi, y, t) = \theta^{\text{ss}}(\xi) + \theta'(\xi, y, t)$$

$$\phi_{\text{ox}}(\xi, y, t) = \phi_{\text{ox}}^{\text{ss}}(\xi) + \phi'(\xi, y, t) \quad (\text{C.17})$$

$$F(y, t) = (1)t + f'(y, t)$$

where the 1 is a placeholder for u , which we set to $u = 1$ for simplicity, and where

$$\begin{aligned}\theta'(\xi, y, t) &= \hat{\theta}(\xi) \exp(\omega t + iky) \\ \phi'(\xi, y, t) &= \hat{\phi}(\xi) \exp(\omega t + iky) \\ f'(y, t) &= \hat{f} \exp(\omega t + iky)\end{aligned}\tag{C.18}$$

Conditions for perturbations and their derivatives across the interface, corresponding to Eq. (C.8), are given by,

$$\left\{ \begin{array}{l} \theta'(\xi = 0^+) = \theta'(\xi = 0^-) = \frac{f' \theta_i(1 + \nu)}{2} \\ \\ \phi'(\xi = 0^+) = \phi'(\xi = 0^-) = \frac{-f' \text{Le}(\theta_{\text{ign}} \nu (1 + \nu))}{\theta_{\text{ign}} \nu (1 + \nu) + 2 \text{Le}(1 - \theta_{\text{ign}})} \\ \\ \frac{\partial \theta'(0^+)}{\partial \xi} - \frac{\partial \theta'(0^-)}{\partial \xi} = \frac{f' \theta_{\text{ign}} (1 + \nu) \nu}{2(\theta_{\text{ign}} \nu - 1)} \\ \\ \frac{\partial \phi'(0^+)}{\partial \xi} - \frac{\partial \phi'(0^-)}{\partial \xi} = f' G(\nu, \text{Le}), \end{array} \right. \tag{C.19}$$

These equations are derived by expanding the perturbed fields (θ and ϕ) and their derivatives around the interface position (prior to perturbation $\xi = 0$) and only keep terms to linear order. This for instance for the temperature reads,

$$\theta(0 - f', y, t) = \theta^{\text{ss}}(\xi = 0) - f' \frac{\partial \theta^{\text{ss}}}{\partial \xi} \Big|_{\xi=0} + \dots, \tag{C.20}$$

By comparing Eq. (C.20) with definition of perturbation in Eqs. (C.17), one can show

$$\theta'(0, y, t) = -f' \frac{\partial \theta_{ss}}{\partial \xi} \Big|_{\xi=0} + \dots, \quad (\text{C.21})$$

By inserting the derivative of steady-state temperature (Eqs. (C.15)) evaluated on both sides of the interface, in Eq. (C.21) the continuity condition for temperature perturbation across the interface gives $\theta'(\xi = 0^+) = \theta'(\xi = 0^-) = \frac{f' \theta_i(1+\nu)}{2}$. The conditions for other field and derivatives across the interface can be derived using the similar approach.

We now continue our analysis by inserting Eqs. (C.17) into Eqs. (C.4), recalling that u is unity, and cancelling terms that correspond to the steady state solutions, which gives

$$\begin{cases} \frac{\partial \theta'}{\partial t} - \frac{\partial \theta'}{\partial \xi} = \frac{\partial^2 \theta'}{\partial \xi^2} + \frac{\partial^2 \theta'}{\partial y^2} - \Gamma \theta' + W' \\ \frac{\partial \phi'}{\partial t} - \frac{\partial \phi'}{\partial \xi} = \frac{1}{Le} \left(\frac{\partial^2 \phi'}{\partial \xi^2} + \frac{\partial^2 \phi'}{\partial y^2} \right) - W', \end{cases} \quad (\text{C.22})$$

where $W'(\xi \leq 0) = A\phi'$ and $W'(\xi) = 0$, for $\xi > 0$. Substituting Eqs. (C.18) into Eqs. (C.22), and solving for the perturbations gives

$$\theta'(\xi) = \begin{cases} n \exp(p_+ \xi) + \frac{mA}{(\omega + k^2 + \Gamma) - l_+^2 - l_+} \exp(l_+ \xi) & \xi \leq 0 \\ a \exp(p_- \xi) & \xi > 0, \end{cases} \quad (\text{C.23})$$

for the temperature perturbation, and for perturbation in concentration,

$$\phi'(\xi) = \begin{cases} m \exp(l_+ \xi) & \xi \leq 0 \\ b \exp(q_- \xi) & \xi > 0, \end{cases} \quad (\text{C.24})$$

where a, b, m, n are arbitrary constants. Substituting Eqs. (C.23 - C.24) into Eq. (C.19) leads to the following algebraic equations for free parameters,

$$\begin{cases} a - \frac{f' \theta_{\text{ign}}}{2} (1 + \nu) = 0 \\ n + \frac{A m}{(\omega + k^2 + \Gamma) - l_+^2 - l_+} - \frac{f' \theta_{\text{ign}} (1 + \nu)}{2} = 0 \\ a p_- - \left(n p_+ + \frac{A m l_+}{(\omega + k^2 + \Gamma) - l_+^2 - l_+} \right) - \frac{f' \theta_{\text{ign}} (1 + \nu) \nu}{2(\theta_{\text{ign}} \nu - 1)} = 0 \\ m = b \\ (b q_- - m l_+) - f' G(\nu, \text{Le}) = 0 \end{cases} \quad (\text{C.25})$$

where subsequent parameters have been defined,

$$\begin{aligned} G(\nu, \text{Le}) &= \frac{\text{Le}^2}{1 + \frac{2 \text{Le} (1 - \theta_{\text{ign}})}{\theta_{\text{ign}} \nu (1 + \nu)}} + \frac{\theta_{\text{ign}}^2 (\nu (1 + \nu))^2}{(-2 \theta_{\text{ign}} \nu + 2)^2 \left(1 + \frac{\theta_{\text{ign}} \nu (1 + \nu)}{\text{Le} (1 - \theta_{\text{ign}} \nu)}\right)} \\ q_{\pm} &= \frac{1}{2} \left[-\text{Le} \pm \sqrt{\text{Le}^2 + 4(k^2 + \text{Le} \omega)} \right] \\ l_{\pm} &= \frac{1}{2} \left[-\text{Le} \pm \sqrt{\text{Le}^2 + 4(k^2 + \text{Le} \omega + A \text{Le})} \right] \\ p_{\pm} &= \frac{1}{2} \left[-1 \pm \sqrt{1 + 4(\omega + k^2 + \Gamma)} \right] \end{aligned} \quad (\text{C.26})$$

Now the perturbation problem reduces to the problem of system of coupled linear homogeneous equations which can be solved by rewriting Eqs. (C.25) in the following matrix form,

$$\begin{bmatrix} 1 & 0 & 0 & 0 & -\frac{\theta_{ig}(1+\nu)}{2} \\ 0 & 0 & \frac{A}{(\omega + k^2 + \Gamma) - l_+^2 - l_+} & 1 & -\frac{\theta_{ig}(1+\nu)}{2} \\ p_- & 0 & \frac{-Al_+}{(\omega + k^2 + \Gamma) - l_+^2 - l_+} & -p_+ & -\frac{\theta_{ig}(1+\nu)\nu}{2(\theta_{ig}\nu - 1)} \\ 0 & -1 & 1 & 0 & 0 \\ 0 & q_- & -l_+ & 0 & -G(\nu, Le) \end{bmatrix} \begin{bmatrix} a \\ b \\ m \\ n \\ f' \end{bmatrix} = \vec{0} \quad (C.27)$$

In order to ensure a non-trivial solution, the determinant of coefficient in Eq. (C.27) is set to zero, and following dispersion relation is derived :

$$\Delta(\omega, k, Le, \Gamma) = -G(\nu, Le) A(p - l) \quad (C.28)$$

$$+ (q - l) \left[\frac{\theta_{ig}(1+\nu)}{2} \left(\frac{\nu}{\nu \theta_{ig} - 1} + (1 - 2p) \right) \dots \right. \\ \left. \dots \times \left((1 - Le)(\omega - l) - ALe + \Gamma \right) \right] = 0.$$

This equation is used in the text to analyze the growth rate of combustion fronts evolving with the Master Model equations with dissipation. To our knowledge, this analysis has not been performed elsewhere in the literature.

References

- [1] A. Aldushin, M. AG, and B. Khaikin. Some features of combustion of condensed systems with refractory reaction products. *Doklady Akademii Nauk SSSR*, 204(5):1139, 1972.
- [2] A. Aldushin and B. Matkowsky. Instabilities, fingering and the saffman-taylor problem in filtration combustion. *Combustion science and technology*, 133(4-6):293–341, 1998.
- [3] A. Aldushin, A. Merzhanov, and B. Seplyarskii. Theory of filtration combustion of metals. *Combustion, Explosion, and Shock Waves*, 12(3):285–294, 1976.
- [4] C. Altantzis, C. Frouzakis, A. Tomboulides, M. Matalon, and K. Boulouchos. Hydrodynamic and thermodiffusive instability effects on the evolution of laminar planar lean premixed hydrogen flames. *Journal of Fluid Mechanics*, 700:329–361, 2012.
- [5] M. Amoorezaei, S. Gurevich, and N. Provatas. Spacing characterization in al–cu alloys directionally solidified under transient growth conditions. *Acta Materialia*, 58(18):6115–6124, 2010.
- [6] M. Amoorezaei, S. Gurevich, and N. Provatas. Orientation selection in solidification patterning. *Acta Materialia*, 60(2):657–663, 2012.
- [7] K. K. Andreev and A. F. Belyaev. Theory of explosive substances. Technical report, DTIC Document, 1966.
- [8] V. Antonov, T. Ivanina, I. Berezin, and K. Martinek. n-alkylboronic acids as bifunctional reversible inhibitors of α -chymotrypsin. *FEBS letters*, 7(1):23–25, 1970.
- [9] R. Arnold, K. Showalter, and J. Tyson. Luther’s 1906 discovery and analysis of chemical waves. *J. Chem. Ed.(submitted)*, 1987.

- [10] B. P. Athreya, N. Goldenfeld, J. A. Dantzig, M. Greenwood, and N. Provatas. Adaptive mesh computation of polycrystalline pattern formation using a renormalization-group reduction of the phase-field crystal model. *Physical Review E*, 76(5):056706, 2007.
- [11] M. Bär. *Complex patterns in reaction-diffusion-systems*. PhD thesis, Habilitationsschrift, Technische Universität Dresden, 2001.
- [12] M. Bär, N. Gottschalk, M. Eiswirth, and G. Ertl. Spiral waves in a surface reaction: model calculations. *The Journal of chemical physics*, 100(2):1202–1214, 1994.
- [13] G. Barenblatt, Y. B. Zeldovich, and A. G. Istratov. On diffusional-thermal stability of a laminar flame. *Zh. Prikl. Mekh. Tekh. Fiz.*, 4:21–26, 1962.
- [14] J. Beck and V. Volpert. Nonlinear dynamics in a simple model of solid flame microstructure. *Physica D: Nonlinear Phenomena*, 182(1):86–102, 2003.
- [15] J. Beck and V. Volpert. A simple model of two-dimensional solid flame microstructure. *Combustion Theory and Modelling*, 7(4):795–812, 2003.
- [16] M. Beckstead. A summary of aluminum combustion. Technical Report 27–31, DTIC Document, 2003.
- [17] B. Belousov. Archives, 1951 in: Oscillations and traveling waves in chemical systems, ed. rj field and m. burger, 1985.
- [18] A. Belyaev. Combustion, detonation, and work of explosion of condensed systems. *Nauk , Moscow*, 1968.
- [19] F. Benkhaldoun, T. Fernandez, B. Larrouturou, and P. Leyland. *A dynamical adaptive method based on local refinement and unrefinement for triangular finite-element meshes: Preliminary results*. PhD thesis, INRIA, 1990.
- [20] D. Bensimon and P. Pelcé. Tip-splitting solutions to a stefan problem. *Physical Review A*, 33(6):4477, 1986.
- [21] I. Borovinskaya, M. Nersesyan, and S. Dolukhanyan. Gravimetric investigation of combustion of porous metallic samples in hydrogen. *Combustion, Explosion, and Shock Waves*, 13(6):807–810, 1977.

- [22] I. Brailovsky, P. V. Gordon, L. Kagan, and G. Sivashinsky. Diffusive-thermal instabilities in premixed flames: Stepwise ignition-temperature kinetics. *Combustion and Flame*, 162(5):2077–2086, 2015.
- [23] I. Brailovsky and G. Sivashinsky. Chaotic dynamics in solid fuel combustion. *Physica D: Nonlinear Phenomena*, 65(1):191–198, 1993.
- [24] B. Bregeon, A. S. Gordon, and F. A. Williams. Near-limit downward propagation of hydrogen and methane flames in oxygennitrogen mixtures. *Combustion and Flame*, 33:33–45, 1978.
- [25] N. F. Britton et al. *Reaction-diffusion equations and their applications to biology*. Academic Press, 1986.
- [26] M. Burden and J. Hunt. Cellular and dendritic growth. i. *Journal of Crystal Growth*, 22(2):99–108, 1974.
- [27] M. Burden and J. Hunt. Cellular and dendritic growth. ii. *Journal of Crystal Growth*, 22(2):109–116, 1974.
- [28] S. Burke and T. Schumann. Diffusion flames. *Industrial & Engineering Chemistry*, 20(10):998–1004, 1928.
- [29] V. Castets, E. Dulos, J. Boissonade, and P. De Kepper. Experimental evidence of a sustained standing turing-type nonequilibrium chemical pattern. *Physical Review Letters*, 64(24):2953, 1990.
- [30] T. Choy, A. Alexopoulos, and M. Thorpe. Dielectric function for a material containing hyperspherical inclusions to o (c2): I. multipole expansions. In *Proceedings of the Royal Society of London A: Mathematical, Physical and Engineering Sciences*, volume 454, pages 1973–1992. The Royal Society, 1998.
- [31] P. Clavin. Dynamic behavior of premixed flame fronts in laminar and turbulent flows. *Progress in Energy and Combustion Science*, 11(1):1–59, 1985.
- [32] P. Clavin and F. Williams. Effects of molecular diffusion and of thermal expansion on the structure and dynamics of premixed flames in turbulent flows of large scale and low intensity. *Journal of fluid mechanics*, 116:251–282, 1982.
- [33] M. Conti and U. M. B. Marconi. Fingering in slow combustion. *Physica A: Statistical Mechanics and its Applications*, 312(3):381–391, 2002.

- [34] Y. Couder. Growth patterns: from stable curved fronts to fractal structures. In *Chaos, order, and patterns*, pages 203–227. Springer, 1991.
- [35] M. C. Cross and P. C. Hohenberg. Pattern formation outside of equilibrium. *Reviews of modern physics*, 65(3):851, 1993.
- [36] P. Daniell. The theory of flame motion. *Proceedings of the Royal Society of London. Series A, Containing Papers of a Mathematical and Physical Character*, 126(802):393–405, 1930.
- [37] G. Darrieus. Propagation d'un front de flamme. *La Technique Moderne*, 30:18, 1938.
- [38] P. De Kepper, V. Castets, E. Dulos, and J. Boissonade. Turing-type chemical patterns in the chlorite-iodide-malonic acid reaction. *Physica D: Nonlinear Phenomena*, 49(1-2):161–169, 1991.
- [39] P. De Kepper, I. R. Epstein, K. Kustin, and M. Orban. Systematic design of chemical oscillators. part 8. batch oscillations and spatial wave patterns in chlorite oscillating systems. *The Journal of Physical Chemistry*, 86(2):170–171, 1982.
- [40] J. De Ris. Spread of a laminar diffusion flame. In *Symposium (international) on Combustion*, volume 12, pages 241–252. Elsevier, 1969.
- [41] A. De Wit. Spatial patterns and spatiotemporal dynamics in chemical systems. *Advances in chemical physics*, 109:435–514, 1999.
- [42] B. Denet. Turbulent scales smaller than the flame thickness. *Physical Review E*, 59(3):2966, 1999.
- [43] B. Denet and P. Haldenwang. A local extinction of the thermo-diffusive premixed flame at low lewis number. In *Numerical Combustion*, pages 223–232. Springer, 1989.
- [44] B. Denet and P. Haldenwang. Numerical study of thermal-diffusive instability of premixed flames. *Combustion science and technology*, 86(1-6):199–221, 1992.
- [45] P. Dimitriou, J. Puszynski, and V. Hlavacek. On the dynamics of equations describing gasless combustion in condensed systems. *Combustion Science and Technology*, 68(4-6):101–111, 1989.

- [46] B. A. Dubrovin. Periodic problems for the korteweg—de vries equation in the class of finite band potentials. *Functional analysis and its applications*, 9(3):215–223, 1975.
- [47] L. Edelstein-Keshet. *Mathematical models in biology*. SIAM, 2005.
- [48] I. R. Epstein, I. Lengyel, S. Kádár, M. Kagan, and M. Yokoyama. New systems for pattern formation studies. *Physica A: Statistical Mechanics and its Applications*, 188(1):26–33, 1992.
- [49] M. Falcke and H. Levine. Pattern selection by gene expression in dictyostelium discoideum. *Physical review letters*, 80(17):3875, 1998.
- [50] P. C. Fife. *Mathematical aspects of reacting and diffusing systems*, volume 28. Springer Science & Business Media, 2013.
- [51] R. A. Fisher. The wave of advance of advantageous genes. *Annals of eugenics*, 7(4):355–369, 1937.
- [52] R. FitzHugh. Impulses and physiological states in theoretical models of nerve membrane. *Biophysical journal*, 1(6):445–466, 1961.
- [53] J.-M. Flesselles, A. Simon, and A. Libchaber. Dynamics of one-dimensional interfaces: an experimentalist’s view. *Advances in Physics*, 40(1):1–51, 1991.
- [54] M. Frankel, V. Roytburd, and G. Sivashinsky. A sequence of period doublings and chaotic pulsations in a free boundary problem modeling thermal instabilities. *SIAM Journal on Applied Mathematics*, 54(4):1101–1112, 1994.
- [55] M. Frankel and G. Sivashinsky. On effects due to thermal expansion and lewis number in spherical flame propagation. *Combustion science and technology*, 31(3-4):131–138, 1983.
- [56] M. Frankel and G. Sivashinsky. On the equation of a curved flame front. *Physica D: Nonlinear Phenomena*, 30(1):28–42, 1988.
- [57] N. Ghoniem and D. Walgraef. *Patterns, Defects, and Materials Instabilities*. Kluwer Academic Publishers, 1990.
- [58] A. Gierer and H. Meinhardt. A theory of biological pattern formation. *Biological Cybernetics*, 12(1):30–39, 1972.

- [59] I. Gololobov, E. Granovskii, and Y. A. Gostintsev. Two combustion modes at the limit of luminous flame propagation. *Combustion, Explosion, and Shock Waves*, 17(1):22–26, 1981.
- [60] S. Goroshin, M. Bidabadi, and J. Lee. Quenching distance of laminar flame in aluminum dust clouds. *Combustion and Flame*, 105(1):147–160, 1996.
- [61] S. Goroshin, F.-D. Tang, and A. J. Higgins. Reaction-diffusion fronts in media with spatially discrete sources. *Physical Review E*, 84(2):027301, 2011.
- [62] M. Greenwood, M. Haataja, and N. Provatas. Crossover scaling of wavelength selection in directional solidification of binary alloys. *Physical review letters*, 93(24):246101, 2004.
- [63] E. G. Groff. The cellular nature of confined spherical propane-air flames. *Combustion and Flame*, 48:51–62, 1982.
- [64] G. H. Gunaratne, Q. Ouyang, and H. L. Swinney. Pattern formation in the presence of symmetries. *Physical Review E*, 50(4):2802, 1994.
- [65] S. Gurevich, M. Amoorezaei, and N. Provatas. Phase-field study of spacing evolution during transient growth. *Phys. Rev. E*, 82:051606, 2010.
- [66] S. Gurevich, A. Karma, M. Plapp, and R. Trivedi. Phase-field study of three-dimensional steady-state growth shapes in directional solidification. *Physical Review E*, 81(1):011603, 2010.
- [67] T. Haxhimali, A. Karma, F. Gonzales, and M. Rappaz. Orientation selection in dendritic evolution. *nature materials*, 5(8):660–664, 2006.
- [68] J. Hirschfelder, C. Curtiss, and D. E. Campbell. The theory of flame propagation. iv. *The Journal of Physical Chemistry*, 57(4):403–414, 1953.
- [69] A. L. Hodgkin and A. F. Huxley. A quantitative description of membrane current and its application to conduction and excitation in nerve. *The Journal of physiology*, 117(4):500, 1952.
- [70] D. Horváth, V. Petrov, S. K. Scott, and K. Showalter. Instabilities in propagating reaction-diffusion fronts. *The Journal of chemical physics*, 98(8):6332–6343, 1993.

- [71] D. Horváth and K. Showalter. Instabilities in propagating reaction-diffusion fronts of the iodate-arsenous acid reaction. *The Journal of chemical physics*, 102(6):2471–2478, 1995.
- [72] S. Howison. Complex variable methods in hele–shaw moving boundary problems. *European Journal of Applied Mathematics*, 3(03):209–224, 1992.
- [73] Y. Huang, G. A. Risha, V. Yang, and R. A. Yetter. Combustion of bimodal nano/micron-sized aluminum particle dust in air. *Proceedings of the Combustion Institute*, 31(2):2001–2009, 2007.
- [74] S. Hwang, A. Mukasyan, A. Rogachev, and A. Varma. Combustion wave microstructure in gas-solid reaction systems: experiments and theory. *Combustion science and technology*, 123(1-6):165–184, 1997.
- [75] J. M. Hyman and B. Nicolaenko. The kuramoto-sivashinsky equation: a bridge between pde’s and dynamical systems. *Physica D: Nonlinear Phenomena*, 18(1):113–126, 1986.
- [76] A. Istratov and V. Librovich. On the stability of propagation of spherical flames. *Journal of Applied Mechanics and Technical Physics*, 7(1):43–50, 1966.
- [77] E. B. Jacob, I. Cohen, and H. Levine. Cooperative self-organization of microorganism. *Adv. Phys.*, 49:395–554, 2000.
- [78] W. Jahnke, W. Skaggs, and A. T. Winfree. Chemical vortex dynamics in the belousov-zhabotinskii reaction and in the two-variable oregonator model. *The Journal of Physical Chemistry*, 93(2):740–749, 1989.
- [79] É. Jouguet. *Mécanique des explosifs*, volume 10. Mame, 1917.
- [80] G. Joulin and G. Sivashinsky. On the dynamics of nearly-extinguished non-adiabatic cellular flames. *Combustion science and technology*, 31(1-2):75–90, 1983.
- [81] P. Julien, J. Vickery, S. Goroshin, D. L. Frost, and J. M. Bergthorson. Freely-propagating flames in aluminum dust clouds. *Combustion and Flame*, 162(11):4241–4253, 2015.
- [82] S. Kadokawa and T. Hasegawa. Numerical simulation of dynamics of premixed flames: flame instability and vortex–flame interaction. *Progress in energy and combustion science*, 31(3):193–241, 2005.

- [83] T. Kashiwagi and S. L. Olson. Radiative ignition and transition to spread investigation (ritsi). In *NASA CONFERENCE PUBLICATION*, pages 97–118. NASA, 1998.
- [84] J. Keener and J. Sneyd. Mathematical physiology, interdisciplinary applied mathematics 8, 1998.
- [85] A. R. Kerstein, W. T. Ashurst, and F. A. Williams. Field equation for interface propagation in an unsteady homogeneous flow field. *Physical Review A*, 37(7):2728, 1988.
- [86] L. Khitrin. Combustion and explosion physics. *Moscow State Univ*, 1957.
- [87] N. Kilker, D. Golovaty, P. V. Gordon, L. Kagan, and G. I. Sivashinsky. Strongly nonlinear asymptotic model of cellular instabilities in premixed flames with step-wise ignition temperature kinetics. *arXiv preprint arXiv:1612.06763*, 2016.
- [88] G. F. Knorre, I. Paleev, et al. theory of furnace processes. *Energiya, Moscow-Leningrad*, 1966.
- [89] A. N. Kolmogorov, I. G. Petrovskii, and N. S. Piskunov. A study of the equation of diffusion with increase in the quantity of matter, and its application to a biological problem. *Bjul. Moskovskogo Gos. Univ*, 1(7):1–26, 1937.
- [90] V. Krinsky. *Self-organization: autowaves and structures far from equilibrium*. Springer, 1984.
- [91] L. Landau. On the theory of slow combustion. *Acta physicochim. URSS*, 19(1):77–85, 1944.
- [92] J. Langer. Instabilities and pattern formation in crystal growth. *Reviews of Modern Physics*, 52(1):1, 1980.
- [93] K. J. Lee, E. C. Cox, and R. E. Goldstein. Competing patterns of signaling activity in dictyostelium discoideum. *Physical review letters*, 76(7):1174, 1996.
- [94] I. Lengyel and I. R. Epstein. Modeling of turing structures in the chlorite-iodide-malonic acid-starch reaction system. *Science*, 251(4994):650, 1991.
- [95] B. Lewis and G. von Elbe. On the theory of flame propagation. *The Journal of Chemical Physics*, 2(8):537–546, 1934.

- [96] B. Lewis and G. von Elbe. *Combustion, Flames and Explosives of Gases*. Academic Press, 1961.
- [97] B. Lewis and G. Von Elbe. *Combustion, flames and explosions of gases*. Elsevier, 2012.
- [98] A. Linan. The asymptotic structure of counterflow diffusion flames for large activation energies. *Acta Astronautica*, 1(7-8):1007–1039, 1974.
- [99] J. Lindsay, R. J. Field, and M. Burger. *Oscillations and traveling waves in chemical systems*. Wiley, 1985.
- [100] C. Lu and Y. C. Yortsos. Pattern formation in reverse filtration combustion. *Physical Review E*, 72(3):036201, 2005.
- [101] R. Luther. Räumliche ausbreitung chemischer reaktionen. *Zeitschrift für Elektrochemie*, 12:596–600, 1906.
- [102] P. Maini, K. Painter, and H. P. Chau. Spatial pattern formation in chemical and biological systems. *Journal of the Chemical Society, Faraday Transactions*, 93(20):3601–3610, 1997.
- [103] Y. M. Maksimov, A. Pak, G. Lavrenchuk, Y. S. Naiborodenko, and A. Merzhanov. Spin combustion of gasless systems. *Combustion, Explosion, and Shock Waves*, 15(3):415–418, 1979.
- [104] J. Malchi, R. Yetter, S. Son, and G. Risha. Nano-aluminum flame spread with fingering combustion instabilities. *Proceedings of the Combustion Institute*, 31(2):2617–2624, 2007.
- [105] E. Mallard and H. Le Chatelier. *Recherches expérimentales et théoriques sur la combustion des mélanges gazeux explosives*. H. Dunod et E. Pinat, 1883.
- [106] S. B. Margolis. Time-dependent solution of a premixed laminar flame. *Journal of Computational Physics*, 27(3):410–427, 1978.
- [107] G. Markstein. Cell structure of propane flames burning in tubes. *The Journal of Chemical Physics*, 17(4):428–429, 1949.
- [108] G. Markstein. *Non-steady flame Propagation*. McMillan Publication, New York, 1964.

- [109] G. Markstein. Nonstationary flame propagation [russian translation]. *Mir, Moscow*, 1968.
- [110] G. Markstein. Flames as amplifiers of fluid mechanical disturbances. In *Proceedings of the Sixth US National Congress for Applied Mechanics, Harvard University, Cambridge, MA*, pages 11–33, 1970.
- [111] G. H. Markstein. Experimental and theoretical studies of flame-front stability. *Journal of the Aeronautical Sciences*, 18(3):199–209, 1951.
- [112] G. H. Markstein. Experimental and theoretical studies of flame-front stability. *Journal of the Aeronautical Sciences*, 2012.
- [113] M. Maruyama. The second cybernetics: Deviation-amplifying mutual causal processes. *American scientist*, 51(2):164–179, 1963.
- [114] M. Matalon and B. Matkowsky. Flames as gasdynamic discontinuities. *Journal of Fluid Mechanics*, 124:239–259, 1982.
- [115] B. Matkowsky and G. Sivashinsky. Propagation of a pulsating reaction front in solid fuel combustion. *SIAM Journal on Applied Mathematics*, 35(3):465–478, 1978.
- [116] A. Merzhanov. Thermal explosion and ignition as a method for formal kinetic studies of exothermic reactions in the condensed phase. *Combustion and Flame*, 11(3):201–211, 1967.
- [117] A. Merzhanov. The theory of stable homogeneous combustion of condensed substances. *Combustion and Flame*, 13(2):143–156, 1969.
- [118] A. Merzhanov. Self-developing high-temperature synthesis of refractory compounds. *Akademiia Nauk SSSR, Vestnik*, 10:76–84, 1976.
- [119] A. Merzhanov. Shs processes: Combustion theory and practice. *Arch. Combustionis*, 1(23):4, 1981.
- [120] A. Merzhanov. History and recent developments in shs. *Ceramics international*, 21(5):371–379, 1995.
- [121] A. Merzhanov and B. Khaikin. Theory of combustion waves in homogeneous media. *Progress in energy and combustion science*, 14(1):1–98, 1988.
- [122] T. Mitani and F. Williams. Studies of cellular flames in hydrogen oxygen nitrogen mixtures. *Combustion and Flame*, 39(2):169–190, 1980.

- [123] J. J. Moore and H. Feng. Combustion synthesis of advanced materials: Part i. reaction parameters. *Progress in Materials Science*, 39(4):243–273, 1995.
- [124] C. Morris and H. Lecar. Voltage oscillations in the barnacle giant muscle fiber. *Biophysical journal*, 35(1):193–213, 1981.
- [125] W. W. Mullins and R. Sekerka. Stability of a planar interface during solidification of a dilute binary alloy. *Journal of applied physics*, 35(2):444–451, 1964.
- [126] W. W. Mullins and R. F. Sekerka. Morphological stability of a particle growing by diffusion or heat flow. *Journal of applied physics*, 34(2):323–329, 1963.
- [127] Z. A. Munir and U. Anselmi-Tamburini. Self-propagating exothermic reactions: the synthesis of high-temperature materials by combustion. *Materials Science Reports*, 3(6):279–365, 1989.
- [128] J. Murray. Parameter space for turing instability in reaction diffusion mechanisms: a comparison of models. *Journal of Theoretical Biology*, 98(1):143–163, 1982.
- [129] J. Murray. Mathematical biology springer-verlag berlin. *Google Scholar*, 1989.
- [130] J. Murray. Mathematical biology. vol. 1: An introduction. interdisciplinary applied mathematics 17, 2002.
- [131] J. D. Murray. *Mathematical Biology. II Spatial Models and Biomedical Applications {Interdisciplinary Applied Mathematics V. 18}*. Springer-Verlag New York Incorporated, 2001.
- [132] G. Nicolis, I. Prigogine, et al. *Self-organization in nonequilibrium systems*, volume 191977. Wiley, New York, 1977.
- [133] T. Nozakura and S. Ikeuchi. Formation of dissipative structures in galaxies. *The Astrophysical Journal*, 279:40–52, 1984.
- [134] W. Nusselt. The rate of ignition of combustible gas mixtures. *Z. Ver. Dtsch. Ing*, 59:872–878, 1915.
- [135] Q. Ouyang, Z. Noszticzius, and H. L. Swinney. Spatial bistability of two-dimensional turing patterns in a reaction-diffusion system. *The Journal of Physical Chemistry*, 96(16):6773–6776, 1992.
- [136] Q. Ouyang and H. L. Swinney. Transition from a uniform state to hexagonal and striped turing patterns. *Nature*, 352(6336):610–612, 1991.

- [137] K. M. Page, P. K. Maini, and N. A. Monk. Complex pattern formation in reaction-diffusion systems with spatially varying parameters. *Physica D: Nonlinear Phenomena*, 202(1):95–115, 2005.
- [138] H. Pearlman. Excitability in high-lewis number premixed gas combustion. *Combustion and flame*, 109(3):382–398, 1997.
- [139] H. G. Pearlman and P. D. Ronney. Near-limit behavior of high-lewis number premixed flames in tubes at normal and low gravity. *Physics of Fluids (1994-present)*, 6(12):4009–4018, 1994.
- [140] J. E. Pearson and S. Ponce-Dawson. Crisis on skid row. *Physica A: Statistical Mechanics and its Applications*, 257(1):141–148, 1998.
- [141] P. Pelce and P. Clavin. Influence of hydrodynamics and diffusion upon the stability limits of laminar premixed flames. *Journal of Fluid Mechanics*, 124:219–237, 1982.
- [142] P. Pelcé and A. Libchaber. *Dynamics of curved fronts*. Elsevier, 2012.
- [143] S. S. Penner. *Chemical rocket propulsion and combustion research*. Routledge, 1962.
- [144] V. Petrov, Q. Ouyang, and H. L. Swinney. Resonant pattern formation in a chemical system. *Nature*, 388(6643):655–657, 1997.
- [145] Y. L. Pliner. *The Reduction of Metal Oxides with Aluminium*. Metallurgia, 1967.
- [146] N. Provatas, N. Goldenfeld, and J. Dantzig. Efficient computation of dendritic microstructures using adaptive mesh refinement. *Physical Review Letters*, 80(15):3308, 1998.
- [147] J. Quinard, G. Searby, and L. Boyer. Cellular structures on premixed flames in a uniform laminar flow. In *Cellular structures in instabilities*, pages 331–341. Springer, 1984.
- [148] P. D. Ronney. Near-limit flame structures at low lewis number. *Combustion and Flame*, 82(1):1–14, 1990.
- [149] G. V. Samsonov. *A configurational model of matter*. Springer Science & Business Media, 2012.
- [150] J. Schnakenberg. Simple chemical reaction systems with limit cycle behaviour. *Journal of theoretical biology*, 81(3):389–400, 1979.

- [151] S. K. Scott and K. Showalter. Simple and complex propagating reaction-diffusion fronts. *Journal of Physical Chemistry*, 96:8702–8702, 1992.
- [152] V. Seetharaman and R. Trivedi. Eutectic growth: Selection of interlamellar spacings. *Metallurgical Transactions A*, 19(12):2955–2964, 1988.
- [153] L. A. Segel. *Modeling dynamic phenomena in molecular and cellular biology*. Cambridge University Press, 1984.
- [154] L. A. Segel and J. L. Jackson. Dissipative structure: an explanation and an ecological example. *Journal of Theoretical Biology*, 37(3):545–559, 1972.
- [155] N. Semenov. Nacatm 1026 (1942) trans, from prog. *Phys. Sci.(USSR) Vol*, 24:433, 1940.
- [156] B. Shraiman and D. Bensimon. Singularities in nonlocal interface dynamics. *Physical Review A*, 30(5):2840, 1984.
- [157] F. Siegert and C. J. Weijer. Three-dimensional scroll waves organize dictyostelium slugs. *Proceedings of the National Academy of Sciences*, 89(14):6433–6437, 1992.
- [158] G. Sivashinsky. On a distorted flame front as a hydrodynamic discontinuity. *Acta Astronautica*, 3(11):889–918, 1976.
- [159] G. Sivashinsky. Diffusional-thermal theory of cellular flames. *Combustion Science and Technology*, 15(3-4):137–145, 1977.
- [160] G. Sivashinsky. On self-turbulization of a laminar flame. *Acta Astronautica*, 6(5-6):569–591, 1979.
- [161] G. Sivashinsky. On spinning propagation of combustion waves. *SIAM Journal on Applied Mathematics*, 40(3):432–438, 1981.
- [162] G. Sivashinsky. On the intrinsic dynamics of premixed flames. *Philosophical Transactions of the Royal Society of London A: Mathematical, Physical and Engineering Sciences*, 332(1624):135–148, 1990.
- [163] G. I. Sivashinsky. Instabilities, pattern formation, and turbulence in flames. *Annual Review of Fluid Mechanics*, 15(1):179–199, 1983.
- [164] F. A. Smith and S. F. Pickering. Bunsen flames of unusual structure1. *Industrial & Engineering Chemistry*, 20(10):1012–1013, 1928.

- [165] A. Sokolik. Samovosplamenenie, plamya i detonatsiya v gazakh. *Self-Ignition Combustion, Flame and Detonation in Gases*(Moscow: Izd. Akad. Nauk SSSR, 1960), 1960.
- [166] M. Soo, S. Goroshin, J. M. Bergthorson, and D. L. Frost. Reaction of a particle suspension in a rapidly-heated oxidizing gas. *Propellants, Explosives, Pyrotechnics*, 40(4):604–612, 2015.
- [167] M. J. Soo, K. Kumashiro, S. Goroshin, D. L. Frost, and J. M. Bergthorson. Thermal structure and burning velocity of flames in non-volatile fuel suspensions. *Proceedings of the Combustion Institute*, 2016.
- [168] D. Spalding. Theory of particle combustion at high pressures. *ARS journal*, 29(11):828–835, 1959.
- [169] D. B. Spalding. The theory of flame phenomena with a chain reaction. *Philosophical Transactions of the Royal Society of London A: Mathematical, Physical and Engineering Sciences*, 249(957):1–25, 1956.
- [170] P. Tabeling, B. Perrin, and S. Fauve. Instability of a linear array of forced vortices. *EPL (Europhysics Letters)*, 3(4):459, 1987.
- [171] F.-D. Tang, S. Goroshin, A. Higgins, and J. Lee. Flame propagation and quenching in iron dust clouds. *Proceedings of the Combustion Institute*, 32(2):1905–1912, 2009.
- [172] F.-D. Tang, A. J. Higgins, and S. Goroshin. Effect of discreteness on heterogeneous flames: propagation limits in regular and random particle arrays. *Combustion Theory and Modelling*, 13(2):319–341, 2009.
- [173] A. M. Tartakovsky, D. M. Tartakovsky, T. D. Scheibe, and P. Meakin. Hybrid simulations of reaction-diffusion systems in porous media. *SIAM Journal on Scientific Computing*, 30(6):2799–2816, 2008.
- [174] D. Thomas. Artificial enzyme membranes, transport, memory, and oscillatory phenomena. *Analysis and control of immobilized enzyme systems*, pages 115–150, 1975.
- [175] S. Torquato. *Random heterogeneous materials: microstructure and macroscopic properties*, volume 16. Springer Science & Business Media, 2013.

- [176] R. Trivedi, S. Liu, and S. Williams. Interface pattern formation in nonlinear dissipative systems. *Nature materials*, 1(3):157–159, 2002.
- [177] A. M. Turing. The chemical basis of morphogenesis. *Philosophical Transactions of the Royal Society of London B: Biological Sciences*, 237(641):37–72, 1952.
- [178] G. Veser and R. Imbihl. Synchronization and spatiotemporal self-organization in the no+ co reaction on pt (100). i. unsynchronized oscillations on the 1× 1 substrate. *The Journal of chemical physics*, 100(11):8483–8491, 1994.
- [179] V. Voronkov and N. Semenov. Propagation of cold flames in combustible mixtures containing 0. 03% carbon disulfide. *Zh. Fiz. Khimii*, 13(12):1695–1727, 1939.
- [180] L. A. Vulis. *Thermal regimes of combustion*. McGraw-Hill, 1961.
- [181] D. Walgraef, G. Dewel, and P. Borckmans. Nonequilibrium phase transitions and chemical instabilities. *Adv. Chem. Phys.*, 49(3), 1982.
- [182] B. J. Welsh, J. Gomatam, and A. E. Burgess. Three-dimensional chemical waves in the belousov–zhabotinskii reaction. *Nature*, 304(5927):611–614, 1983.
- [183] D. B. White. The planforms and onset of convection with a temperature-dependent viscosity. *Journal of Fluid Mechanics*, 191:247–286, 1988.
- [184] N. Wiener and A. Rosenblueth. The mathematical formulation of the problem of conduction of impulses in a network of connected excitable elements, specifically in cardiac muscle. *Archivos del instituto de Cardiología de México*, 16(3):205–265, 1946.
- [185] A. T. Winfree. Spiral waves of chemical activity. *Science*, 175(4022):634–636, 1972.
- [186] A. T. Winfree. Scroll-shaped waves of chemical activity in three dimensions. *Science*, 181(4103):937–939, 1973.
- [187] A. T. Winfree. Rotating solutions to reaction-diffusion equations in simply-connected media. In *SIAM-AMS Proc*, volume 8, pages 13–31, 1974.
- [188] T. A. Witten and L. M. Sander. Diffusion-limited aggregation. *Physical Review B*, 27(9):5686, 1983.
- [189] B. Ya. Zel'dovich, da frank-kamenetskii. *Zh. Fiz. Khim*, 12:100, 1938.

- [190] A. Zaikin and A. Zhabotinsky. Concentration wave propagation in two-dimensional liquid-phase self-oscillating system. *Nature*, 225(5232):535–537, 1970.
- [191] Y. Zeldovich. Flame propagation in a substance reacting at initial temperature. *Combustion and Flame*, 39(3):219–224, 1980.
- [192] Y. B. Zeldovich. Theory of combustion and detonation of gases academy of sciences (ussr). *Institute of Chemical Physics*, 1944.
- [193] Y. Zhang, P. Ronney, E. Roegner, and J. Greenberg. Lewis number effects on flame spreading over thin solid fuels. *Combustion and flame*, 90(1):71–83, 1992.
- [194] L. Q. Zhou and Q. Ouyang. Spiral instabilities in a reaction- diffusion system. *The Journal of Physical Chemistry A*, 105(1):112–118, 2001.
- [195] O. Zik and E. Moses. Fingering instability in combustion: an extended view. *Physical Review E*, 60(1):518, 1999.
- [196] O. Zik, Z. Olami, and E. Moses. Fingering instability in combustion. *Physical review letters*, 81(18):3868, 1998.